NEW FORMULATION FOR FINITE ELEMENT MODELING ELECTROSTATICALLY DRIVEN MICROELECTROMECHANICAL SYSTEMS

by

Ilya V. Avdeev

BS, St. Petersburg State Technical University, 1997

MS, St. Petersburg State Technical University, 1999

Submitted to the Graduate Faculty of

the School of Engineering in partial fulfillment

of the requirements for the degree of

Doctor of Philosophy

University of Pittsburgh

2003

UNIVERSITY OF PITTSBURGH

SCHOOL OF ENGINEERING

This dissertation was presented

by

Ilya V. Avdeev

It was defended on

November 20, 2003

and approved by

M. Lovell, Associate Professor, Dept. of Mechanical Engineering

M. Mickle, Professor, Dept. of Electrical Engineering

O. Onipede Jr., Assistant Professor, Penn State University, Erie

D. Ostergaard, Director of Multiphysics Solutions Group, ANSYS, Inc.

J. Vipperman, Assistant Professor, Dept. of Mechanical Engineering

Q.-M. Wang, Assistant Professor, Dept. of Mechanical Engineering

Dissertation Directors: M. Lovell, Associate Professor, Dept. of Mechanical Engineering,

O. Onipede Jr., Assistant Professor, Penn State University, Erie

NEW FORMULATION FOR FINITE ELEMENT MODELING ELECTROSTATICALLY DRIVEN MICROELECTROMECHANICAL SYSTEMS

Ilya V. Avdeev, PhD

University of Pittsburgh, 2003

The increased complexity and precision requirements of microelectromechanical systems (MEMS) have brought about the need to develop more reliable and accurate MEMS simulation tools. To better capture the physical behavior encountered, several finite element analysis techniques for modeling electrostatic and structural coupling in MEMS devices have been developed in this project. Using the principle of virtual work and an approximation for capacitance, a new 2-D lumped transducer element for the static analysis of MEMS has been developed. This new transducer element is compatible to 2-D structural and beam elements. A novel strongly coupled 3-D transducer formulation has also been developed to model MEMS devices with dominant fringing electrostatic fields. The transducer is compatible with both structural and electrostatic solid elements, which allows for modeling complex devices. Through innovative internal morphing capabilities and exact element integration the 3-D transducer element is one of the most powerful coupled field FE analysis tools available. To verify the accuracy and effectiveness of both the 2-D and 3-D transducer elements a series of benchmark analyses were conducted. More specifically, the numerically predicted results for the misalignment of lateral combdrive fingers were compared to available analytical and modeling techniques. Electrostatic uncoupled 2-D and 3-D finite element models were also used to perform energy computations during misalignment. Finally, a stability analysis of misaligned combdrive was performed using a coupled 2-D finite element approach. The analytical and numerical results were compared and found to vary due to fringing fields.

TABLE OF CONTENTS

LIST OF TABLES

LIST OF FIGURES

ACKNOWLEDGEMENTS

The acknowledgements is a difficult thing to write considering the number of people that are responsible for this paper. However, a few contributions deserve to be recognized for all of their effort. First of all, I have to thank my advisors, Dipo Onipede Jr. and Michael Lovell. Without their expertise and knowledge this work could not have been started. Without their guidance and help, this work could not have been complete. My deepest gratitude goes to graduate committee members: Marlin Mickle, Dale Ostergaard, Jeffrey Vipperman and Qing-Ming Wang.

I would like to thank John Swanson for offering an incredible gift of Swanson Doctoral Fellowship to the Department of Mechanical Engineering. It was great having the freedom to choose research topic and to be able to conduct the research on our terms.

My great appreciation also goes to wonderful people of ANSYS, Inc., who actively participated in my life and research. Specifically, I'd like to thank Miklos Gyimesi, who was a constant inspiration for my research and an infinite source of wisdom and knowledge.

I would like to thank all my friends and colleagues for their support throughout the years. My deepest and most sincere appreciation goes to my parents and my wife, who had always supported me and kept me focused.

1.0   INTRODUCTION

1.1   MICROELECTROMECHANICAL SYSTEMS

The fundamental theme of this dissertation is related to the modeling of microelectrome-chanical systems (MEMS). It is therefore instructive to give a brief historical background and definition of MEMS. MEMS started in 1959 with the talk that Richard Feynman gave at the annual meeting of the American Physical Society at the California Institute of Technology [1]. "There's plenty of room at the bottom" was the name of that milestone presentation. Feynman was the first researcher who saw the future of miniaturization and issues related to practical realization of his ideas. His first "challenge" was: "I hereby offer a prize of $1,000 to the first guy who can take the information on the page of a book and put it on an area 1/25 000 smaller in linear scale in such manner that it can be read by an electron microscope." The challenge was offered as a high-school competition, because at that time nobody had started that field [1]. The work, by T. Newman and R.F.W. Pease of Stanford University, won the Feynman challenge in 1985. It took almost 26 years for technology to develop enough to overcome the fabrication issues, that Feynman described in his talk: lithography resolution, deposition, and characterization.

The second of Feynman's "challenge" was: "I want to offer another price –...– of another $1000 to the first guy who makes an operating electric motor – a rotating electric motor which can be controlled from the outside and, not counting the lead-in wires, is only 1/64 inch cube." The motor, created by McLellan, was shown in 1983 during the second milestone Feynman's talk at the Jet Propulsion Laboratory (JPL) [2]. Feynman delivered the speech that actually started the MEMS field. He was among the first – if not the first – person who proposed the use of semiconductor integrated technology to fabricate infinitesimal machines.

The technology which is known as microelectromechanical systems (MEMS) in the U.S.A., is called microsystems technology (MST) in Europe. According to Albert Pisano, a former MEMS program manager of DARPA, "...the acronym for Microelectromechanical Systems, MEMS, was adopted by a group of about 80 zealots at a crowded meeting in Salt Lake City in 1989 called the Micro-Tele-Operated Robotics Workshop..." [3]. He was a part of that group and recalls, that at the beginning, they "...constantly worried if any scholarly journal would publish the papers we wrote. Sources of research funding were hard to find and difficult to maintain. MEMS fabrication was itself a major issue, and the frequent topic of conversation was about the nature, properties, and standardization of the polysilicon that the pioneering researchers were using to demonstrate the early, elementary structures of the day." Since that time, MEMS has developed into a huge industry, research field and a market around the world. By 1997, when there were 80 U.S. companies in the MEMS field, the combined total world market of MEMS was approximately \$2 billion [3]. The most conservative studies predict a world MEMS market in excess of \$8 billion in 2003. The analysis and forecast of U.S. MEMS markets are presented in Table 1 [3]. The reality has by far exceeded the expectations of scientists and engineers. In fact, MEMS industry is not just a corner stone of innovation in technology, but it also is a lunching pad for emerging technologies, the most promising of which is nanotechnology.

The field of MEMS is relatively new, therefore there is no unique, widely accepted definition of MEMS. One of the broadest and probably the best definition was given by Maluf in 2000 [3]. He defines MEMS as simultaneously "... a toolbox, a physical product, and a methodology all in one:

- It is a portfolio of techniques and processes to design and create miniature systems;
- It is a physical product often specialized and unique to a final application – one can seldom buy a generic MEMS product at the neighborhood electronic store;
- "MEMS is a way of making things," reports DARPA. These "things" merge the functions of sensing and actuation with computation and communication to locally control physical parameters at the microscale, yet cause effects at much grander scales..."

Table 1: Analysis and forecast of U.S. MEMS markets (in millions of U.S. dollars)

Year	Automotive	Medical	IT/Industrial	Military/Aerospace	Total
1994	255.7	129.5	438.3	49.1	872.5
1995	298.0	146.1	459.0	54.8	957.9
1996	355.0	164.4	492.8	62.2	1,074.3
1997	419.0	187.0	527.0	71.6	1,204.6
1998	491.5	216.7	575.3	79.6	1,363.1
1999	552.0	245.7	645.9	95.8	1,549.4
2000	645.7	291.3	733.3	110.7	1,781.0
2001	758.5	354.8	836.0	133.3	2,082.5
2002	879.6	444.7	995.1	156.9	2,476.3
2003	1,019	562.9	1,222	176.7	2,980.4
2004	1,172	716.0	1,514	202.7	3,604.5

The present and future applications of MEMS can be combined into several groups (Table 2) [3]. There is a number of comprehensive reviews of MEMS applications, focusing on the sensor and actuator systems by Ko [4], actuators by Fujita [5], polysilicon integrated microsystems by Howe [6], IC microtransducers by Baltes [7], and general reviews by Bao [8] and Fluitman [9]. The impact of MEMS technology on society is the subject of Bryzek's review [10]. The design future and present trends are covered in reviews of Senturia [11] and Wachutka [12], [13].

1.2 ELECTROSTATICALLY DRIVEN MEMS TRANSDUCERS

Electrostatically driven MEMS transducers are the subject of this research project. This is a practical choice, due to the domination of electrostatics over the other types of physical domain, such as magnetics, thermodynamics, piezoelectricity or optics [3]. There are several reasons why the coupling between electrostatics and mechanics is the "driving force" of MEMS development:

- MEMS started borrowing technology from the semiconductor industry, where silicon is the number one material [3]. The beauty of silicon, as a semiconductor material, is that it can be used either as an insulator (intrinsic silicon) or as a conductor (doped silicon). This property of the silicon, accompanied by its sufficient structural strength, allows MEMS designers to use silicon in carrying out a variety of actuation and sensing functions.

- Electrostatically driven actuators have short response time. Application and release of forces take virtually the same time, in contrary to the thermo-actuation (fast in heating and slow in cooling).

- Transducers are relatively easy to design, due to the well explored field of electrostatics. There is a variety of simplified capacitor models, which can be applied to the design of MEMS. Classical examples are parallel plate and comb capacitor models [14].

- Electrostatically driven transducers are less sensitive to environmental conditions than others. Packaging and operating conditions are not as strict as for other transducers.

The great number of applications (Table 2) requires a variety of methods and tools for designing and analyzing MEMS devices. For the last decade, MEMS technology was developing faster than simulation and analysis techniques. As a result, there is a lack of sophisticated analysis tools to model physical behavior and response of the electrostatically driven transducers.

1.3 OBJECTIVES OF RESEARCH

The purpose of this research is to extend existing and develop new numerical techniques for solving electromechanical problems in MEMS. The research will be focused on the following six major topics:

- development of a 2-D lumped transducer finite element with a strong coupling between rigid or deformable mechanical domains and slightly curved electrostatic fields, such as developed in optical mirrors, switches, resonators, etc;
- development of a novel 3-D coupled field finite element for modeling MEMS with dominating fringing electrostatic fields, such as combdrives, micromotors, etc.;
- testing of developed finite elements, comparing results of static electromechanical analyses with experimental results available in literature and with other numerical techniques;
- development of a simplified analytical model of lateral combdrive structures to model in-plane misalignments;
- development of an uncoupled FE technique for modeling in-plane combdrive misalignments to account for fringing electrostatic fields;
- pull-in combdrive analysis using analytical and strongly coupled distributed models.

The new 2-D lumped transducer element will be a generalization of 1-D transducers. The element will have a trapezoidal shape with four nodes and three degrees of freedoms per each node. The most important condition to be satisfied is its compatibility with standard plane structural elements. Electrostatic forces will be calculated within the element using the principle of virtual work. The Newton - Raphson algorithm will be the basis for the

nonlinear coupled field formulation. The element will be tested by comparing results of static analysis with results obtained using other simulation techniques (sequential coupling, 1-D lumped model and distributed transducer models) and experimental data.

The new 3-D distributed tetrahedral transducer element will also be derived using the principle of virtual work. The new element can be utilized for modeling 3-D coupled field problems with dominating fringing fields, such as static analysis of combdrives, deflectable 3-D micromirrors, and micromotors. The 3-D element will provide mesh morphing during a nonlinear analysis, making the element sufficiently faster than the sequential coupled FE models, which uses external morphers or meshers.

In order test the new 3-D element, a simplified analytical model of a misaligned combdrive can be constructed using a rigid model of fingers and certain assumptions regarding the electrostatic field. The model can be used to investigate the influence of misalignment on the combdrive driving force. A great deal of research has been focused on calculating unbalanced forces and moments and finding conditions required for stability of static equilibrium states. This is important from the designer perspective, because it sets the limits on applied voltage and structural stiffness of the transducer. The simplified analytical model doesn't account for fringing field effects. The validity of the analytical model and inaccuracies brought by simplifying assumptions need to be investigated. An uncoupled FE model has to be generated. The electrostatic field energy, calculated using FEM allows forces and moments to be obtained through the principle of virtual work. Sequentially coupled or distributed transducer models can be utilized for stability analysis.

Prior to discussing the research topics, a literature review on state-of-the-art numerical methods for the coupled field analysis will be conducted.

Table 2: Examples of present and future application areas for MEMS

Commercial Applications	Military Applications
Invasive and noninvasive biomedical sensors	Inertial systems for munitions guidance and personal navigation
Miniature biomedical analytical instruments	Distributed sensors for asset tracking, environmental and security surveillance
Cardiac management systems (e.g., pacemakers, catheters)	Weapons safing, arming, and fuzing
Drug delivery systems (e.g., insulin, analgesics)	Integrated micro-optomechanical components for identify-friend-or-foe systems
Neurostimulation	Head- and night-display systems
Engine and propulsion control	Low-power, high-density mass data storage devices
Automotive safety, braking, and suspension systems	Embedded sensors and actuators for condition-based maintenance
Telecommunication optical fiber components and switches	Integrated fluidic systems for miniature propellant and combustion control
Mass data storage systems	Miniature fluidic systems for early detection of biochemical warfare
Electromechanical signal processing	Electromechanical signal processing for low-power wireless communication
Distributed sensors for condition-based maintenance/monitoring struct. health	Active, conformable surfaces for distributed aerodynamic control of aircraft
Distributed control of aerodynamic and hydrodynamic systems	

2.0 REVIEW OF BASIC TECHNIQUES FOR MODELING MEMS

The main focus of this literature review is the presentation of an overview of the research that has been performed on the development and use of the finite element method (FEM) for solving coupled field problems of electromechanics. The various methods and techniques of coupled field simulation can be placed into four categories: uncoupled models, sequentially coupled models, lumped or reduced order models and distributed coupled field models. The following sub-sections provide brief descriptions of each of these categories and acknowledge main contributors to each of them.

2.1 UNCOUPLED MODELS

Historically, uncoupling or decoupling was the first approach widely used by designers and engineers for solving coupled field problem. Tang *et al* were the first to use decoupling for the design of lateral polysilicon combdrive transducers in 1989 [15]. The way he uncoupled the analysis was by calculating an electrostatic force developed in the combdrive using a simplified analytical electrostatic model (neglecting fringing electrostatic fields). For more than a decade, his model has been used for the design of combdrive actuators and resonators. This example is a classical representation of an uncoupled modeling technique. If electromechanical coupled field problem allows one to simplify any of the two or more physical domains (usually electrostatic one) and to analytically calculate some of the coupled parameters (usually electrostatic force), then this system can be effectively treated using uncoupled modeling technique. With the development of powerful electrostatic packages using finite element method (FEM) [16] or boundary element method (BEM) [17], the simplified

analytical models were substituted with more accurate and representative numerical models. The following are examples of how this technique was successfully applied to the various MEMS applications.

Sangster and Samper in 1997 used the uncoupled technique to create 2-D and 3-D FE electrostatic torque models of a double-stator wobble motor [18]. The electrostatic field was calculated using commercially available FE-package Opera [19]. The torque produced by an electrostatic field was obtained by integrating the electrostatic field product over the FE mesh. The authors came to the conclusion that unless the motor was of a very low axial height relative to its radius or exhibited a relatively large rotor-stator air gap, 3-D modeling was generally unnecessary. Furthermore, an analytical approximation could be used rather than the FE model if 5% torque prediction was acceptable.

Bonse in 1995 [20] applied the MAXWELL 2-D Field Simulator FE package [21] to calculate capacitance of various position sensors. The authors used a mix of FEM simulations and calculations based on the simplification of the electric field to accurately characterize microsensors without having to build and test several prototypes.

The capacitance of the combdrive fingers with non-parallel (due to the particular deep reactive ion etching process) side walls was calculated using both the MEMCAD package and simplified analytical model by Tay *et al* in 1999 [22]. The authors adjusted Tang's formula for the driving electrostatic force in perfect combdrive [15] and came to the conclusion that both analytical and simulated results were very close. Tay's group were the first to suggest that the effect of non-ideal cross section of the fingers must not be neglected in micromachined sensors that are fabricated using deep reactive etching process.

FEM wasn't just used for the simulation of the electrostatic domain. It was widely used to optimize the shape of structural elements and to calculate natural frequencies and generalized stiffnesses, which were later used as the parameters of lumped models of the structural domain. Since 1994, Fischer used ANSYS to optimize the shape of torsional micromirrors during deflection and to control their natural frequencies [23]. The FE stress analysis of thin polysilicon plates was performed by Bistue in 1997 in order to design a pressure microsensor [24]. The pressure-strain sensitivity was used to obtain the capacitance of the plate. Resonant frequencies of the microaccelerometer were calculated using ANSYS

5.4 by Li in 2001. Resonant frequencies were used to validate analytical formulation for the design of the accelerometer. The uncoupled modeling technique has been the most popular tool among the designers of MEMS for the last decade. Despite its popularity, this approach can not be applied to the analysis of strongly coupled systems, such as deflectable micromirrors, and micromotors. To overcome this shortcoming, the sequential coupling method was developed.

2.2   SEQUENTIAL COUPLING

The sequential coupling method is also called a "weak coupling" or "load vector coupling" [25]. The method is not just intuitively simple, but also relatively easy to implement. It allows the combination of strength of single field simulators for solving coupled field problems. In the case of electromechanics, electrostatic and structural solutions are obtained sequentially. Interaction (coupling) between two domains occurs through the load vector, which represents the electrostatic forces acting upon the boundaries of the structural elements. The iterative process in this case is required to obtain a reasonable solution. Therefore, the convergence of the iterative process becomes the main issue of the method.

Senturia *et al* was among the first people who suggested the sequential coupling architecture of their computer-aided design system for microelectromechanical systems (MEMCAD) [26] (Figure 1). Several years later, in 1995, CoSolve-EM program was developed *et al* [27] based on that architecture. The sequential coupling was based on a relaxation scheme combining a fast multipole-accelerated scheme for the electrostatic analysis (FASTCAP, [28]) with a standard FEM for the mechanical system analysis (ABAQUS, [29]). The approach was later successfully used for modeling electrostatic curved electrode actuators [30] and torsional micromirrors [31]. However, modeling pull-in effects and other bifurcations leaded to unresolved convergence problems [30].

The approach proposed by Wachutka *et al* in 1999 [32] also followed the idea of using FE codes for the mechanical and the electrical subproblems and coupling them through the common domain interfaces. The developed software combined BEM for modeling electrostatic domain and FEM for modeling mechanical one. The iterative method followed a Gauss-

Seidel-like relaxation scheme. The authors developed a novel technique for the treatment of unstable regions of the operating area, such as snap-down (pull-in) effect [32], where none of the usual solution schemes could converge. The homotopy method was used to tackle this problem. The new approach was shown to solve a well-known torsional micromirror contact problem [33].

Schroth *et al* in 1996 created a sequentially coupled scheme, which coupled ANSYS with the lumped circuit PSpice simulator [34]. The iterative scheme was useful but had convergence issues. The approach was used for the transient analysis of the electromechanical system of a resonant beam force sensor. One of the important features of this approach is that one can couple finite element with boundary element solutions, which is utilized in Coventor [17] commercial package, for example.

The sequential coupling between electrical and mechanical FE physics domains for MEMS analysis was also introduced in ANSYS 5.6 [35], [16] using the ESSOLV command macro. ESSOLV allowed the most general treatment of individual physics domains. However, it couldn't be applied to small signal modal and harmonic analyses because a total system eigen-frequency analysis required matrix coupling. Moreover, sequential coupling generally converged slower than the other techniques if it converged at all.

2.3   LUMPED OR REDUCED ORDER MODELS

Lumped models are usually strongly coupled and are considered to be the fastest from the convergence/solution time perspective. Moreover, they have the widest application range: from the reduced order modeling of MEMS (Spice-type compatible models) to the modeling distributed mechanical systems using lumped transducers.

One of the first strongly coupled transducer elements was introduced in ANSYS 5.6 [35], [16] to eliminate the shortcomings of sequential coupling technique. Coupling between electrostatic forces and mechanical forces was characterized by representing a microtransducer's capacitance as a function of the device's mechanical degree of freedom (stroke) [36]. The element stored electrostatic energy by converting it into mechanical energy and visa versa. The element took on the form of a lumped element with voltage and structural DOFs as

11

across variables and current and force as through variables. Input for the element consisted of a capacitance-stroke relationship that could be derived from electrostatic field solutions. The element could characterize up to three independent translation degrees of freedom at any point to simulate three-dimensional coupling. Thus, the electrostatic mesh was removed from the problem domain and replaced by a set of transducer elements hooked to the mechanical and electrical model providing a reduced order modeling (ROM) of a coupled electrostatic-structural system.

Even with the strongly coupled lumped transducers, convergence issues were experienced when applied to the difficult hysteric pull-in and release analyses [27]. The cause of the problem can be attributed to the negative total system stiffness matrix and can be resolved in ANSYS 5.7 using the augmented stiffness method.

Fedder *et al* have been designing the lumped models of the surface micromachined microresonators [37] for several years. They have developed optimization-based synthesis algorithms for designers of microresonators. The mechanical properties of the lumped transducers were verified using the ABAQUS FE package [29].

Mehner *et al* reported in 2000 successful implementation of a methodology for automatically generating reduced-order nonlinear dynamic macromodels from three-dimensional physical simulations for the conservative-energy-domain behavior [38], [39] (Figure 2). The macromodels were developed for a rapid circuit and system simulation of both non-stiffened and stiffened mechanical structures.

Lumped models allow treatment of a diverse number of analysis types, including pre-stressed modal and harmonic analyses. The Newton - Raphson nonlinear iteration converges quickly and robustly with lumped models, but it is limited geometrically to problems where the capacitance can be accurately described as a function of a single degree of freedom, usually the stroke of a comb drive. In a bending electrode problem, such as an optical switch, a single lumped transducer can not be applied. Fortunately, when the gap is small and fringing is insignificant, the capacitance between deforming electrodes can be practically modelled by several capacitors connected parallel. The EMTGEN (Electro Mechanical Transducer GENerator) command macro, introduced in ANSYS 5.7 can be applied to this case [40].

2.4 STRONGLY COUPLED DISTRIBUTED MODELS

The newest and most sophisticated method of solving coupled field problems is a strongly coupled distributed modeling technique. In this method, both the electrostatic and structural domains are modelled using distributed elements, coupled through governing electromechanical equations of equilibrium.

Aluru and White proposed to use the fastest numerical methods for treatment of each domain [41]: accelerated boundary-element methods for 3-D electrostatic analysis and FEM for the structural analysis. The nonlinear coupled system is solved using the Newton algorithm. In their paper the advantages and disadvantages of the BEM vs. FEM techniques for the static- and coupled field analysis are discussed. The FEM/FEM coupled approach, developed by Schwarzenbach in 1994 [42] is criticized, because it will require the construction of an exterior mesh for electrostatic analysis.

The first strongly coupled 2-D distributed element appeared in ANSYS 6.0 release [25]. In the ANSYS element no assumptions are made regarding the electrostatic field and the capacitance-stroke relationship is not required. The principles of virtual work and conservation of energy are the basis of the element formulation, and the coupling of the electrostatic degrees of freedom. The reaction "forces" are electrical charge and mechanical force. The FE formulation of the transducer element follows standard Ritz – Galerkin variational principles which ensures that it is compatible with regular finite elements.

Clearly, there is a lack of strongly coupled distributed modeling tools, especially for three-dimensional analysis. A significant portion of this thesis pertains to the development of a 3-D finite element to couple the electrostatic and the structural domains. Such an element could be very efficient for solving problems with dominant fringing fields.
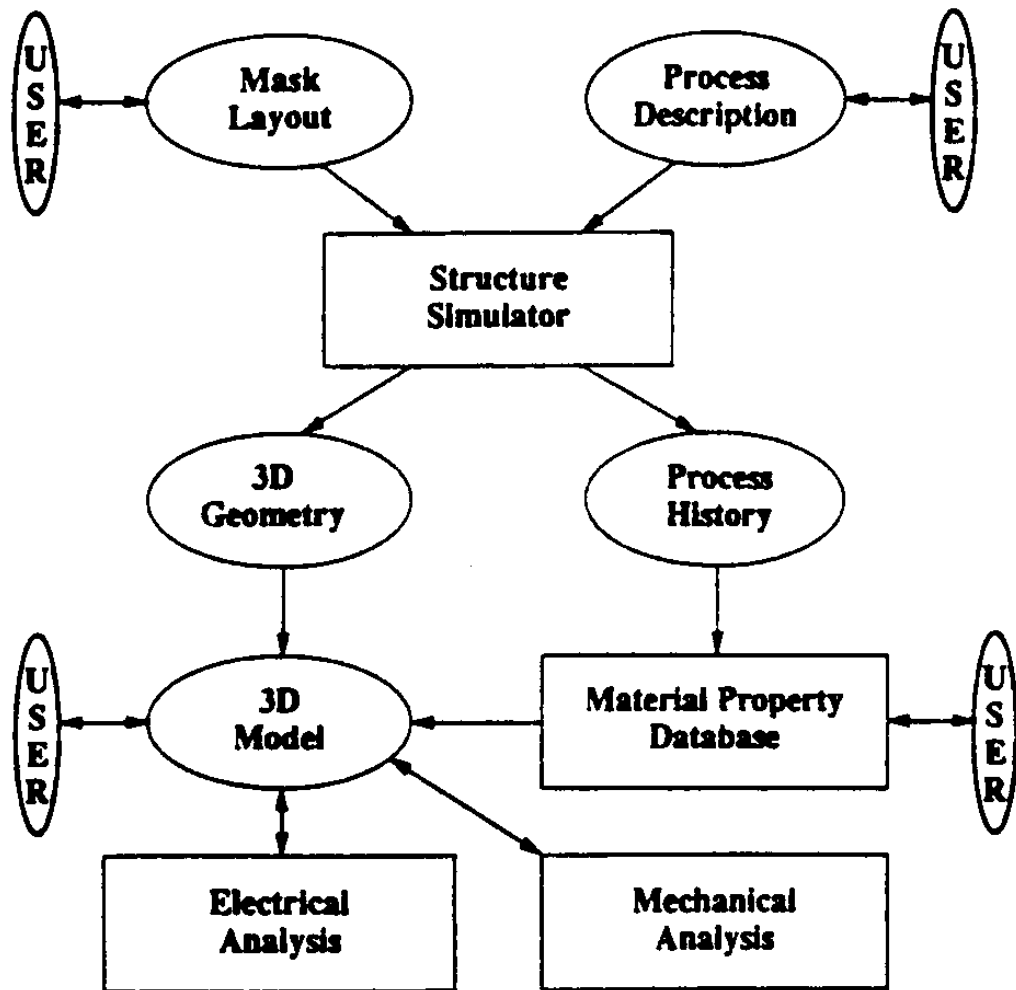
Figure 1: MEMCAD Architecture
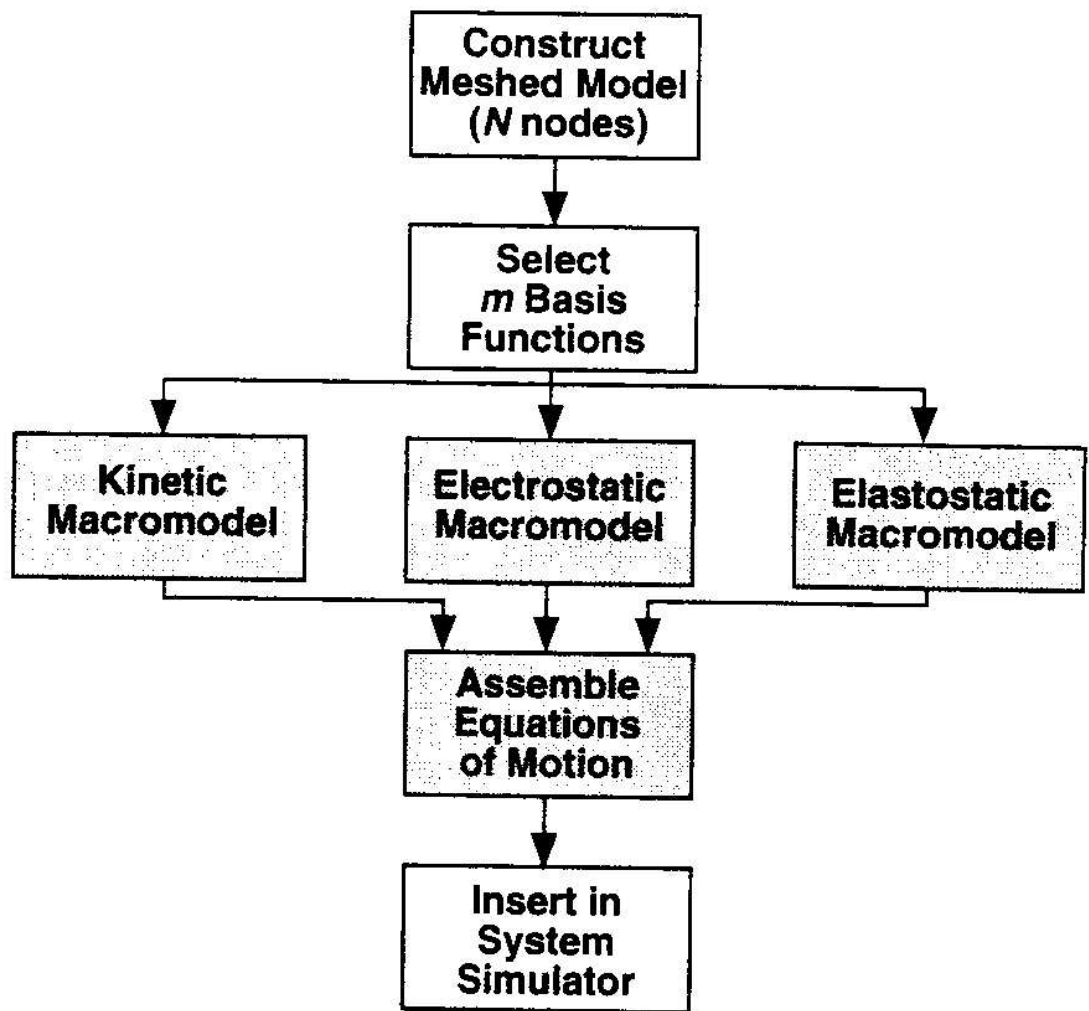
Figure 2: Overview of automated macromodeling process

3.0 GENERALIZED 2-D LUMPED TRANSDUCER FINITE ELEMENT

3.1 OVERVIEW

Lumped one-dimensional transducer elements [35] are no longer effective for modeling devices with complex geometrical configuration or where fringing electrostatic fields are dominant, such as combdrives [43], electrostatic motors [18], and microgrippers [44]. There have been several numerical methods proposed for the more accurate treatment of electro-mechanical systems, such as hybrid finite/boundary element method [45], sequential physics coupling [16], reduced order fully lumped technique [46], and distributed mechanical model with a single one-dimensional transducer [35]. These methods are often difficult to use and require extra meshing or morphing with simplifying assumptions.

The objective of this chapter is to develop a new strongly coupled lumped 2-D transducer element that fills the gap between sequential coupling and lumped 1-D element capabilities. The new strongly-coupled field transducer benefits from both sequential coupling and lumped 1-D approaches. The energy conservation and virtual work principles form the basis of the coupled field element formulation.

3.2 ELECTROMECHANICAL ENERGY CONSERVATION PRINCIPLES

The strongly coupled formulation presented in the following chapters is based on electrome-chanical energy conservation principles. The detailed review of these principles can be found in [47]. Therefore, we limit ourselves to one representative example of a system that consists of two anchored capacitor electrodes and a dielectric slab sliding between the electrodes,

suspended with a spring (see Figure 3). The absolute permittivity of space between the electrodes is denoted as ϵ_0, and the permittivity of the slab is denoted as ϵ_1. The displacement of the slab (stroke) is denoted as x.

According to electromechanical energy conservation principle [47], the net flow of energy into the lossless system (see Figure 3) is equal to the rate of change of energy stored in the system:

$$\frac{dW'_{elec}}{dt} - \frac{dW_{mech}}{dt} = \frac{dW'_{stored}}{dt} \tag{3.1}$$

In (3.1), dW'_{elec} is the differential electric energy input, dW_{mech} is the differential mechanical energy output, and dW'_{stored} is the differential change in stored energy. The electric terminal has the terminal variables voltage U and charge Q, and the mechanical terminal has the terminal variable force f and displacement x. In terms of the terminal variables, (3.1) becomes

$$U\frac{dQ}{dt} - f\frac{dx}{dt} = \frac{dW'_{stored}}{dt} \tag{3.2}$$

Multiplying both sides of (3.2) by dt we obtain:

$$dW'_{stored} = U dQ - f dx \tag{3.3}$$

The stored energy is a function of the state variables Q and x and therefore its differential is equal to:

$$dW_{stored}(Q, x) = \frac{\partial W'_{stored}}{\partial Q} dQ + \frac{\partial W'_{stored}}{\partial x} dx \tag{3.4}$$

Comparing (3.3) and (3.4) we find the terminal force and voltage:

$$f = -\frac{\partial W'_{stored}}{\partial x}, \qquad U = \frac{\partial W'_{stored}}{\partial Q} \tag{3.5}$$

The stored energy consists of two components: electrostatic field energy, $W'_{field}(Q, x)$, and mechanical spring energy, $W_{spring}(x)$:

$$W'_{stored}(Q, x) = W'_{field}(Q, x) + W_{spring}(x) \tag{3.6}$$

We assume that the system is conservative. Therefore, for any given state of the system (Q, x), the stored energy can be calculated by integrating (3.3) over any path on a state plane that leads to that given state. Assuming linearity of the relationship between capacitor's charge and potential

$$Q = CU \tag{3.7}$$

we have the following expression for the stored energy:

$$W'_{stored}(Q, x) = \frac{Q^2}{2C(x)} + \frac{kx^2}{2} \tag{3.8}$$

Plugging (3.8) into (3.5) we obtain:

$$f = \frac{Q^2 C'_x(x)}{2C(x)^2} - kx \tag{3.9}$$

$$U = \frac{Q}{C(x)} \tag{3.10}$$

For the dielectric slab system depicted in Figure 3, the capacitance is given by

$$C(x) = \frac{t\left[\epsilon_1 x + \epsilon_0(L - x)\right]}{g} \tag{3.11}$$

In (3.11), t is the electrode thickness, and g is the gap between the electrodes. For a fixed value of charge, Q , a static equilibrium state x_{eq} is a solution of the following non-linear equation ($f = 0$)

$$kx_{eq} = \frac{Q^2 g}{2t} \frac{\epsilon_1 - \epsilon_0}{\left[\epsilon_1 x_{eq} + \epsilon_0(L - x_{eq})\right]^2} \tag{3.12}$$

In the case of a fixed voltage, U, the equilibrium state has an explicit form:

$$x_{eq} = \frac{tU^2}{2gk}(\epsilon_1 - \epsilon_0) \tag{3.13}$$

It should be noted that the same value of force, f, can be computed using a coenergy [47], which is defined by:

$$W_{field}(U, x) = UQ - W'_{field}(Q, x) \tag{3.14}$$

Following the same logic as before we obtain the following expressions for the force and the charge:

$$f = \frac{\partial(W_{stored} - W_{spring})}{\partial x}, \qquad Q = \frac{\partial W_{stored}}{\partial U} \qquad (3.15)$$

For linear systems, coenergy is equal to energy. Nevertheless, forces calculated using (3.15) and (3.5) are equal to the same value for either linear or non-linear systems [47], independent of whether the energy or coenergy approached are employed.

3.3   GOVERNING NON-LINEAR FINITE ELEMENT EQUATIONS

The full FE model of an electromechanical system, most typically a MEMS device, consists of classical mechanical elements (lumped or distributed) and transducer finite elements. The mechanical elements are used to model the electrodes and suspension structure. They store or dissipate mechanical energy (elastic and kinetic). The space between the electrodes (electrostatic domain) is modelled with the transducers, that store electrostatic energy (magnetic energy is neglected).

The transducers have a vector of electrical potentials, $\mathbf{u}$, and a vector of structural displacements, $\mathbf{x}$, as nodal degrees of freedom. The reactions are the vector of electric charges, $\mathbf{q}$, and a vector of mechanical forces, $\mathbf{f}$. In a standard electrostatic FE model the mesh remains geometrically intact throughout the solution. In the transducer elements, nodes move morphing the mesh. The vector of new (deformed) node coordinates, $\mathbf{X}$, is computed as the sum of the vector of original node coordinates, $\mathbf{X}_o$, and the displacement vector ($\mathbf{X} = \mathbf{X}_o + \mathbf{x}$). Element quantities, such as energy and electric field, are now functions of $\mathbf{x}$ and $\mathbf{u}$.

The new transducer formulation is based on Ritz - Galerkin variational principles [25]. The total potential energy is a sum of electrostatic and mechanical energies

$$W'(\mathbf{x}, \mathbf{q}) = W'_{elec}(\mathbf{x}, \mathbf{q}) + W_{mech}(\mathbf{x}) \qquad (3.16)$$
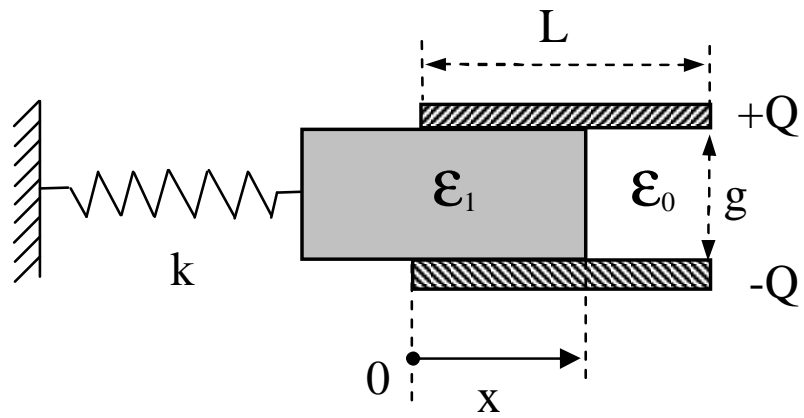
(a) Schematic representation
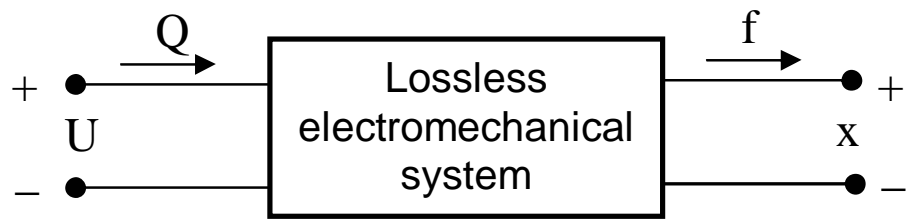
(b) Terminal representation

Figure 3: Dielectric slab capacitor (illustration of energy formulation)

The energy change due to electric potential and displacement changes produces reactions charges and mechanical forces. The vectors of nodal mechanical forces, $\mathbf{f}$, and electric charges, $\mathbf{q}$, are calculated using energy conservation principle:

$$\mathbf{f}(\mathbf{x}, \mathbf{u}) = \frac{\partial W(\mathbf{x}, \mathbf{u})}{\partial \mathbf{x}} = \frac{\partial W_{elec}(\mathbf{x}, \mathbf{u})}{\partial \mathbf{x}} - \frac{\partial W_{mech}(\mathbf{x})}{\partial \mathbf{x}} \qquad (3.17)$$

$$\mathbf{q}(\mathbf{x}, \mathbf{u}) = \frac{\partial W(\mathbf{x}, \mathbf{u})}{\partial \mathbf{u}} = \frac{\partial W_{elec}(\mathbf{x}, \mathbf{u})}{\partial \mathbf{u}} = \mathbf{C}(\mathbf{x})\mathbf{u} \qquad (3.18)$$

At the equilibrium state, these forces balance each other on the internal nodes of the transducer mesh and balance applied external forces on the external nodes ($\mathbf{f}_{ext}$ and $\mathbf{q}_{ext}$). This ensures the compatibility of the transducer elements with the regular mechanical elements. In most practical cases, the system of equilibrium equations is linear from an electrical point of view, but highly non-linear from a mechanical point of view. The non-linear system of a coupled field equilibrium equations of statics is given by:

$$\begin{bmatrix} \mathbf{f}(\mathbf{x}, \mathbf{u}) \\ \mathbf{q}(\mathbf{x}, \mathbf{u}) \end{bmatrix} = \begin{bmatrix} \mathbf{f}_{ext} \\ \mathbf{q}_{ext} \end{bmatrix} \qquad (3.19)$$

Equation (3.19) in a form of the Newton - Raphson method [48] is given by:

$$\begin{bmatrix} \mathbf{K}_{xx}(\mathbf{x}, \mathbf{u}) & \mathbf{K}_{xu}(\mathbf{x}, \mathbf{u}) \\ \mathbf{K}_{ux}(\mathbf{x}, \mathbf{u}) & \mathbf{K}_{uu}(\mathbf{x}, \mathbf{u}) \end{bmatrix} \begin{bmatrix} \Delta \mathbf{x} \\ \Delta \mathbf{u} \end{bmatrix} = \begin{bmatrix} \Delta \mathbf{f}(\mathbf{x}, \mathbf{u}) \\ \Delta \mathbf{q}(\mathbf{x}, \mathbf{u}) \end{bmatrix} \qquad (3.20)$$

In (3.20), $\Delta \mathbf{x}$ and $\Delta \mathbf{u}$ are the increments of nodal displacements and potentials, $\Delta \mathbf{f}(\mathbf{x}, \mathbf{u})$ and $\Delta \mathbf{q}(\mathbf{x}, \mathbf{u})$ are the out-of-balance nodal forces and charges, and the blocks of the tangent stiffness matrix, $\mathbf{K}$, are given by

$$\mathbf{K}_{xx}(\mathbf{x}, \mathbf{u}) = \frac{\partial \mathbf{f}(\mathbf{x}, \mathbf{u})}{\partial \mathbf{x}} = \frac{\partial^2 W(\mathbf{x}, \mathbf{u})}{\partial \mathbf{x}^2} \qquad (3.21)$$

$$\mathbf{K}_{xu}(\mathbf{x}, \mathbf{u}) = \frac{\partial \mathbf{f}(\mathbf{x}, \mathbf{u})}{\partial \mathbf{u}} = \frac{\partial^2 W(\mathbf{x}, \mathbf{u})}{\partial \mathbf{x} \partial \mathbf{u}} \qquad (3.22)$$

$$\mathbf{K}_{ux}(\mathbf{x}, \mathbf{u}) = \frac{\partial \mathbf{q}(\mathbf{x}, \mathbf{u})}{\partial \mathbf{x}} = \frac{\partial^2 W(\mathbf{x}, \mathbf{u})}{\partial \mathbf{u} \partial \mathbf{x}} \qquad (3.23)$$

$$\mathbf{K}_{uu}(\mathbf{x}, \mathbf{u}) = \frac{\partial \mathbf{q}(\mathbf{x}, \mathbf{u})}{\partial \mathbf{u}} = \frac{\partial^2 W(\mathbf{x}, \mathbf{u})}{\partial \mathbf{u}^2} = \mathbf{C}(\mathbf{x}) \qquad (3.24)$$

The mesh, including the structural domain and the air region, deform to reach force equilibrium. The original nodes are constantly updated according to the electromechanical force equilibrium. This procedure is highly non-linear and huge displacements are allowed for an arbitrary uneven mesh. For the transient, modal or harmonic coupled field FE analysis, in addition to the stiffness matrix given by (3.21) - (3.24), the mass and damping matrices of the mechanical domain have to be calculated using standard mechanical FEM. The transducer element is also compatible to network electrical elements [40], which allows for static, transient, modal, and harmonic network analyses.

3.4   TRANSDUCER ELEMENT ARCHITECTURE AND BASIC ASSUMPTIONS

The generalized 2-D transducer element is designed for solving static electromechanical problems where electrostatic field lines are straight or slightly curved (i.e. fringing effects are ignored) [49]. This class of problems includes but is not limited to micromirrors, microgrippers, RF switches and certain combdrive geometries (Figure 4). A structural domain is modelled using either plane (strain or stress) or beam elements (Figure 5).

The new transducer links together two parallel or slightly tilted electrodes with the potential difference denoted as V, providing a strong coupling between electrostatic and mechanical domains. The electrostatic field, E, created by the electrodes is schematically depicted in Figure 5. The transducer shares nodes with the mechanical finite element models of both electrodes.

The schematic picture of the new transducer element in Figure 5 shows that the element has a trapezoidal shape with two sides tangent to the surfaces of the electrodes. There are three degrees of freedom per each node: horizontal component of displacement vector, U_x, vertical component of displacement vector, U_y, and an electrostatic potential, V. Three forces associated with each node are: horizontal component of mechanical force vector, f_x, vertical component of mechanical force vector, f_y, and electrical charge, q (see Figure 5).

For the sake of simplicity, we will assume that only nodes 1 and 2 are active, because in a vast majority of applications, the mechanical and electrostatic degrees of freedom of the ground (nodes 3 and 4) are fixed and equal to zero. Finally, it will be assumed that the top electrode is equipotential, which means that $V^{(1)} = V^{(2)} = V$.

3.5 TRANSDUCER FINITE ELEMENT VECTORS AND MATRICES

After applying all the assumptions, the number of element degrees of freedom is reduced to five. The vector of element unknowns is given by:

$$\mathbf{U}^{(e)} = [U_x^{(1)}, U_y^{(1)}, U_x^{(2)}, U_y^{(2)}, V]^T \tag{3.25}$$

The transducer element stores only electrostatic potential energy. The element coenergy, W_e, of an entire electrostatic domain (space between the electrodes) is computed by assembling all transducer elements:

$$W_e = \sum_{e=1}^{NE} W_e^{(e)} = \sum_{e=1}^{NE} \frac{V^2}{2} C^{(e)} \tag{3.26}$$

In (3.26), NE is the number of transducer elements and $C^{(e)}$ is the element capacitance, which is a function of element's geometry. The element vector of nodal forces, $\mathbf{F}_e^{(e)}$, produced by changing electrostatic field is calculated using virtual work principle:

$$\mathbf{F}_e^{(e)} = \frac{\partial W_e^{(e)}}{\partial \mathbf{U}^{(e)}} = \begin{bmatrix} \frac{\partial W_e^{(e)}}{\partial U_x^{(1)}} \\ \frac{\partial W_e^{(e)}}{\partial U_y^{(1)}} \\ \frac{\partial W_e^{(e)}}{\partial U_x^{(2)}} \\ \frac{\partial W_e^{(e)}}{\partial U_y^{(2)}} \\ \frac{\partial W_e^{(e)}}{\partial V} \end{bmatrix} = \frac{V^2}{2} \begin{bmatrix} \frac{\partial C^{(e)}}{\partial U_x^{(1)}} \\ \frac{\partial C^{(e)}}{\partial U_y^{(1)}} \\ \frac{\partial C^{(e)}}{\partial U_x^{(2)}} \\ \frac{\partial C^{(e)}}{\partial U_y^{(2)}} \\ \frac{\partial C^{(e)}}{\partial V} \end{bmatrix} = \begin{bmatrix} f_x^{(1)} \\ f_y^{(1)} \\ f_x^{(2)} \\ f_y^{(2)} \\ q \end{bmatrix} \tag{3.27}$$

In order to compute $\mathbf{F}_e^{(e)}$, we have to know the element capacitance, $C^{(e)}$. A tilted capacitor model can be used to calculate $C^{(e)}$ [14]:

$$C^{(e)} = C^{(e)}(\theta) \approx \frac{\epsilon w}{\theta} \ln\left(\frac{2g_0 + L\theta}{2g_0 - L\theta}\right) \tag{3.28}$$
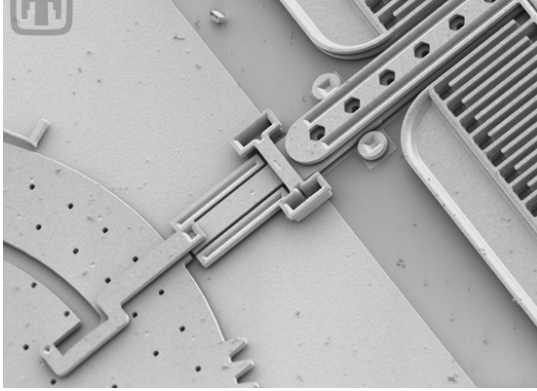
(a) Courtesy of Sandia NL
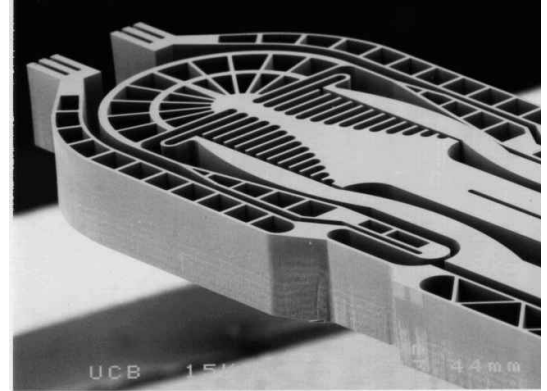
(c) Courtesy of UCB
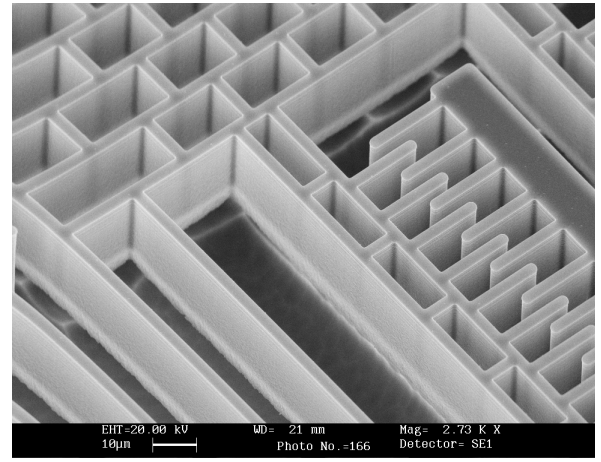
Figure 4: Surface and bulk micromachined MEMS for 2-D analysis: (a) and (b) surface micromachined MEMS; (c) and (d) bulk micromachined MEMS

Electrode 1

$\underline{E}$

V

Electrode 2

$f_y^{(1)}$

$q^{(1)}$

$u_x^{(2)}$,
$u_y^{(2)}$,
$V^{(2)}$

2

1

$f_x^{(1)}$

3

4

x
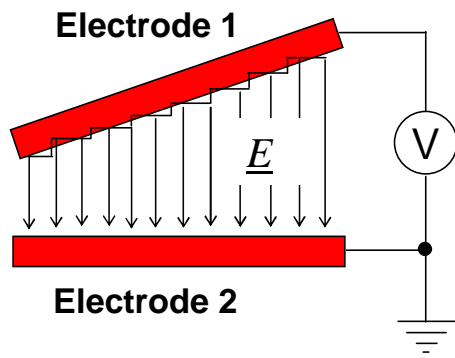
(a) Physical element model
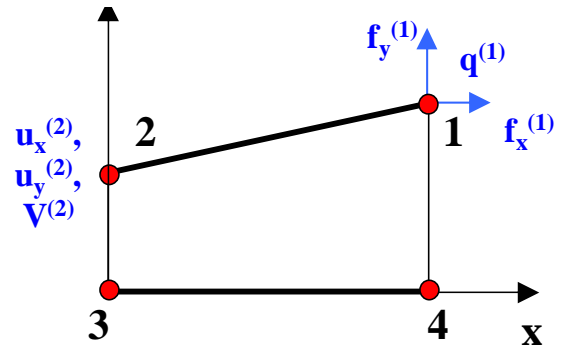
(b) Mathematical element model

**Structural 2D or
BEAM elements**

Figure 5: Two-dimensional lumped element model

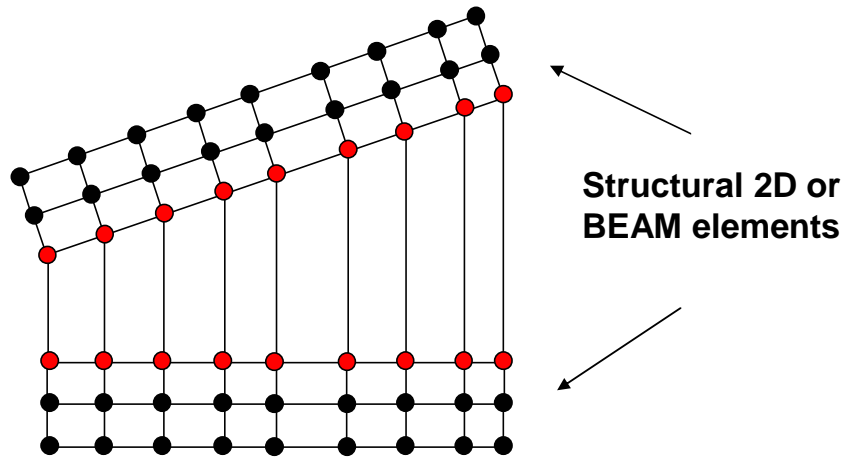In (3.28), θ is the angle between the electrodes, ϵ is the space permittivity constant, w is the electrode width (in a direction normal to this page), g_0 is the average gap between two electrodes, and L is the length of the ground (bottom) electrode. It is important to remember that this model is derived from the assumption that the angle θ is small and, therefore, the field lines are only slightly curved [50].

The expression for $C^{(e)}$, given by (3.28) can be rewritten in terms of element nodal coordinates, x_1, y_1, x_2, and y_2:

$$C^{(e)} = C^{(e)}(x_1, y_1, x_2, y_2) = \epsilon w \left(\frac{x_2 - x_1}{y_2 - y_1} \right) \ln \left(\frac{y_2}{y_1} \right), \qquad y_1 \neq y_2 \qquad (3.29)$$

$$C^{(e)} = C^{(e)}(x_1, y_1, x_2, y_2) = 2\epsilon w \left(\frac{x_1 - x_2}{y_1 + y_2} \right), \qquad y_1 = y_2 \qquad (3.30)$$

The element nodal coordinates are the sum of original (non-deformed) coordinates and the nodal displacements:

$$x_1 = (x_1)_0 + U_x^{(1)}, \qquad y_1 = (y_1)_0 + U_y^{(1)}, \qquad x_2 = (x_2)_0 + U_x^{(2)}, \qquad y_2 = (y_2)_0 + U_y^{(2)} \qquad (3.31)$$

Therefore, the differentials of the nodal coordinates are equal to the differentials of the nodal displacements:

$$dx_1 = dU_x^{(1)}, \qquad dy_1 = dU_y^{(1)}, \qquad dx_2 = dU_x^{(2)}, \qquad dy_2 = dU_y^{(2)} \qquad (3.32)$$

Now, we can use the differentials of nodal coordinates to calculate the nodal forces (see Appendix A), given by (3.27). For small displacements and voltage change (dx_i, dy_i and dV_i, $i = 1, 2$), we have:

$$f_x^{(i)} = f_{x0}^{(i)} + K_{xx}^{(ij)} dx_i + K_{xy}^{(ij)} dy_i + K_{xv}^{(ij)} dV_i \qquad (3.33)$$

$$f_y^{(i)} = f_{y0}^{(i)} + K_{yx}^{(ij)} dx_i + K_{yy}^{(ij)} dy_i + K_{yv}^{(ij)} dV_i \qquad (3.34)$$

$$q^{(i)} = q_0^{(i)} + K_{vx}^{(ij)} dx_i + K_{vy}^{(ij)} dy_i + K_{vv}^{(ij)} dV_i \qquad (3.35)$$

The forces given by (3.33)-(3.35) are the entries for a Newton - Raphson algorithm of solving a non-linear problem [48]. In (3.33) - (3.35), the Newton - Raphson restoring forces from

26

a previous equilibrium increment are denoted as $f_{x0}^{(i)}$, $f_{y0}^{(i)}$, and $q_0^{(i)}$, while the components of the tangent stiffness matrix are denoted as $K_{q,r}^{(ij)}$ ($q, r = x, y, u$ and $i, j = 1, 2$). These components are given by:

$$K_{xx}^{(ij)} = \frac{\partial f_x^{(i)}}{\partial x_j}, \quad K_{xy}^{(ij)} = \frac{\partial f_x^{(i)}}{\partial y_j}, \quad K_{xv}^{(ij)} = \frac{\partial f_x^{(i)}}{\partial V_j}$$

$$K_{yx}^{(ij)} = \frac{\partial f_y^{(i)}}{\partial x_j}, \quad K_{yy}^{(ij)} = \frac{\partial f_y^{(i)}}{\partial y_j}, \quad K_{yv}^{(ij)} = \frac{\partial f_y^{(i)}}{\partial V_j}$$

$$K_{vx}^{(ij)} = \frac{\partial q^{(i)}}{\partial x_j}, \quad K_{vy}^{(ij)} = \frac{\partial q^{(i)}}{\partial y_j}, \quad K_{vv}^{(ij)} = \frac{\partial q^{(i)}}{\partial V_j} \quad\quad (3.36)$$

Thus, the transducer element is completely defined by the expressions for the element nodal forces (3.33)-(3.35) and the expressions for a tangent stiffness matrix (3.36).

3.6   VERIFICATION PROBLEMS

3.6.1   Parallel plate capacitive transducer

In this section several problems will be solved to validate the new transducer element. As a first example, we will compute a static equilibrium state of a parallel plate capacitive transducer schematically, as shown in Figure 6. The transducer consists of two electrodes separated by a gap that is a function of applied voltage and a stiffness of a suspending spring. The problem has an analytical solution for rigid electrodes and a lumped spring without accounting for fringing electrostatic fields. The top electrode is modelled as a flexible solid body fixed at the top surface.

Two finite element models are used to compute a static equilibrium of the system: (1) 2-D generalized transducer element model and (2) 1-D lumped transducer element, TRANS126 [40] (reference solution).

In the first model, the top electrode is meshed with plane stress two-dimensional quadrilateral elements [16] (see Figure 7). The Young's modulus is 10 Pa and Poisson's ratio is equal to zero. A unit voltage is applied across the electrodes. The nonlinear static problem

27

of electroelasticity is solved using a sparse FE solver [16]. The vertical displacement field is depicted in Figure 8 for the first model and the second model in Figure 9.

The solution obtained using the new element converged two times slower than the reference solution (Figure 10). This can be attributed to the fact that the reference solution was obtained using a one-dimensional lumped element (TRANS126). The vertical electrode displacement (stroke) vs. the potential drop, V, is depicted in Figure 11. Both, the new transducer element and the reference lumped element produce very close results (the difference is within 0.1% margin).

3.6.2 Clamped beam electrode bending

The second problem is considered to be a standard benchmark for coupled-field codes. The problem was introduced by Gilbert *et al* in 1996 [51]. The experimental data was used to a verify sequential coupling tool (CoSolve-EM). In this problem, a clamped-clamped charged beam is suspended over a grounded substrate with the insolation contact layer deposited on top (see Figure 12). The problem is defined by the following parameters: the free space permittivity is $8.854 \cdot 10^{-6}$ pF /μm, the beam length is 80 μm, the beam thickness is 10 μm, the beam height is 0.5 μm, the air gap is 0.6 μm, the Young's modulus (silicon) is 169.0 GPa, and the contact layer thickness is 0.1 μm.

Only a half of the beam is modelled due to symmetry. The air gap between the contact layer and the beam is meshed with the new transducer elements (see Figure 13). The beam is meshed with plane strain structural elements, PLANE45 [40]. The potential drop, V, is applied between the beam and the ground. The maximum beam deflection (tip deflection) is a function of V. The original and deformed mesh are depicted in Figures 14 and 15.

The results of the static analysis (tip displacement as a function of the potential drop) are compared with the reference solution obtained using the sequential coupling technique (ESSOLV) [40]. Comparison of the CPU time vs. the element size is depicted in Figure 16. It can be seen, that the solution time for the new element varies between five and ten seconds for the element size varying between 0.5 μm and 4.0 μm. The ESSOLV solution time, for the fastest case (element size 4.0 μm), is about 27 seconds, which is almost seven

times longer than the new element solution time. Comparison of the converged (in terms of the element size) ESSOLV tip deflection and the new element solution is shown in Figure 17. Considering the ESSOLV solution as a reference one (it is eventually the same as one presented in [51]). The Figure 17 demonstrates the importance of the mesh sensitivity analysis. The tip deflection varies from -0.067 μm to -0.0725 μm.

Finally, the hysteresis behavior of the beam is demonstrated in Figure 18. The tip deflection increases when the potential increases until a bifurcation point is reached. When $V = 18V$, the beam reaches an unstable equilibrium point. Increasing voltage carries the system into the unstable solution and the beam snaps down to the contact layer (pull-in). When the contact occurs, the attractive electrostatic force becomes sufficiently higher than the repulsive structural force. Therefore, it takes much lower voltage (about $12V$) to release the beam. The hysteresis behavior is well known and called pull-in/release phenomena. Figure 18 shows that the new element produces results virtually indistinguishable from the results obtained using ESSOLV ANSYS macro.

3.7 SUMMARY

A lumped 2-D transducer element formulation was developed in this chapter for modeling a wide range of MEMS devices. The computer code was developed for the ANSYS platform and benchmark problems were solved. A major assumption was made to neglect fringing fields, which proved to be accurate and effective for the class of devices studied. The developed lumped element models were much faster than the sequential coupling models, and they maintained the same level of accuracy. Based on the benchmark problems, hysteresis problems with contact can be effectively solved using the new element. It allows the modeling of a great variety of real-world problems. However, for systems with dominant fringing fields, such as combdrives, motors, mirrors, distributed coupled field models are still required.
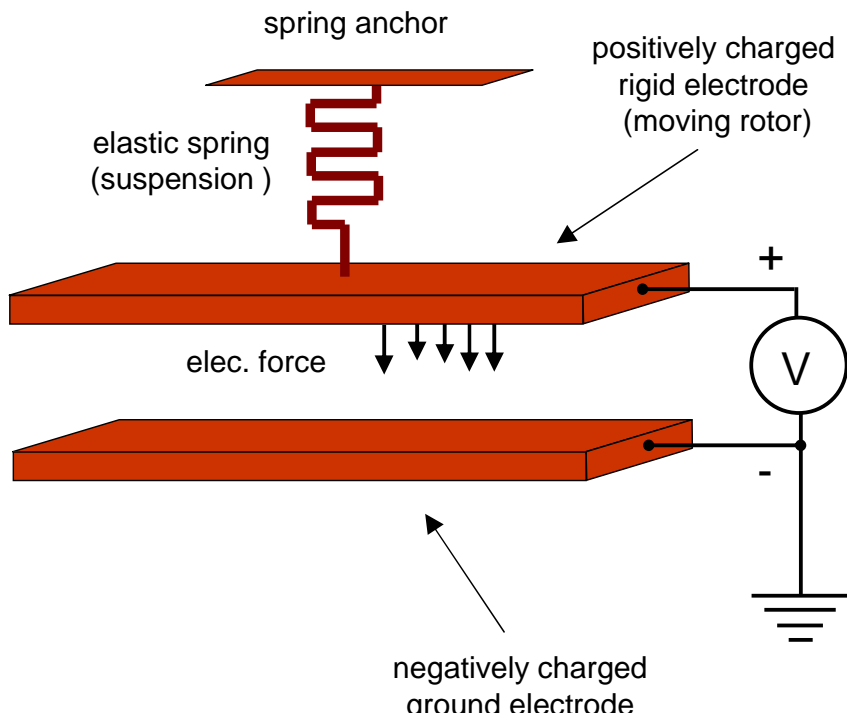
Figure 6: Parallel plate capacitive transducer (scheme)
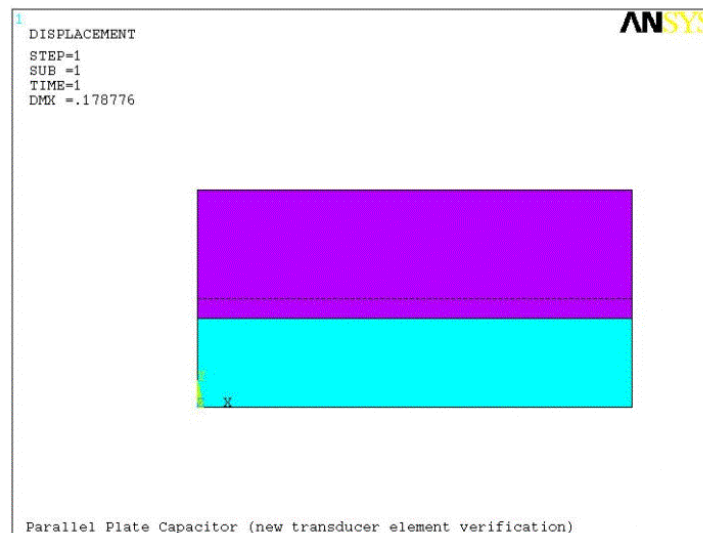
Figure 7: Deformed mesh (first model – flexible top electrode)
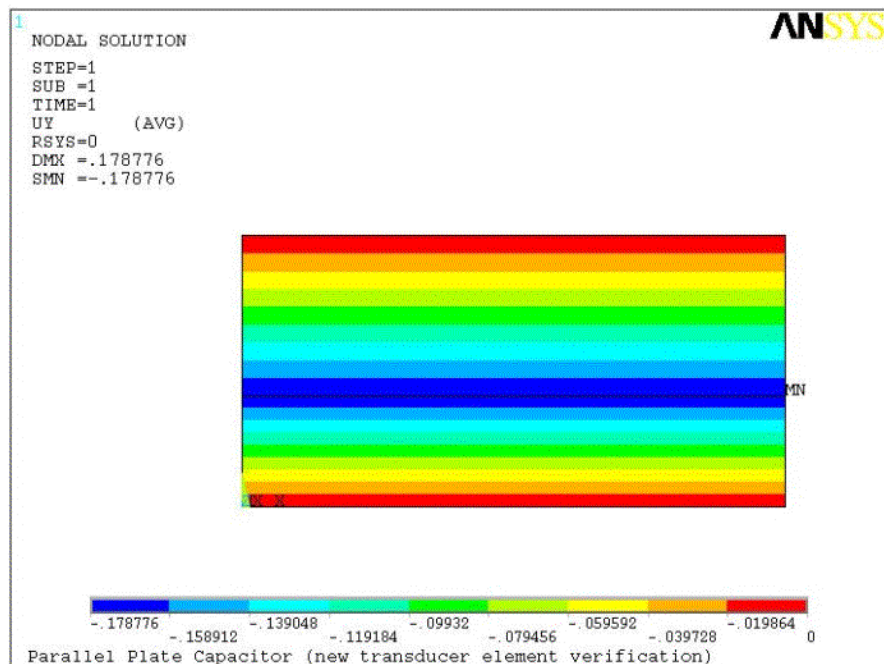
Figure 8: Vertical displacement field (solid elastic model)
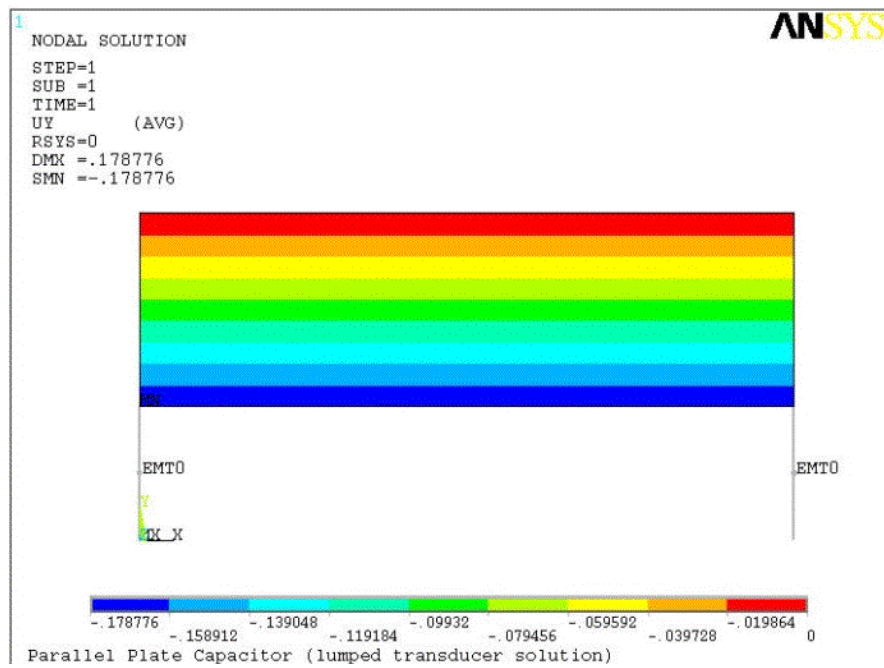
Figure 9: Vertical displacement field (lumped spring model)
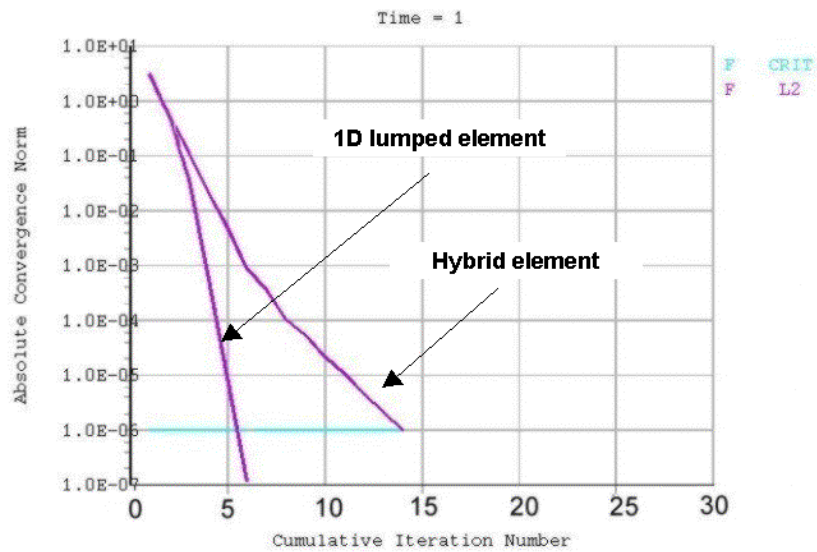
Figure 10: Convergence of a nonlinear solution
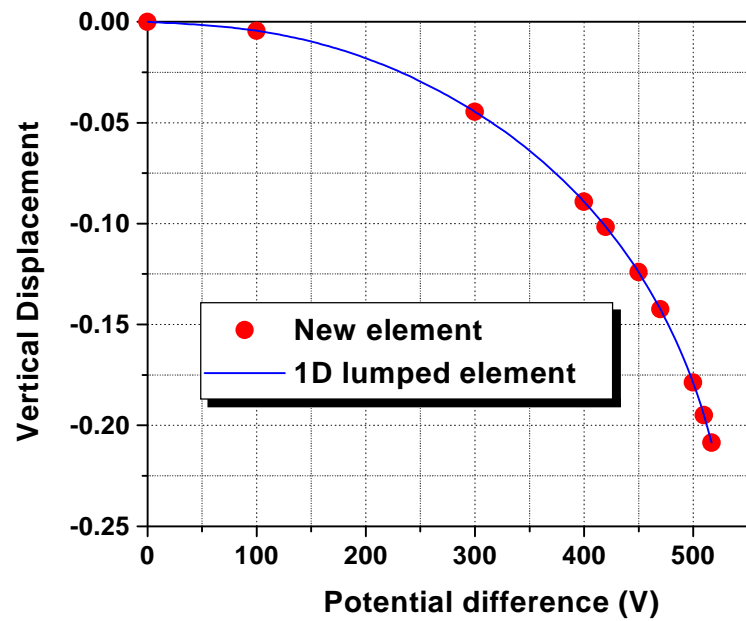
Figure 11: Vertical displacement of the top electrode vs. applied voltage
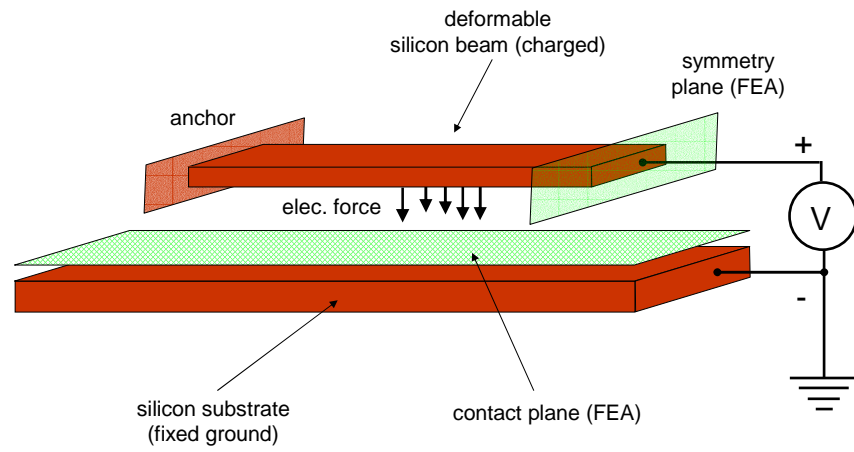
Figure 12: Bending of a clamped beam with contact and hysteresis
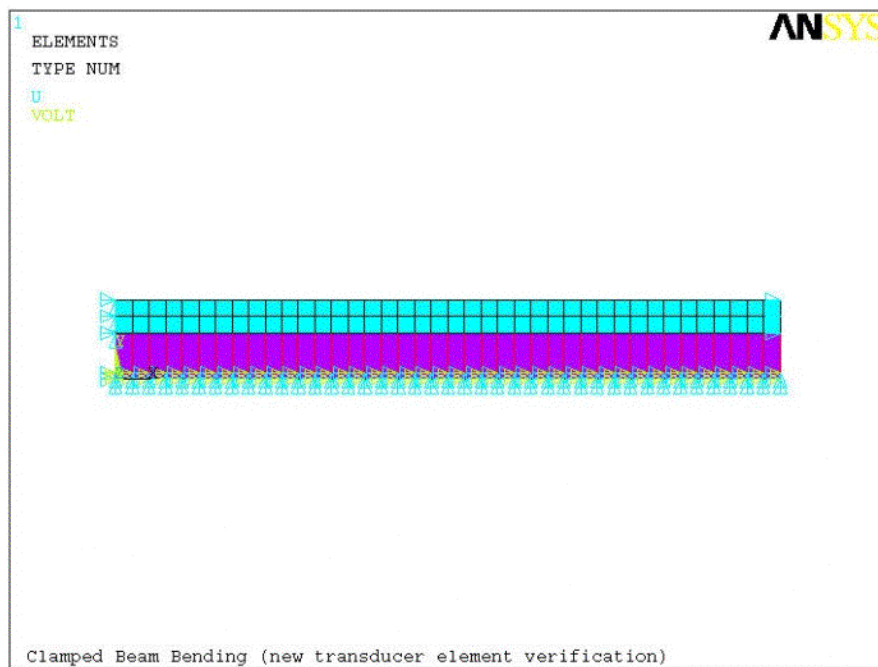
Figure 13: Fragment of finite element model of the beam (structural and transducer elements)
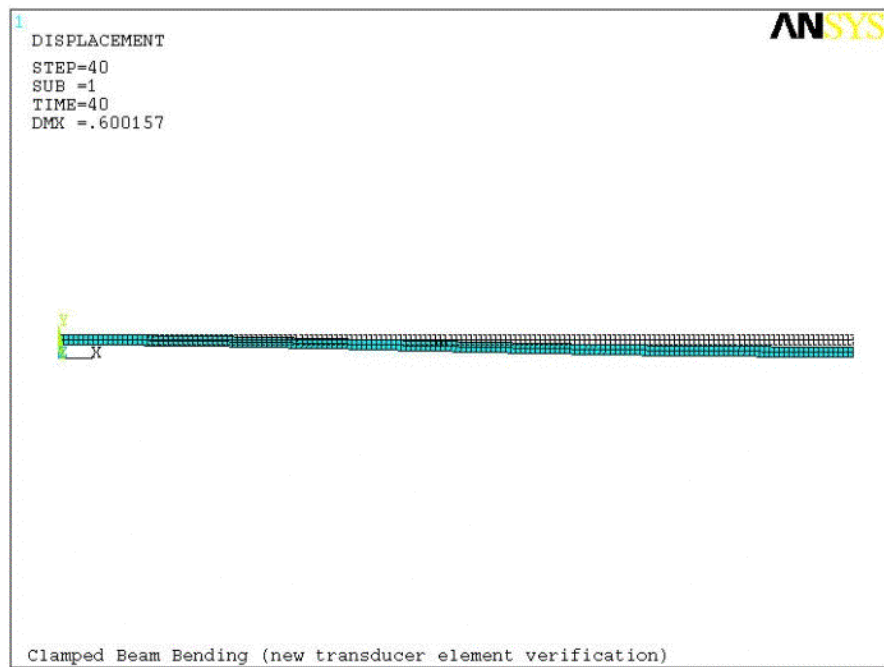
Figure 14: Deformed mesh (structural and transducer elements)
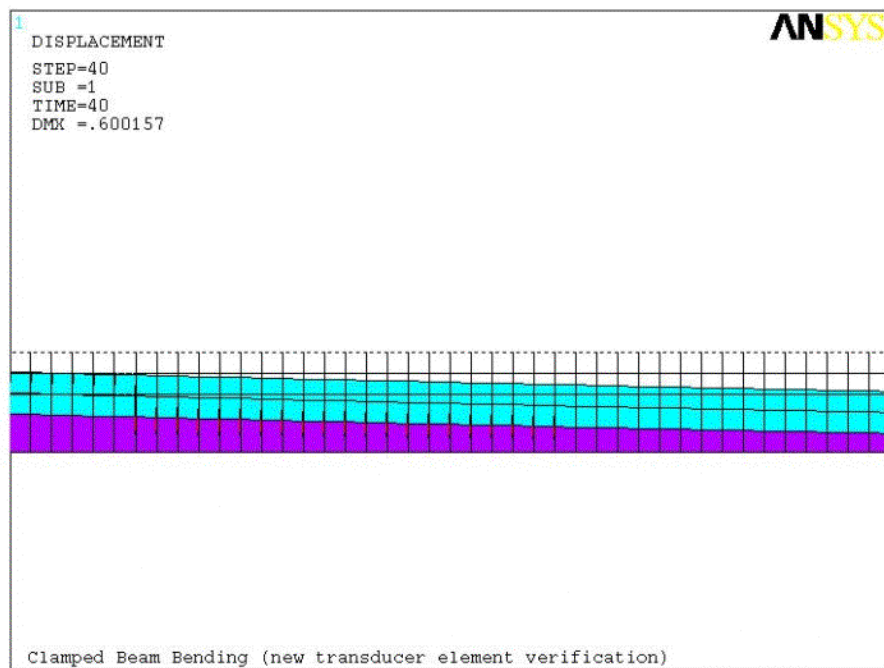
Figure 15: Fragment of the deformed mesh (structural and transducer elements)
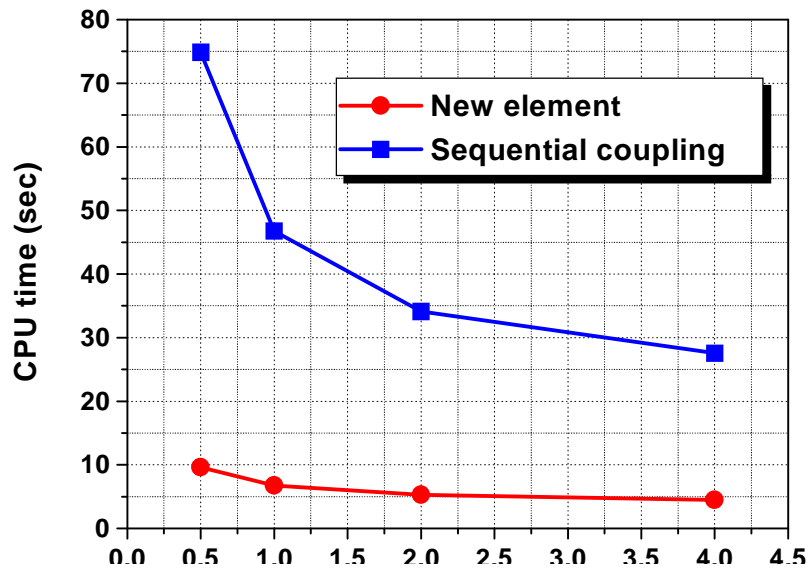
Figure 16: CPU time of the nonlinear solution vs. element size
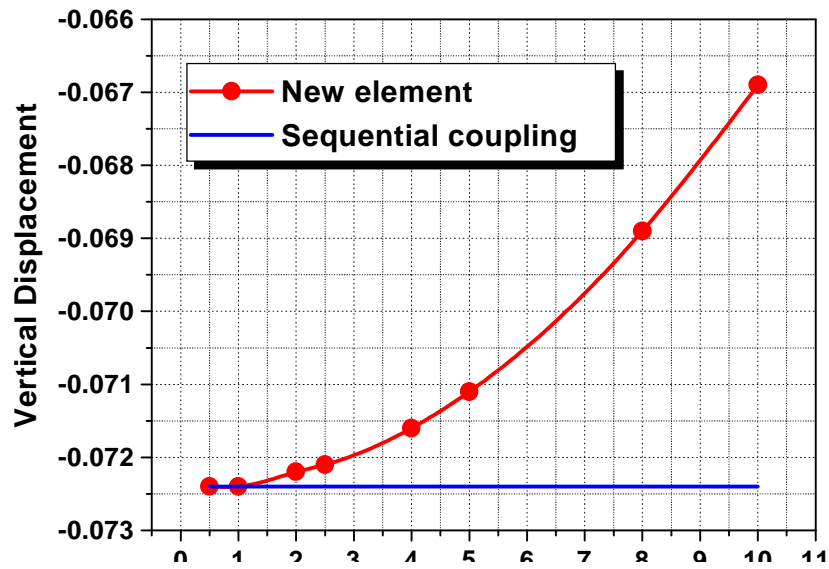
Figure 17: Tip vertical displacement vs. element size

35
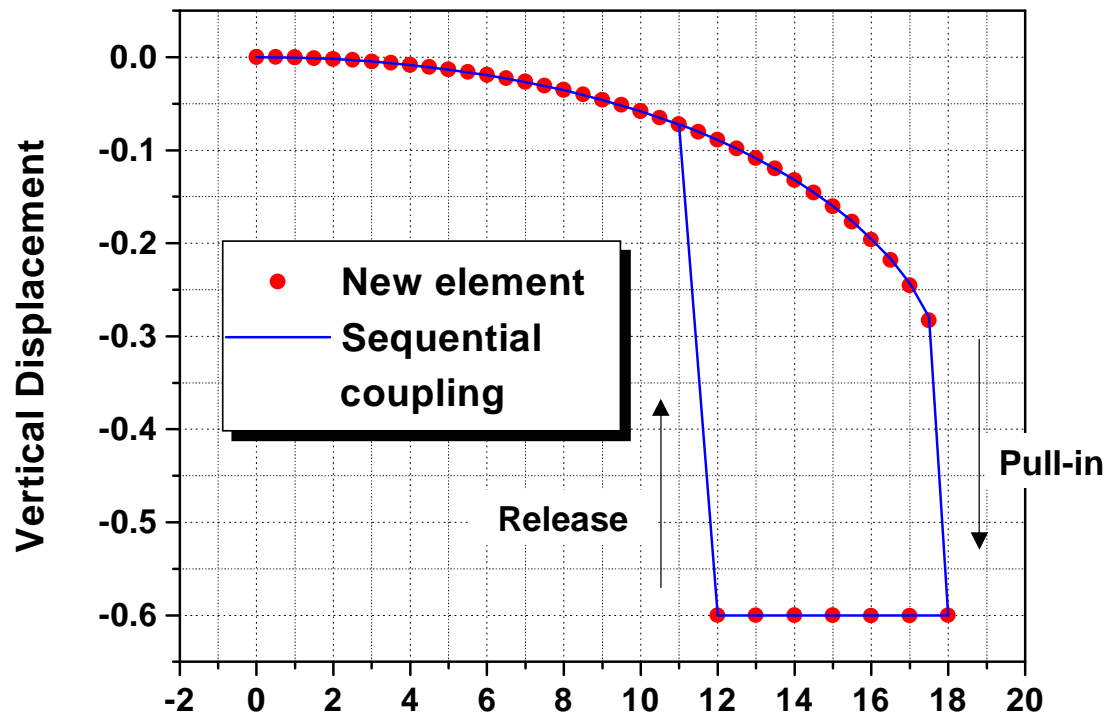
Figure 18: Hysteresis loop: vertical tip displacement vs. potential drop

4.0 3-D STRONGLY COUPLED TETRAHEDRAL TRANSDUCER FINITE ELEMENT

4.1 OVERVIEW

The increased functionality of MEMS fabrication and production techniques has lead to the ability of creating devices and components with complex geometrical configurations. These components require efficient FE modeling techniques to solve coupled electromechanical problems. The lumped models are no longer applicable for devices, such as combdrives or electrostatic motors, where fringing electrostatic fields are dominant. There have been several numerical methods proposed for the treatment of electromechanical systems including: FE or boundary element methods using sequential physics coupling; strongly coupled but reduced order methods using fully lumped or mechanically distributed but electrically lumped 1-D, multi-dimensional or modal-space transducers. All of these methods need some extra meshing or morphing, introduce simplifying assumptions and may not be convenient to use. This chapter introduces a distributed strongly coupled electromechanical transducer finite element with internal morphing capability for full and accurate modeling the underlying physical phenomena. The new transducer can be used in a FE model with classical lumped and/or solid mechanical elements. The element formulation follows similar logic to the 2-D lumped element presented in Chapter 3.

4.2 TRANSDUCER ELEMENT COENERGY

The transducer element's potential energy (coenergy) is associated with the electrostatic field. The coenergy of the whole system, $W_{elec}(\mathbf{x}, \mathbf{u})$, is computed by assembling all transducer elements together and is given by

$$W_{elec}(\mathbf{x}, \mathbf{u}) = \sum_{i=1}^{NT} W^{(i)} = \frac{1}{2} \mathbf{u}^T \mathbf{C}(\mathbf{x}) \mathbf{u} \tag{4.1}$$

In (4.1), NT is the number of assembled transducers, $\mathbf{x}$ and $\mathbf{u}$ are the vectors of nodal displacements and potentials, and $\mathbf{C}(\mathbf{x})$ is the system capacitance matrix. This is similar to classical electrostatic FE capacitance matrix. The difference is that the transducers are morphing, so that the capacitance matrix depends on nodal coordinates and displacements [52].

The 3-D transducer element has a tetrahedral shape with the geometry fully defined by coordinates of four nodes (see Figure 19). Each element node has four degrees of freedom: three coordinates of a nodal displacement vector defined in a global Cartesian coordinate system, u_x, u_y, and u_z, and potential of electrostatic field, U. The electrostatic coenergy of an individual transducer element, $W^{(e)}$, is given by:

$$W^{(e)} = \frac{1}{2} \int_V \epsilon \mathbf{E}^2 dv = \frac{1}{2} \int_V \epsilon grad^2 U dv \tag{4.2}$$

In (4.2), ϵ is the element permittivity (material property of the element), V is the element volume, $\mathbf{E}$ is the electric field vector, and U is the electrostatic potential. For a linear tetrahedral element with a constant permittivity the integral in (4.2) can be evaluated analytically

$$W^{(e)} = \frac{\epsilon V}{2} grad^2 U = \frac{\epsilon V}{2} \sum_{i=1}^{4} \sum_{j=1}^{4} \frac{\mathbf{n}_i \cdot \mathbf{n}_j}{h_i h_j} U_i U_j = \left(\mathbf{u}^{(e)}\right)^T \mathbf{C}^{(e)}(\mathbf{x}) \mathbf{u}^{(e)} \tag{4.3}$$

In (4.3), h_i are the tetrahedral altitudes, $\mathbf{n}_i$ are the inner face normals, $\mathbf{u}^{(e)}$ is the element vector of nodal potentials, and $\mathbf{C}^{(e)}(\mathbf{x})$ is the element capacitance matrix (see Figure 19). Note, that in (4.3), the energy is a function of nodal potentials (scalars) and tetrahedral geometry is invariant of the coordinate system.
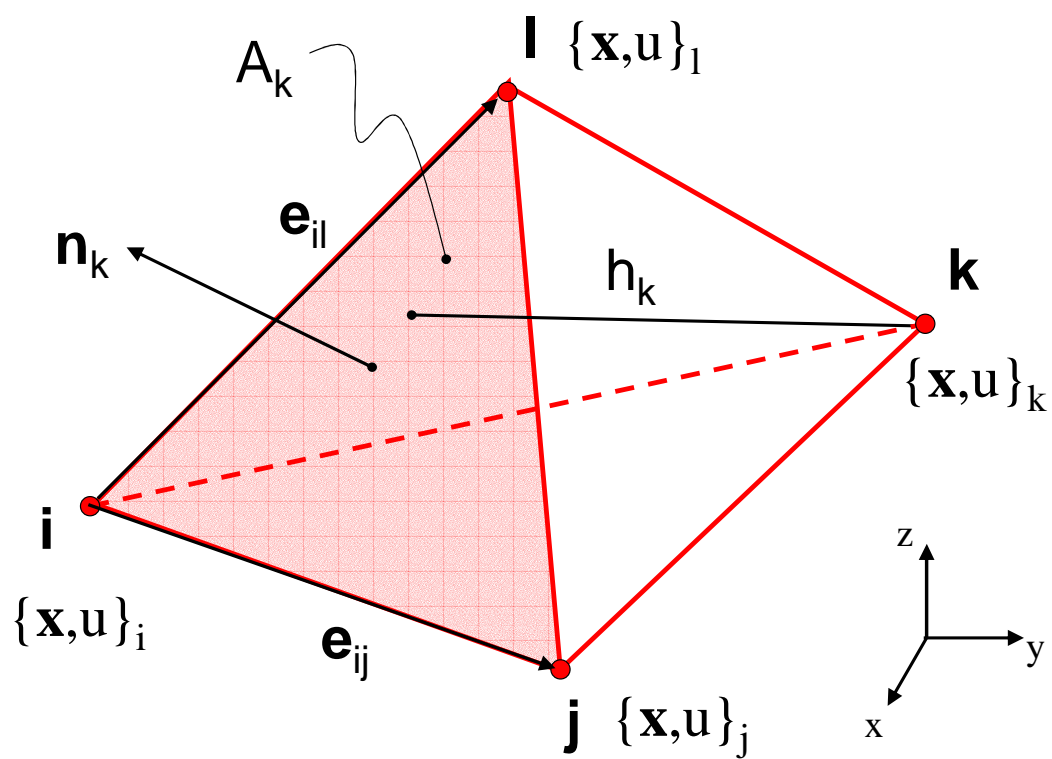
Figure 19: Tetrahedral transducer element

4.3 TRANSDUCER FINITE ELEMENT VECTORS AND MATRICES

The vectors of nodal generalized forces, $\mathbf{f}(\mathbf{x}, \mathbf{u})$ and charges, $\mathbf{q}(\mathbf{x}, \mathbf{u})$, are the assemblies of element vectors, $\mathbf{f}^{(e)}(\mathbf{x}^{(e)}, \mathbf{u}^{(e)})$ and $\mathbf{q}^{(e)}(\mathbf{x}^{(e)}, \mathbf{u}^{(e)})$, where $\mathbf{x}^{(e)}$ and $\mathbf{u}^{(e)}$ are the element vectors of nodal displacements and potentials. The element generalized forces are calculated using the principle of virtual work by differentiating element's coenergy (4.3) with respect to nodal displacements and potentials:

$$\mathbf{f}^{(e)}(\mathbf{x}^{(e)}, \mathbf{u}^{(e)}) = \frac{\partial W^{(e)}(\mathbf{x}^{(e)}, \mathbf{u}^{(e)})}{\partial \mathbf{x}^{(e)}} = \left(\mathbf{u}^{(e)}\right)^T \frac{\partial \mathbf{C}^{(e)}(\mathbf{x})}{\partial \mathbf{x}^{(e)}} \mathbf{u}^{(e)} \tag{4.4}$$

$$\mathbf{q}^{(e)}(\mathbf{x}^{(e)}, \mathbf{u}^{(e)}) = \frac{\partial W^{(e)}(\mathbf{x}^{(e)}, \mathbf{u}^{(e)})}{\partial \mathbf{u}^{(e)}} = \mathbf{C}^{(e)}(\mathbf{x}) \mathbf{u}^{(e)} \tag{4.5}$$

In order to calculate the derivatives of the element capacitance matrix, the derivatives of the element normals (see Figure 19) must be determined. The normals are given by (see Appendix B for details)

$$\mathbf{n}_1 = \frac{\mathbf{e}_{24} \times \mathbf{e}_{23}}{2A_1}, \quad \mathbf{n}_2 = \frac{\mathbf{e}_{13} \times \mathbf{e}_{14}}{2A_2}, \quad \mathbf{n}_3 = \frac{\mathbf{e}_{14} \times \mathbf{e}_{12}}{2A_3}, \quad \mathbf{n}_4 = \frac{\mathbf{e}_{12} \times \mathbf{e}_{13}}{2A_4} \tag{4.6}$$

In (4.6), $\mathbf{e}_{ij}$ is the edge vector with the origin in node i and the end in node j, and A_k is the area of the k-th element side. Recalling the element volume (see Appendix C for details),

$$V = \frac{h_1 A_1}{3} = \frac{h_2 A_2}{3} = \frac{h_3 A_3}{3} = \frac{h_4 A_4}{3} \tag{4.7}$$

The following expression for the element coenergy can be obtained

$$W^{(e)} = \sum_{i=1}^{10} W_i^{(e)} \tag{4.8}$$

where coenergy terms, $W_i^{(e)}$, are given by

$$W_1^{(e)} = \frac{(\mathbf{e}_{24} \times \mathbf{e}_{23}) \cdot (\mathbf{e}_{24} \times \mathbf{e}_{23})}{72V} \epsilon U_1^2, \qquad W_2^{(e)} = \frac{(\mathbf{e}_{13} \times \mathbf{e}_{14}) \cdot (\mathbf{e}_{13} \times \mathbf{e}_{14})}{72V} \epsilon U_2^2, \tag{4.9}$$

$$W_3^{(e)} = \frac{(\mathbf{e}_{14} \times \mathbf{e}_{12}) \cdot (\mathbf{e}_{14} \times \mathbf{e}_{12})}{72V} \epsilon U_3^2, \qquad W_4^{(e)} = \frac{(\mathbf{e}_{12} \times \mathbf{e}_{13}) \cdot (\mathbf{e}_{12} \times \mathbf{e}_{13})}{72V} \epsilon U_4^2, \tag{4.10}$$

$$W_5^{(e)} = \frac{(\mathbf{e}_{24} \times \mathbf{e}_{23}) \cdot (\mathbf{e}_{13} \times \mathbf{e}_{14})}{36V} \epsilon U_1 U_2, \qquad W_6^{(e)} = \frac{(\mathbf{e}_{24} \times \mathbf{e}_{23}) \cdot (\mathbf{e}_{14} \times \mathbf{e}_{12})}{36V} \epsilon U_1 U_3, \quad (4.11)$$

$$W_7^{(e)} = \frac{(\mathbf{e}_{24} \times \mathbf{e}_{23}) \cdot (\mathbf{e}_{12} \times \mathbf{e}_{13})}{36V} \epsilon U_1 U_4, \qquad W_8^{(e)} = \frac{(\mathbf{e}_{13} \times \mathbf{e}_{14}) \cdot (\mathbf{e}_{14} \times \mathbf{e}_{12})}{36V} \epsilon U_2 U_3, \quad (4.12)$$

$$W_9^{(e)} = \frac{(\mathbf{e}_{13} \times \mathbf{e}_{14}) \cdot (\mathbf{e}_{12} \times \mathbf{e}_{13})}{36V} \epsilon U_2 U_4, \qquad W_{10}^{(e)} = \frac{(\mathbf{e}_{14} \times \mathbf{e}_{12}) \cdot (\mathbf{e}_{12} \times \mathbf{e}_{13})}{36V} \epsilon U_3 U_4 \quad (4.13)$$

The vector of element nodal forces can now be presented in the following general form

$$\mathbf{f}^{(e)} = \sum_{k=1}^{10} \frac{\partial W_k^{(e)}}{\partial \mathbf{x}^{(e)}} = \sum_{k=1}^{10} \left[\frac{\partial G_k(\epsilon, \mathbf{e}_{ij}, U_n)}{\partial \mathbf{x}^{(e)}} \frac{1}{V} - \frac{G_k(\epsilon, \mathbf{e}_{ij}, U_n)}{V^2} \frac{\partial V}{\partial \mathbf{x}^{(e)}} \right] \qquad (4.14)$$

In (4.14), x_m is the m-th component of the element displacement vector $(\mathbf{x}^{(e)})$, and G_k are the functions of element edge vectors $(\mathbf{e}_{ij})$, permittivity (ϵ) and nodal potentials (U_n). The element vector of nodal charges is given by

$$\mathbf{q}^{(e)} = \mathbf{C}^{(e)}(\mathbf{x})\mathbf{u}^{(e)} = \sum_{k=1}^{10} \frac{\partial W_k^{(e)}}{\partial \mathbf{u}^{(e)}} \qquad (4.15)$$

The blocks of element tangent stiffness matrix are calculated by differentiating element vectors of nodal reactions and charges with respect to element vectors of nodal displacements and potentials

$$\mathbf{K}_{xx}^{(e)} = \frac{\partial \mathbf{f}^{(e)}}{\partial \mathbf{x}^{(e)}}, \qquad \mathbf{K}_{xu}^{(e)} = \frac{\partial \mathbf{f}^{(e)}}{\partial \mathbf{u}^{(e)}}, \qquad \mathbf{K}_{ux}^{(e)} = \frac{\partial \mathbf{q}^{(e)}}{\partial \mathbf{x}^{(e)}}, \qquad \mathbf{K}_{uu}^{(e)} = \frac{\partial \mathbf{q}^{(e)}}{\partial \mathbf{u}^{(e)}} \qquad (4.16)$$

Note, that all element matrices and vectors are calculated analytically, i.e. avoiding numerical integration and differentiating. In this case, the element is not just computationally effective, but also extremely accurate in computing generalized nodal forces and charges. Knowing the element vectors and matrices, the whole non-linear system of matrices and vectors representing static equilibrium can be assembled and solved with iterative solvers based on Newton - Raphson method.

4.4 MESH MORPHING

An internal mesh morphing capability is an important feature of the developed transducer element that separates it from lumped transducers and models based on a sequential coupling. Mesh morphing is a process of updating vectors of nodal displacements of the transducer elements during the solution of a non-linear problem. The number of elements remains constant so that element continuity is maintained during mesh morphing. In the element, there are out-of-balance mechanical forces acting upon each node. The interface nodes (nodes on the surface of electrodes) generates the electrostatic force that deforms the mechanical structure. Every inner node moves in a direction defined by the resulting out-of-balance force acting upon the node. Structural stiffness of the transducer elements is inversely proportional to the element volume, i.e. the bigger elements are softer than the smaller ones. This is extremely important for modeling geometrical singularities such as sharp corners or edges. The mesh must be refined around the singularities in order to capture strong electrostatic fields and to accurately compute driving forces (see Figure 20). High forces, however, can "invert" transducer elements if their structural stiffnesses are not big enough (see Figure 21). For this reason, the structural stiffness of transducer elements are weighted based on their size.

The convergence speed and solution accuracy of the element during a non-linear solution depends on many parameters, the most important of which are the convergence tolerance (CT) and the morphing acceleration factor (MAF). The first parameter is a convergence criterion used by an iterative Newton - Raphson solver. The second parameter is a factor used to stiffen or soften all of the transducer elements. Increasing the morphing acceleration factor produces a stiffer mesh, which could be necessary for strong singularities or small displacements.
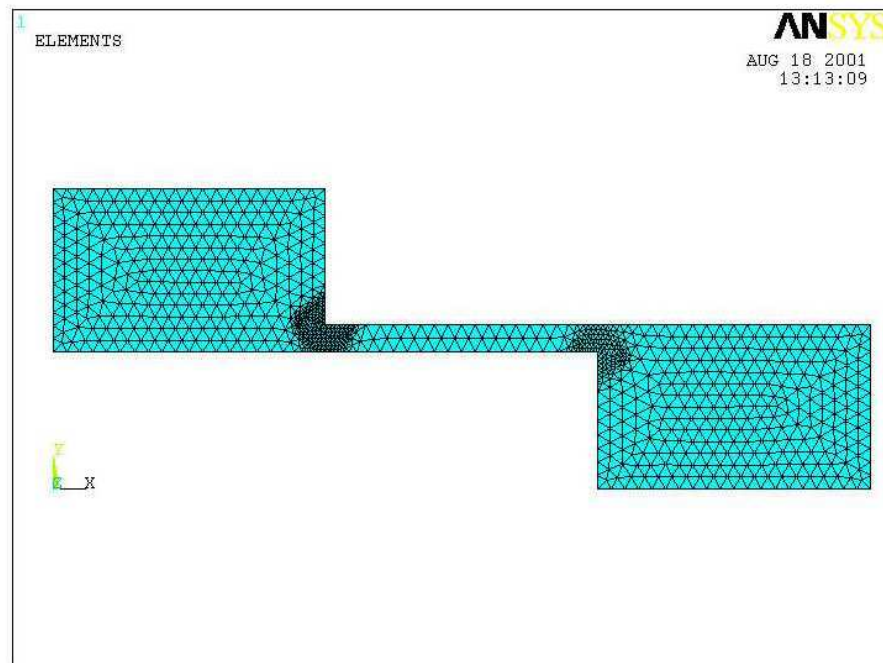
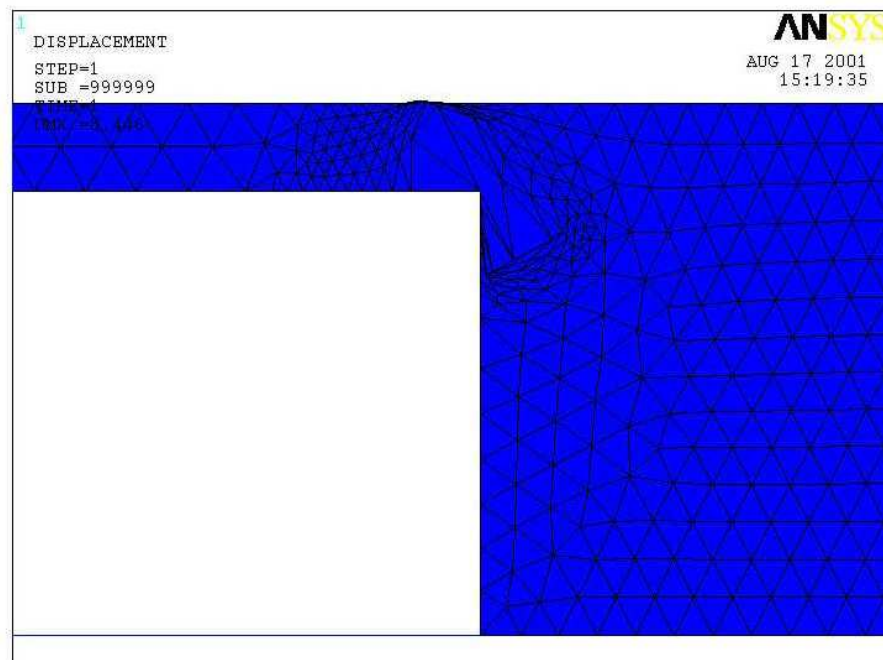Figure 20: Mesh refinement for accurate capturing singularities

Figure 21: Element inversion around singular point

4.5   NUMERICAL EXAMPLES

4.5.1   Parallel-plate electromechanical transducer

As a first example to demonstrate the new element capabilities, we will compute a static equilibrium state of a parallel plate capacitive transducer, which is schematically shown in Figure 6 (see Chapter 3). The transducer consists of two electrodes separated by a gap that is a function of applied voltage and a stiffness of a suspending spring. This problem has an analytical solution for rigid electrodes and a lumped spring without accounting for fringing electrostatic fields. The electrode displacement corresponding to the static equilibrium, u_e can be calculated by solving the following non-linear equation:

$$ku_e - \frac{\epsilon_0 V^2}{2(g_0 - u_e)^2} = 0 \tag{4.17}$$

In (4.17), k is the spring stiffness, ϵ_0 is a free space permittivity, g_0 is the initial gap between the electrodes, and V is the applied voltage. The rectangular electrodes have 1.0 μm side length and are separated by a gap of 1.0 μm. The voltage of 0.5 V is applied to the transducer. The rigid electrodes are modelled by constraining the interface nodes of the transducer elements. The transducer element size is set to 0.5 μm. The FE model consists of one hundred transducer elements and one spring element (184 total degrees of freedom). The spring stiffness is 0.9765625 N/μm. In this case, the solution of equation (4.17) predicts an equilibrium displacement of 0.2 μm.

The problem posed was then modelled using the new transducer element. A sample predicted displacement of the 3-D transducer mesh is depicted in Figure 22. In Table 3, the solution accuracy and speed are compared for different values of convergence tolerance (morphing acceleration factor is equal to one – no acceleration). At a smaller value of the tolerance, more iterations are required to converge, but the solution becomes more accurate. This is an intuitively simple, but very important result. In Table 4, the solution accuracy and speed are compared for different values of morphing acceleration factor (convergence tolerance is equal to 0.00005 N). A smaller factor (softer mesh) leads to a faster convergence, while a larger factor leads to a slower convergence. Note, that the accuracy essentially

Table 3: Solution convergence speed and accuracy for various convergence tolerance (CT) values

CT (N)	Time (s)	Iterations	Displacement	Error (%)
0.02000	2.84	7	0.16989	15.06
0.01000	3.19	9	0.18233	8.84
0.00500	3.71	12	0.19184	4.08
0.00200	4.28	15	0.19617	1.92
0.00100	4.79	18	0.19819	0.91
0.00050	5.34	21	0.19914	0.43
0.00025	5.99	24	0.19959	0.21
0.00005	6.97	30	0.19991	0.05

remains independent of the acceleration factor. To achieve more accurate solution, one must therefore adjust the value of the convergence tolerance. The MAF can be further used to speed up the convergence for a given accuracy. It should be noted that there is a bottom MAF limit which can not be crossed without loosing the integrity of the transducer elements (mesh becomes too soft). This limit varies for different problems and boundary conditions. An "inversion" of transducer elements is used as an indicator that this limit has been reached.

4.5.2   Electrostatic torsion microactuator

The second example problem that will be used to verify the transducer element is an electrostatic torsion microactuator. The physical torsion microactuator [31] used for the following example was fabricated using three photolithography steps made on a Si(001) substrate composed of a 85-μm bulk, silicon 1-μm heavily boron-doped layer, and a 15-μm epitaxial layer. Fabrication of the actuator was done in three steps [31]. The first step defines the conducting elements (lines and plates), the second step defines the proof mass, and the third step defines the springs. The epitaxial layer is etched out through reactive ion etching (RIE).

Table 4: Solution convergence speed and accuracy for various morphing acceleration factor (MAF) values

MAF	Time (s)	Iterations	Displacement	Error (%)
0.20	4.35	15	0.19990	0.05
0.25	4.51	16	0.19991	0.05
0.50	5.35	21	0.19992	0.05
1.00	6.97	30	0.19991	0.05
2.00	10.43	48	0.19990	0.05
4.00	17.16	85	0.19990	0.05

The electrodes controlling the angle were attached using indium bumps technology [31]. The summary of the torsion microactuator parameters is presented in Table 5.

The finite element model of the microactuator is depicted in Figure 23. Solid ANSYS elements (green) were used to model the micromirror and support beams. The 3-D transducer elements (purple) were used to model air zones between the two driving electrodes. FE model contains 5,207 transducer elements and 2,096 solid elements. Alternating current between the electrodes allows the micromirror to turn around the supporting beam axis. Increasing voltage leads to pull-in of the micromirror. The reported [31] theoretical and experimental values of pull-in voltage, V_{pin}, and pull-in angle, θ_{pin}, are presented in Table 6. The results obtained using the 3-D transducer model (Figure 23) are compared to the reported results (Table 6). The FE results show very good agreement with the experimental data.

4.5.3 Combdrive electromechanical transducer

The final example problem to be solved with the new element is for a combdrive electromechanical transducer. The lateral combdrive transducer (see Figure 24) was originally introduced in 1989 by Tang [15]. Since its introduction, little or no improvements have been made to allow a designer to calculate the capacitance and driving force of a combdrive. The original formula for a capacitance and a driving force are based on a simplified mathematical
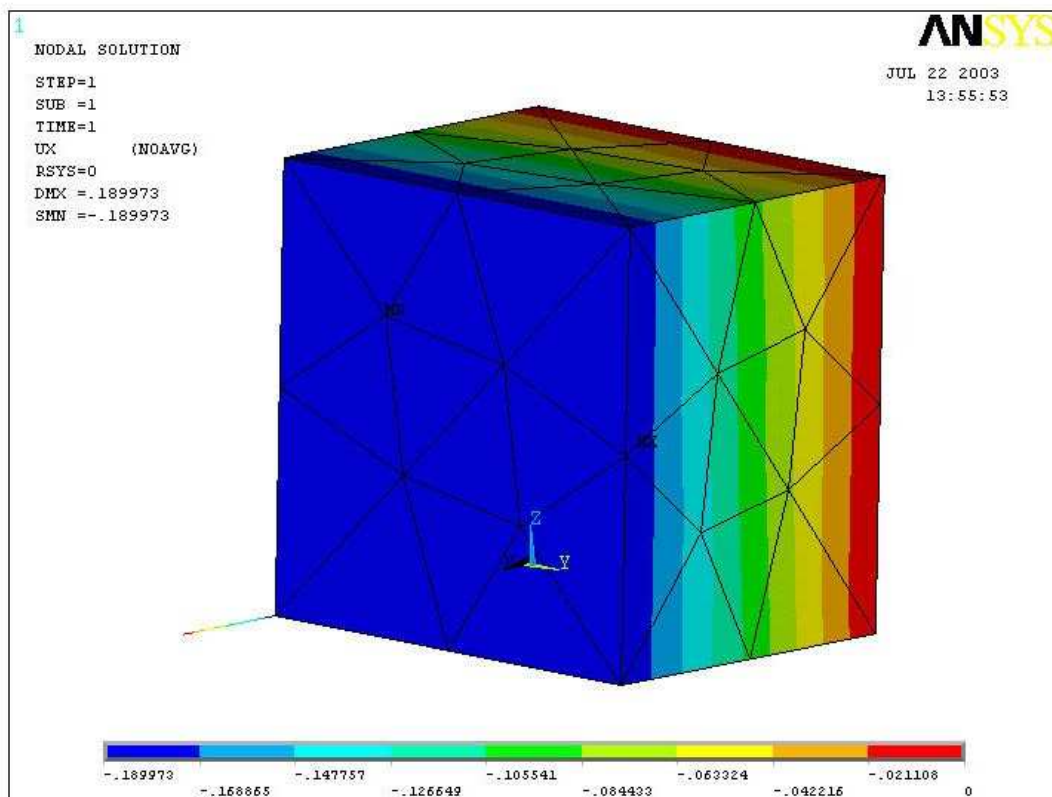
Figure 22: Displacement field (deformed transducer mesh)

Table 5: Summary of the torsion microactuator parameters

Shear modulus	G	73 GPa
Distance from axis of rotation to nearest electrode edge	a_1	430 μm
Distance from axis of rotation to farthest electrode edge	a_2	680 μm
Plate half width	a_3	700 μm
Initial gap between electrodes and substrate	d	4.55 μm
Width of supportive beams	w	31 μm
Thickness of supportive beams	t	14 μm
Length of supportive beams	L	400 μm
Length of micromirror plate and both electrodes	b	1300 μm

Table 6: Comparison between reported (theoretical and experimental) and FE pull-in parameters for torsion microactuator

	Theoretical	Experimental	FEA (3-D)
θ_{pin}	0.4042	0.385	0.397
V_{pin}	11.59 V	11.5 V	11.55 V
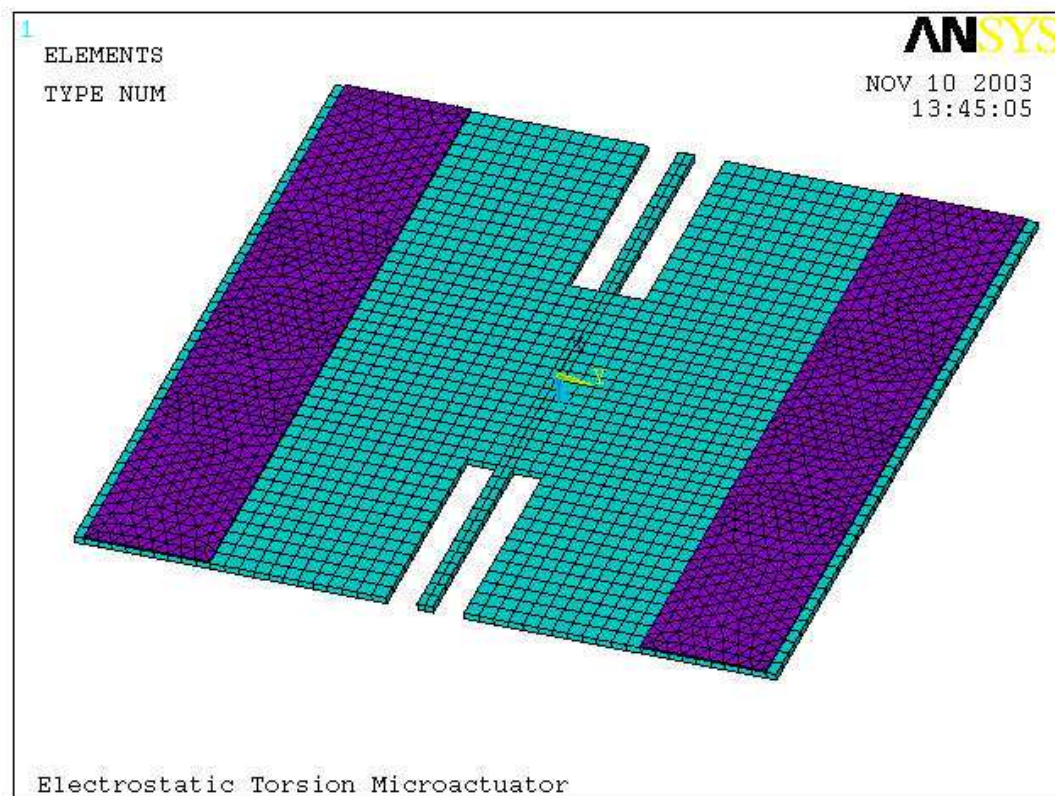
Figure 23: Electrostatic torsion microactuator (FE model)

model which accounts for only an electrostatic field between the lateral surfaces of the comb-drive fingers. It was assumed that the field lines are straight. The combdrive's capacitance and driving force have the following expressions:

$$C(u) = \frac{2Nt(L_0 + u)\epsilon_0}{g}, \qquad F(u) = \frac{V^2}{2}\frac{dC(u)}{du} = \frac{Nt\epsilon_0 V^2}{g} \qquad (4.18)$$

In (4.18), N is the number of comb fingers, L_0 is the initial comb finger overlap, t is the electrode thickness, g is the gap between the comb fingers, u is the stroke, ϵ_0 is the permittivity, and V is the applied voltage. Equation (4.18) ignores the field between the top/bottom and the top/lateral fields, as well as the fringing electrostatic fields that develop in the corners and edges of the comb fingers. To illustrate this point, consider the 2-D electrostatic FE model of the combdrive, representing a cross-section of the 3-D combdrive (see Figure 25). A voltage is applied between the rotor and stator that produces an electrostatic field with the potential distribution depicted in Figure 25. This 2-D model accounts for fringing fields, which are shown in Figure 26. The gap between the fingers is 4 μm, finger width is 4 μm, finger thickness is 2 μm, and the size of the air region is 4 μm. Using a unit thickness in a z-direction we are able to compute the capacitance, which is 25.994 pF. The theoretical capacitance value, calculated using (4.18), is 8.854 pF, which is almost four times smaller than the computed value.

Combdrive transducers are widely used in the circuit models of complicated sensors and actuators. In order to determine a realistic value of the capacitance as a parameter of such a network element, a 3-D models is required to accurately extract the capacitance and calculate the driving force. The 3-D electrostatic FE combdrive model can be used to extract the combdrive capacitance as a function of stroke (rotor displacement), which is an important parameter of a combdrive lumped (network) element. To illustrate the modeling capabilities of the element consider a combdrive with a finger length of 50 μm, an overlap of 25 μm, a gap between fingers of 4 μm, a finger width of 4 μm, a finger thickness of 2 μm, an air region size of 2 μm, and a spring stiffness of 10 N/μm. Utilizing the numerical (FE) electrostatic model, the capacitance is found to be a linear function of stroke (see Table 7). Using the data in Table 7, we can calculate a first-order derivative of capacitance with respect

Table 7: Combdrive capacitance as a function of stroke

Stroke	Capacitance
0.0	6.9096E-10
1.0	7.1264E-10
2.0	7.3498E-10
4.0	7.7896E-10
6.0	8.2285E-10
8.0	8.6686E-10
10.0	9.1082E-10

to the stroke (coefficient of linearity). The electrostatic force in this case is independent of stroke and remains constant for a given value of applied voltage. For $\epsilon_0 = 1$ we have

$$F_e(V) = \frac{V^2}{2}\frac{dC(u)}{du} \approx 1.24V^2 \tag{4.19}$$

$$U_t(V) = \frac{F_e(V)}{k} = \frac{1.24V^2}{10} = 0.124V^2 \tag{4.20}$$

Displacement values for various voltages are presented in Table 8.

As a final modeling exercise, we will use the tetrahedral transducer element to compute the static equilibrium states of the combdrive for various values of the applied voltage. A sample with its displacement field is shown in Figure 27. FE model contains 12,740 transducer elements. In the figure, it is important to note that the air region is now modelled with the transducer elements. Boundary conditions play an important role in the modeling and solution. The external nodes of the transducer mesh are free to move, while the boundary is fixed in certain directions. The outside boundary (far-field) is fixed with respect to all mechanical degrees of freedom. The interface nodes (nodes attached to the electrodes) are allowed to slide along the electrodes as long as the electrode shape does not change. This assumption is only possible for rigid mechanical structures. The potential distribution for a given voltage is shown in Figures 28 and 29. In Figure 29, the air around the fingers (top and

Table 8: Equilibrium displacement as a function of applied voltage

Voltage (V)	U_t (Tang [15])	U_{3-D} (3-D transducer)	U_u (Uncoupled)
1.0	0.05	0.57	0.124
2.0	0.20	1.01	0.496
3.0	0.45	1.78	1.116
4.0	0.80	2.74	1.984
5.0	1.25	3.96	3.100
6.0	1.80	5.26	4.464
10.0	5.00	12.9	12.40

bottom) is not depicted. The values of equilibrium displacements (for $\epsilon_0 = 1$ and $N = 1$) are shown in Table 8 for different voltages and compared to the traditional approach [15] given by:

$$U_e = \frac{Nt\epsilon_0 V^2}{g_0 k} \tag{4.21}$$

The difference in theoretical and FE results presented in Table 8 is due to the fringing fields that are modelled in both 3-D transducer element and uncoupled FE models but are ignored in a simplified analytical model [15]. This example demonstrates importance and contribution of the 3-D transducer element developed in this Chapter.

The differences between the 3-D transducer and uncoupled FE results in Table 8 are due to the fact that the force convergence tolerance were the same for all voltages. More accurate results were obtained for higher voltages (see Table 8) for the prescribed convergence tolerance value (order of 1.0 N). Figure 30 demonstrates that the difference in transducer and uncoupled solutions can be decreased by decreasing the value of the convergence tolerance (for the applied voltage of 4.0 V). A slight mismatch (due to morphing) between FE meshes of the transducer and the uncoupled models also contributes to the difference between these two solutions.

4.6 SUMMARY

A distributed 3-D transducer element formulation was developed in this chapter for modeling a wide range of MEMS devices. The elements accounts for fringing electrostatic fields and the internal morphing capability of the element allows a designer to use the original mesh for solving large displacement non-linear problems. The computer code was developed for the ANSYS platform and several numerical examples were presented which show good agreement with experimental data. The developed element is among the most sophisticated and effective techniques of solving 3-D coupled field problems presently available for designers and researchers working in the MEMS industry.
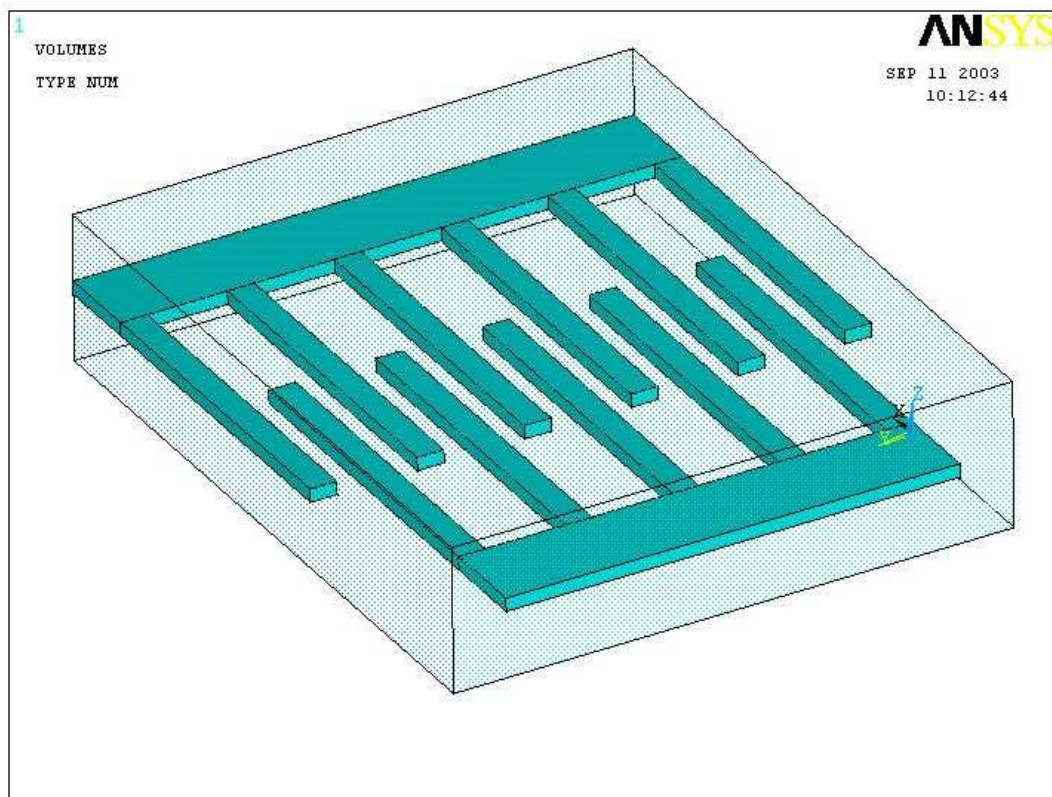
Figure 24: Combdrive transducer (ANSYS solid model)
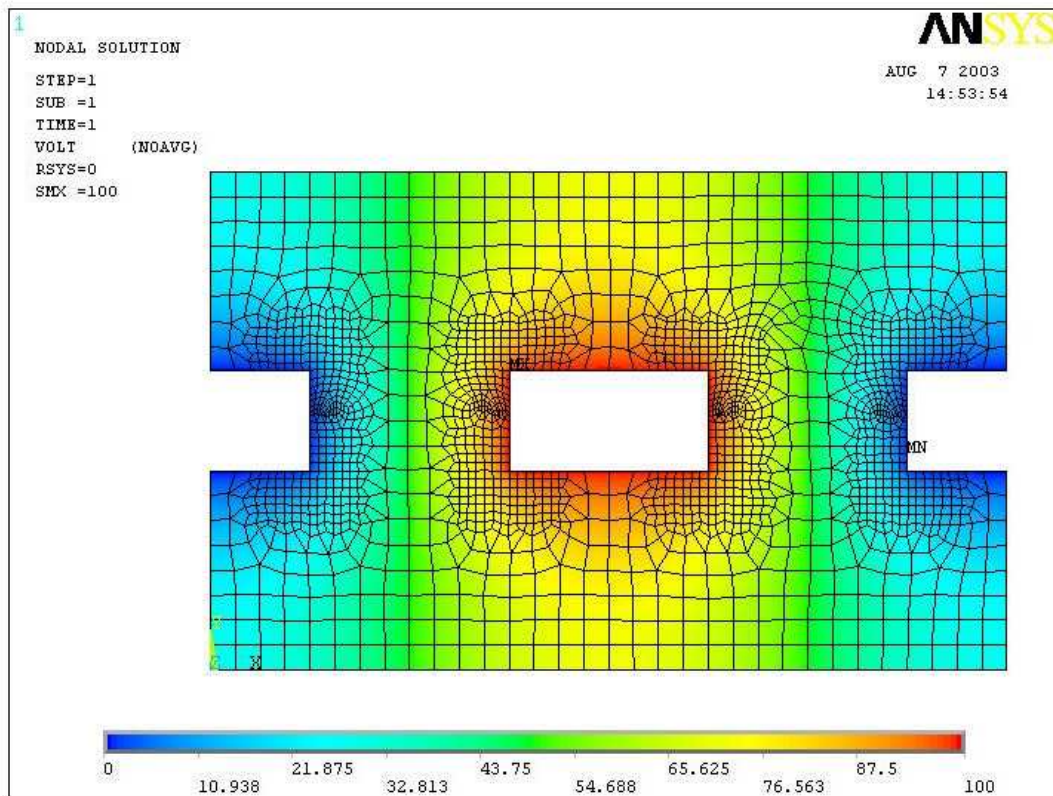
Figure 25: Potential distribution between two fixed and one moving comb finger (2-D model of the cross-section)

Figure 26: Electrostatic field between two fixed and one moving comb finger (2-D model of the cross-section)

Figure 27: Displacement field (combdrive layer shown)

Figure 28: Potential distribution (full combdrive transducer model shown)

Figure 29: Potential distribution (combdrive layer shown)

Figure 30: Difference between transducer and uncoupled FE solutions ($\Delta = \frac{U_{3-D} - U_u}{U_u} \cdot 100\%$)

5.0 MODELING IN-PLANE MISALIGNMENTS IN LATERAL COMBDRIVE TRANSDUCERS

5.1 INTRODUCTION

5.1.1 Overview of combdrive transducers

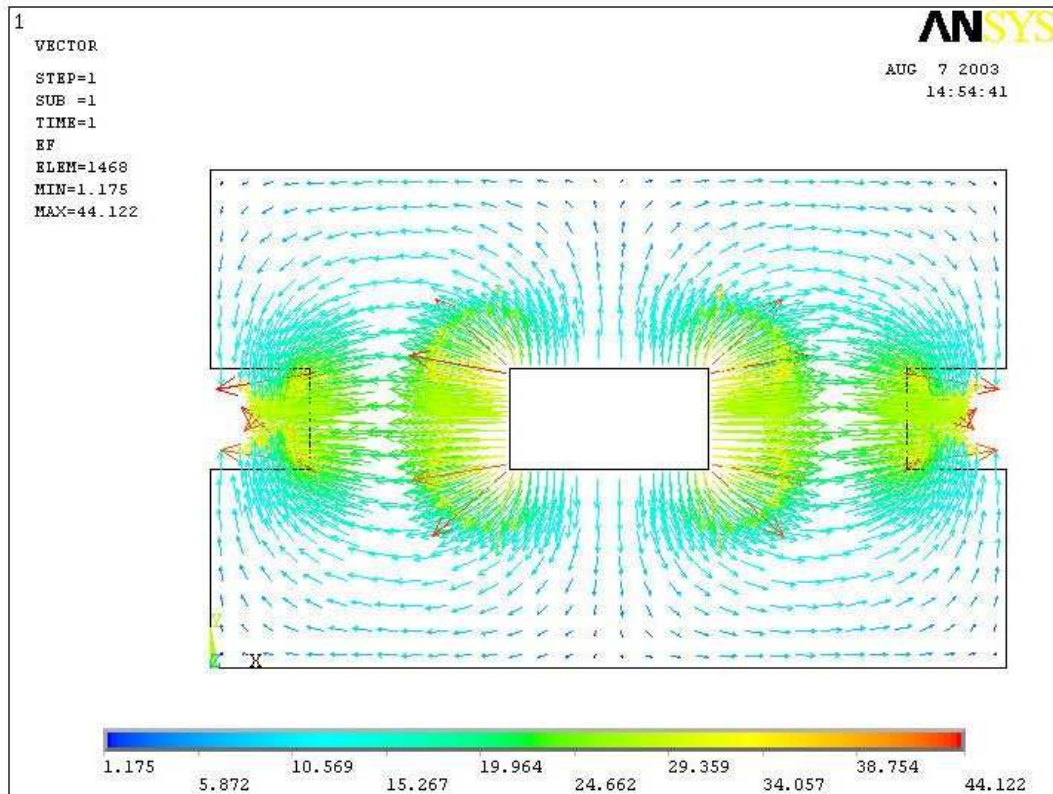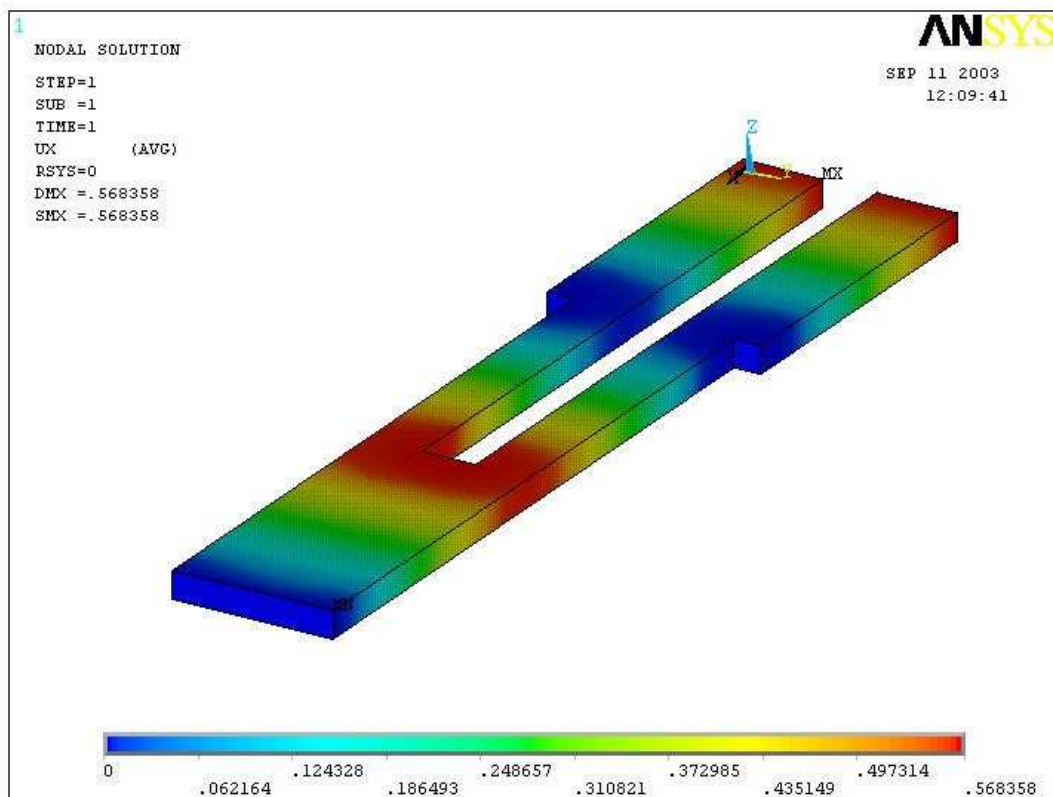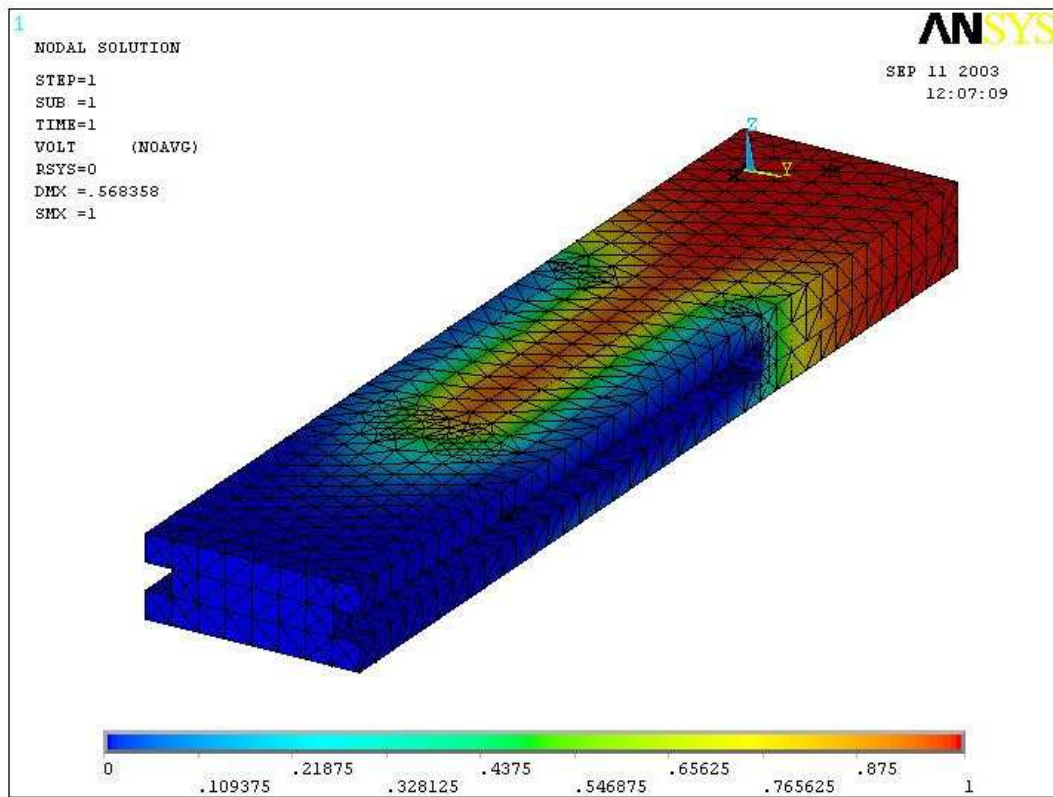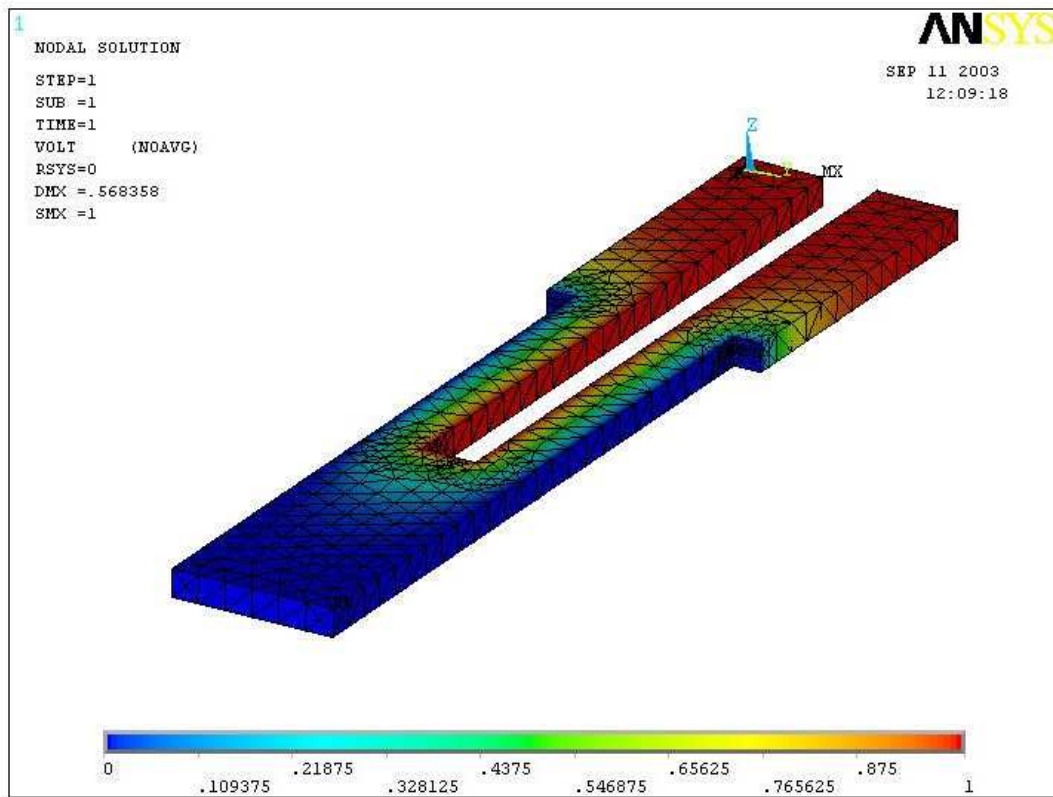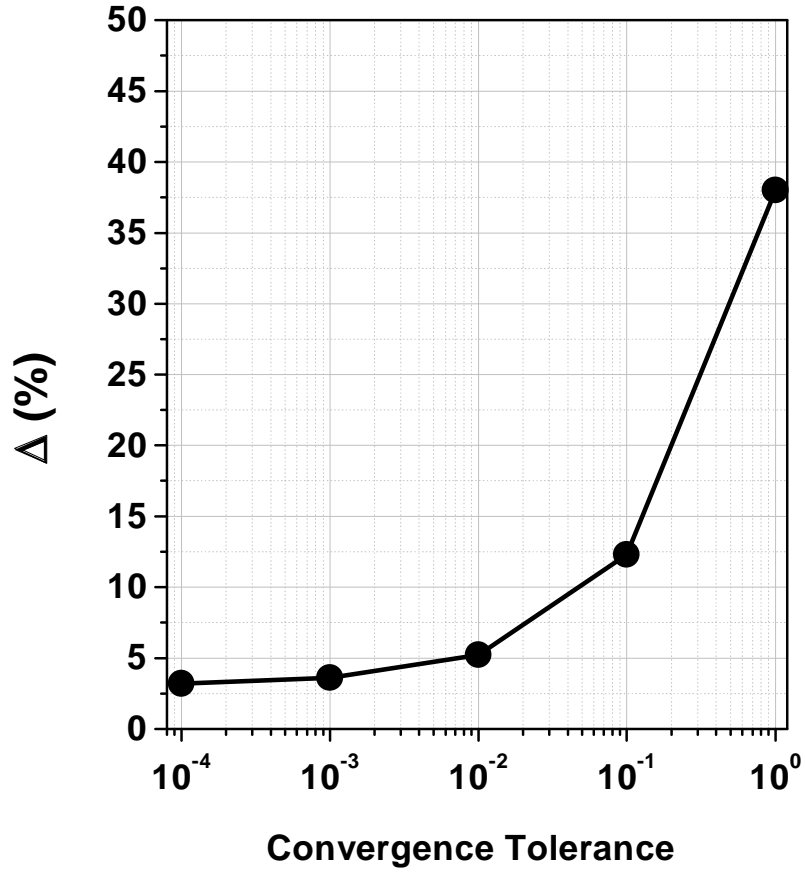Interdigitated finger (comb) transducers or "combdrives" have been successfully used in a wide variety of sensors and actuators for more than a decade [15], [53]. Commercially produced combdrives can be fabricated into numerous finger shapes including straight, circular and conical (see Figure 31). This chapter is particularly focused on the misalignments of surface micromachined straight finger combdrives [43]. Straight finger combdrives (see Figure 32) are critical for the operation of RF microdevices, mechanical sensors, long-range actuators and mechanical power transmitters [3]. Slight misalignment between a rotor (a moving comb) and a stator (an anchored comb) can significantly degrade device performance. Misalignments of the combdrives can be attributed to one or more of the following causes: fabrication defects, asymmetric mechanical or potential distributions, non-uniform electric properties of the silicon, and failure of electrical circuitry. One of the most important parameters in the design of MEMS devices is the pull-in voltage, which can be determined by conducting a stability analysis of the static equilibrium [54], [55]. The pull-in effect must be avoided because it causes stiction between the rotor and the stator. Stiction can lead to an electrical shortage and ultimately device failure [3]. Thus, analyzing the pull-in effect as related to combdrive misalignments is critically important, and therefore will be one of the primary focuses of the present Chapter.

5.1.2 Misalignment classification

There are two general types of combdrive misalignments: (1) out-of-plane and (2) in-plane. Curling of the comb fingers is the most common example of an out-of-plane misalignment. Curling is usually caused by residual stresses and often develops in surface micromachined combdrives [3]. The value of a combdrive's capacitance and its driving electrostatic force can be significantly reduced by curling. The curling effect, however, can be avoided by reducing the aspect ratio (length/thickness) of the comb fingers. Other out-of-plane misalignments in combdrives, such as asymmetry and non-parallel etching of combdrive fingers, have been investigated in detail [56], [22]. These studies have shown that misalignments can generate large torsional motions [56], which can be used in micromirror applications, and can significantly change the driving force [22].

Little information is currently available, however, on in-plane misalignments. The in-plane misalignments not only decrease precision (by changing the value of the driving force), but they can lead to structural instabilities and eventually device failure (the electrical shortage). The stroke range of a misaligned combdrive becomes different from its original design. For the purpose of better understanding in-plane misalignments, translational and rotational static combdrive modes will be studied in this chapter. Both analytical and numerical methods will be utilized to calculate the in-plane forces and the moments produced by quasi-static electrostatic fields in the combdrive.

5.1.3 Numerical approach

The finite element method (FEM) can be used as a basic tool for coupled field numerical simulations [16]. The most common method of analyzing MEMS devices is to solve the structural and electrostatic problems separately. This technique, often referred to as decoupling, can be applied accurately for simple geometries, such as parallel plate capacitors or perfectly aligned combdrives. Modeling combdrive misalignment effects in MEMS devices, however, requires more sophisticated numerical techniques. Fringing fields associated with the edges and corners of the combdrive fingers, for example, significantly contribute to the field energy and driving forces. Therefore, 2-D or 3-D distributed coupled-field finite elements are

required to accurately capture the fringing field effects [25]. The multiple degrees of freedom lumped coupled-field models are less accurate in this case. Generally, stability analysis of the actuator equilibrium states (pull-in analysis) can be performed using either analytical or numerical techniques [57], [58]. Closed-form analytical models and equilibrium solutions are preferable if they can be constructed. However, such an approach is limited to a few simple geometrical configurations. In this chapter, it will be shown that a closed-form solution can be obtained for the pull-in voltage of only translationally misaligned combdrives. In this chapter we will use a 2-D FE coupled-field approach that utilizes strongly coupled triangle transducer elements [25]. Using this approach, several misalignment models will be analyzed and the pull-in voltage will be determined as a function of several misalignment parameters.

5.2   ANALYTICAL MODELS OF COMBDRIVES WITH IN-PLANE MISALIGNMENTS

5.2.1   Basic assumptions and approach

In this section, two analytical models for the in-plane misaligned combdrive are discussed: (1) translational and (2) rotational. To simplify the geometry, only one pair of comb fingers will be analyzed. It will be assumed that the rotor and stator are two equipotential electrodes with a potential difference V, applied between them. The out of plane component (z-component) of the electrostatic field will be ignored. The total electrostatic energy of the comb, W_e, can be calculated using the following relationship:

$$W_e = \frac{C_{comb}V^2}{2} = \frac{Q^2}{2C_{comb}} \tag{5.1}$$

In (5.1), C_{comb} is the total capacitance of the combdrive, and Q is the electric charge. As illustrated in Figure 33, the total capacitance is a function of the tip capacitance, C_{tip}, the lateral capacitances, C_{top} and C_{bot}, and the fringing capacitance, C_{fring}:

$$C_{comb} = C_{tip} + C_{top} + C_{bot} + C_{fring} \tag{5.2}$$

The electrostatic energy stored in the tip, lateral and fringing electrostatic fields is proportional to the respective terms in (5.2). In both the translational and rotational models discussed in this section, it will be assumed from the comb geometry that $C_{tip} << C_{top}, C_{bot}$. This is due to the fact that finger overlap is usually much smaller than finger length. The fringing electrostatic fields will also be ignored. In addition, it is assumed that the derivatives of capacitances with respect to the comb displacements are negligible. Such an assumption is important since electrostatic forces are directly proportional to these derivatives. In order to justify these assumptions, the influence of the fringing fields will be determined using the finite element method and then compared to the analytical results. The mechanical domain of the combdrive can be represented by the system of linear springs shown in Figure 33. The mechanical potential energy is given by

$$W_m = \frac{k_x x^2}{2} + \frac{k_y y^2}{2} + \frac{k_\theta \theta^2}{2} \tag{5.3}$$

In (5.3), x is the stroke, y is the translational misalignment, θ is the rotational misalignment, and k_x, k_y, and k_θ are the stiffnesses of the springs. The combdrive structure is assumed to be rigid, since the structural stiffness is usually much higher than the spring stiffnesses. The total potential energy of the combdrive transducer is a combination of the electrostatic and the mechanical energies:

$$W = W_e + W_m = \frac{Q^2}{2(C_{top} + C_{bot})} + \frac{k_x x^2}{2} + \frac{k_y y^2}{2} + \frac{k_\theta \theta^2}{2} \tag{5.4}$$

For a given value of the potential drop, V, or charge Q the energy of the electrostatic field is a function of three generalized rigid body motion coordinates: x, y and θ. According to the principle of virtual work, the generalized forces associated with these coordinates can be calculated by [50]:

$$M_z(x, y, \theta) = -\frac{\partial W}{\partial \theta}, \qquad F_x(x, y, \theta) = -\frac{\partial W}{\partial x}, \qquad F_y(x, y, \theta) = -\frac{\partial W}{\partial y} \tag{5.5}$$

Physically, these generalized forces represents the total in-plane moment and two planar components of the total force. They characterize the equilibrium between the attractive electrostatic forces and the restoring mechanical forces produced by the springs. The combdrive is in the state of a static electromechanical equilibrium when all generalized forces

64

(5.5) are equal to zero. The stability of an equilibrium state can be determined using the potential energy function (5.4). If the equilibrium state corresponds to a local minimum of W, then the equilibrium is stable; otherwise the equilibrium state will be unstable. In the following sections two analytical models of the misaligned combdrive will be discussed.

5.2.2 Translational misalignment model

Consider the misaligned case when the comb fingers remain parallel to each other such that there are no rotational misalignments. The total potential energy of the combdrive, W, is a function of the misalignment parameter, y:

$$W(y) = -\frac{\epsilon w L V^2}{2} \left[\frac{1}{g-y} + \frac{1}{g+y} \right] + \frac{k_y y^2}{2} \tag{5.6}$$

In (5.6), L is the finger overlap, ϵ is the permittivity constant, and w is the thickness of the combdrive in the direction of the substrate. The generalized misalignment force can be calculated using (5.5):

$$F(y) = -\frac{dW(y)}{dy} = \frac{\epsilon w L V^2}{2} \left[\frac{1}{(g-y)^2} - \frac{1}{(g+y)^2} \right] - k_y y \tag{5.7}$$

The static equilibrium condition, $F(y) = 0$, is satisfied when:

$$\frac{2yg}{(g-y)^2(g+y)^2} = \frac{k_y y}{\epsilon w L V^2} \tag{5.8}$$

The equation (5.8) has three solutions (equilibrium states):

$$y_0 = 0, \quad y_{1,2} = \pm\sqrt{g^2 - V\sqrt{\frac{2\epsilon g w L}{k_y}}} \tag{5.9}$$

It is clear that for states $y_{1,2}$ to exist the following condition must be satisfied:

$$g^2 - V\sqrt{\frac{2\epsilon g w L}{k_y}} \geq 0 \quad \Rightarrow \quad V \leq \sqrt{\frac{g^3 k_y}{2\epsilon w L}} \equiv V_{PI} \tag{5.10}$$

If the applied voltage is equal to V_{PI} then there is only one equilibrium state:

$$y_0 = y_1 = y_2 = 0 \tag{5.11}$$

The critical voltage, V_{PI}, is often referred as the "pull-in voltage" [59]. Looking at the stability of the obtained equilibrium states, the second derivative of the potential energy, $W(y)$, is given by:

$$\frac{d^2W}{dy^2} = -\epsilon wLV^2 \left[\frac{1}{(g-y)^3} + \frac{1}{(g+y)^3} \right] + k_y \tag{5.12}$$

For the first equilibrium state, $y = y_0$, we have:

$$\frac{d^2W}{dy^2}\bigg|_{(y=y_0)} = -\frac{2\epsilon wLV^2}{g^3} + k_y \tag{5.13}$$

From equation (5.13), it can be found that the second derivative of the total potential energy is positive if $V < V_{PI}$, negative if $V > V_{PI}$ and equal to zero if $V = V_{PI}$. Only in the case of $V < V_{PI}$ does the equilibrium state $y = 0$ remain stable (local minimum of the total potential energy in Figure 34). When the voltage reaches or exceeds the pull-in value, the equilibrium becomes unstable and any small perturbation of y leads to the fingers snapping (pull-in).

It can be shown that for the second and the third equilibrium states (y_1 and y_2), the second derivative of the potential energy is always negative, which indicates local maximums of potential energy. This shows that the other two equilibrium states are unconditionally unstable. The electrostatic force is higher than the restoring mechanical force if y exceeds y_1 (see Figure 35), pulling the rotor towards the stator. The unstable equilibrium y_1 represents the maximum allowable misalignment before the pull-in. The value of y_1 depends on the stiffness, k_y, and therefore can be controlled, as depicted in Figure 36.

5.2.3 Rotational misalignment model

In the rotational misalignment model, there are two misalignment parameters: small rotational misalignment and translational misalignment. The tilted electrode model will be used to calculate the lateral capacitance of the combdrive. In this approach, the tilted electrodes (each lateral side of the comb finger) will be approximated with a set of infinitesimally small plates parallel to the stator plate capacitors. It will also be assumed that the electrostatic

field lines between lateral sides of the rotor and stator are parallel to each other and orthogonal to the stator, so that fringing fields will be neglected. Thus, the tilted capacitance is calculated as an integral over the length of the finger overlap:

$$C(\theta) = \int_0^L \frac{\epsilon w \, ds}{g(\theta, s)} \tag{5.14}$$

In (5.14) L is the length of the overlap, ϵ is the permittivity constant, w is the thickness of the comb finger (thickness of a silicon layer) and θ is the misalignment angle. The gap between the parallel plates of an infinitesimal capacitor with coordinate along the length of the ground electrode (s) is given by:

$$g(\theta, s) = g_0 + [s - \frac{L}{2}] \sin \theta \tag{5.15}$$

where g_0 is the average gap between the combdrive fingers. Substituting (5.15) into (5.14) and integrating over the length we obtain the following expression for the tilted capacitance:

$$C(\theta) = \int_0^L \frac{\epsilon w \, ds}{g_0 + [s - \frac{L}{2}] \sin \theta} = \frac{\epsilon w}{\sin \theta} \ln \left(\frac{2g_0 + L \sin \theta}{2g_0 - L \sin \theta} \right) \tag{5.16}$$

For small rotational misalignments ($\sin \theta \approx \theta$) the tilted capacitance can be approximated by:

$$C(\theta) \approx \frac{\epsilon w}{\theta} \ln \left(\frac{2g_0 + L\theta}{2g_0 - L\theta} \right) \tag{5.17}$$

Equation (5.17) is extremely useful and popular among the designers of analog MEMS devices. It is important to note that an identical mathematical result was obtained using a circular arc approximation of the electrostatic field lines in [22].

To calculate the combdrive capacitance, the average gap, g_0, is substituted with ($g_0 - y - L\theta/2$) and ($g_0 + y + L\theta/2$) for the top and bottom lateral finger surfaces respectively. In this case, we obtain the total capacitance as a function of misalignment coordinates:

$$C(y, \theta) = \frac{\epsilon w}{\theta} \ln \left[\frac{(g_0 - y)(g_0 + y + L\theta)}{(g_0 + y)(g_0 - y - L\theta)} \right] \tag{5.18}$$

Therefore, the total potential energy of the combdrive is:

$$W(y, \theta) = -\frac{\epsilon w V^2}{\theta} \ln \left[\frac{(g_0 - y)(g_0 + y + L\theta)}{(g_0 + y)(g_0 - y - L\theta)} \right] + \frac{k_y y^2}{2} + \frac{k_\theta \theta^2}{2} \tag{5.19}$$

67

The moment and force equilibrium conditions are:

$$\frac{\epsilon g_0 w V^2}{\theta}\left[\frac{1}{g_0^2-(y+L\theta)^2}-\frac{1}{g_0^2-y^2}\right]-k_y y=0 \qquad (5.20)$$

$$\frac{\epsilon w V^2}{2\theta^2}\left(-\ln\left[\frac{(g_0+y+L\theta)(g_0-y)}{(g_0-y-L\theta)(g_0+y)}\right]+\frac{2Lg_0\theta}{g_0^2-(y+L\theta)^2}\right)-k_\theta\theta=0 \qquad (5.21)$$

The obtained non-linear equilibrium equations (5.20) and (5.21) can only be solved numerically. Therefore, the total potential energy function (5.19) has to be evaluated to investigate the stability of the numerical solution. It is important to note that similar pull-in analysis was performed in [55] to model various beam actuators. These two dimensional pull-in equations were solved using MATLAB and compared to FEM/BEM simulations provided by the MEMCAD [55]. However, for actuators with complex geometries and dominant fringing fields, the strongly coupled-field FE modeling can be a more effective method of solving static equilibrium and pull-in problems [25].

5.3   UNCOUPLED FE MODELS

In this section, uncoupled finite element (FE) models of the combdrive are used to account for fringing electrostatic fields. The primary goal of the FE models are to accurately compute the potential energy of the electrostatic domain for a given potential difference between the equipotential electrodes of the combdrive. The accuracy of the FE solution primarily depends upon the characteristics of the FE mesh. The FE electrostatic models (see Figures 4 and 5) have been created using ANSYS/Multiphysics software [40]. As with the analytical model, the generalized FE forces are calculated using virtual work [25]. Since the fingers were assumed equipotential and rigid, only the electrostatic domain has been modelled. It is important to note, however, that mechanical finite elements were still required to: 1) preserve the combdrive shape during motion and subsequent mesh morphing of the electrostatic domain and 2) model the lumped springs that were attached to the combdrives. The air gap between the fingers was meshed using tetrahedral (3-D) and triangular (2-D) electrostatic elements with one degree of freedom per node (potential). The Laplace's potential

Table 9: Combdrive parameters for the uncoupled FE modeling

Model 1	Model 2
Initial gap: 5 μm	Initial gap: 3 μm
Finger length: 100 μm	Finger length: 80 μm
Finger overlap: 50 μm	Finger overlap: 40 μm
Finger width: 5 μm	Finger width: 4 μm
Finger thickness: 2 μm	Finger thickness: 2 μm
Applied voltage: 36 V	Applied voltage 4 V

equation was numerically solved using these elements while the combdrive was kinematically constrained. The field energy was then calculated by integrating over all finite elements [40].

Two sets of the combdrive finger parameters were used for the simulation (Table 9). Using the uncoupled FE models, the capacitance was determined as a function of rotation angle. Examining the 2-D numerical and analytical force results, it was found that the driving force (F_x) of the misaligned combdrive was significantly higher than the perfectly aligned combdrive for both the rotational (see Figure 39) and translational misalignments (see Figure 40). In fact, Figure 39 shows that as the combdrive angle increases, the driving force nonlinearly increases with stroke. This can be particularly problematic for MEMS devices that are designed to have a constant force with increasing stroke. Since both the analytical and 2-D FE models produce similar results, it is evident that in-plane fringing effects are not significant for the driving force. Examining Figure 41, the misalignment forces, F_y, were found to be much larger than the driving forces. The large magnitude of the misalignment forces can significantly affect combdrive performance. Moreover, the moment (M_z) developed in the combdrive (Figure 42) can lead to serious stability problems. The 3-D finite element results in Figures 9 and 10 indicate that the fringing 3-D fields add significantly to both the misalignment force and moment. It is noteworthy to mention that the combdrive capacitance computed using a 3-D FE model is much higher than the 2-D capacitance, which is important to account for when using a combdrive with surrounding circuitry.
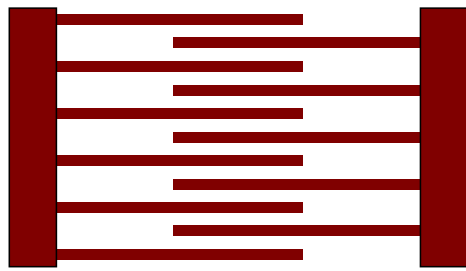
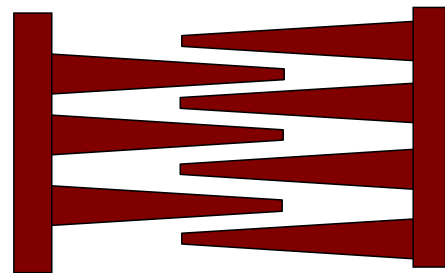(a) Straight fingers (original)
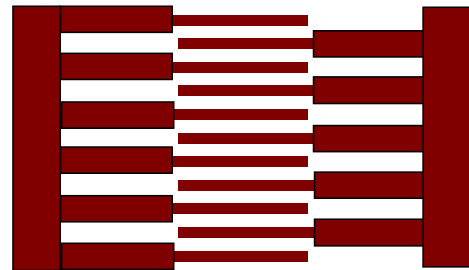
(b) Straight fingers (modif.)
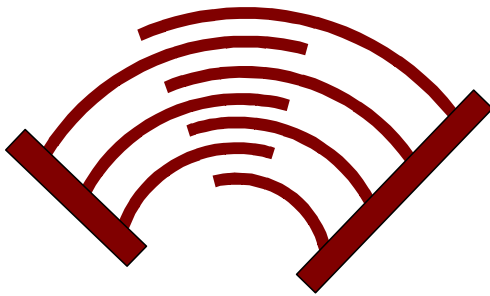
(c) Curved fingers

(d) Conical fingers

Figure 31: Typical geometries of the lateral in-plane combdrives

Figure 32: Basic geometry of the lateral combdrive actuator
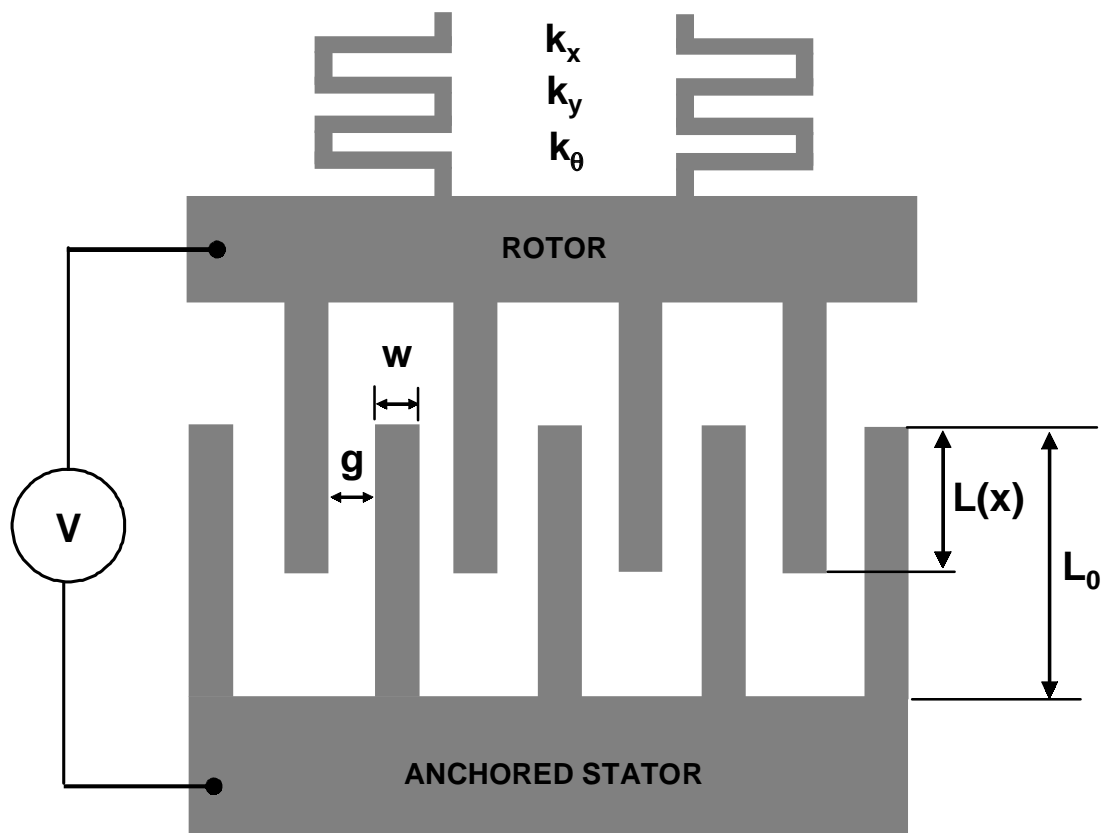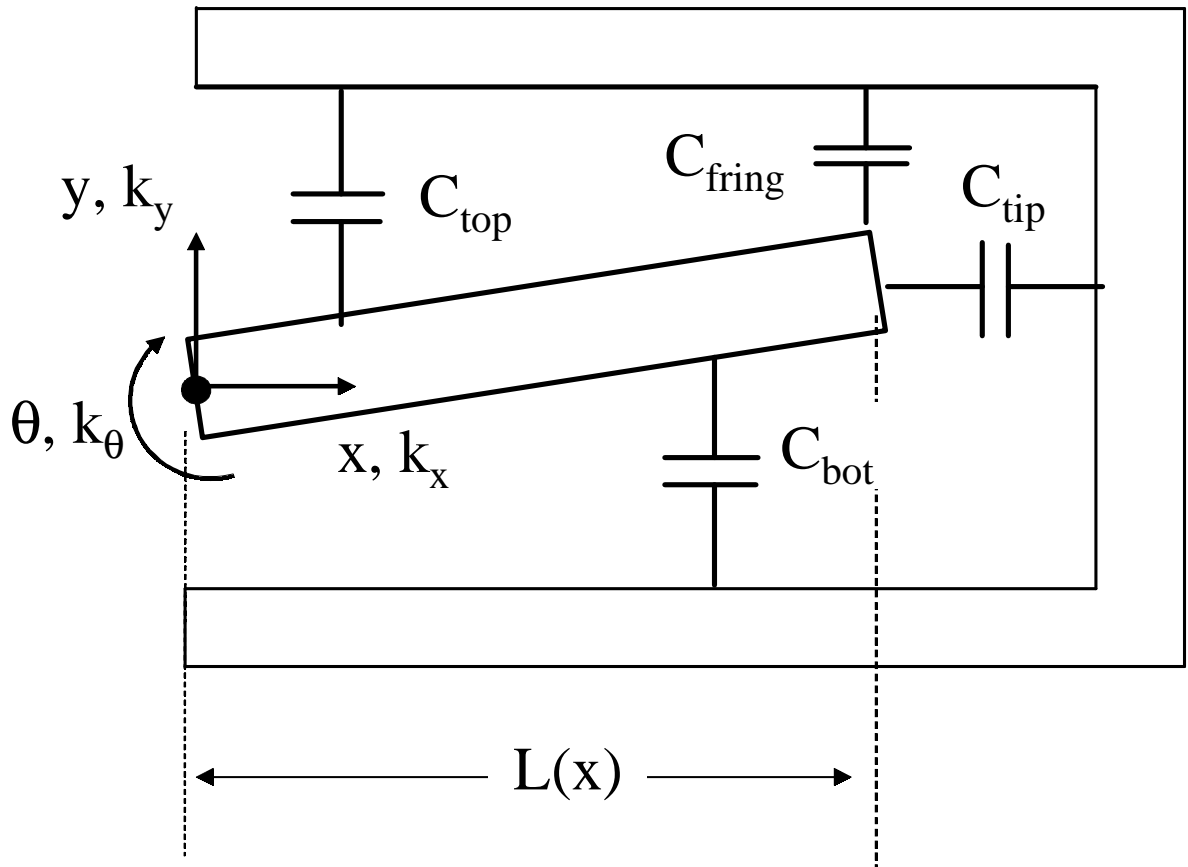
Figure 33: Analytical 2-D model of the representative combdrive finger
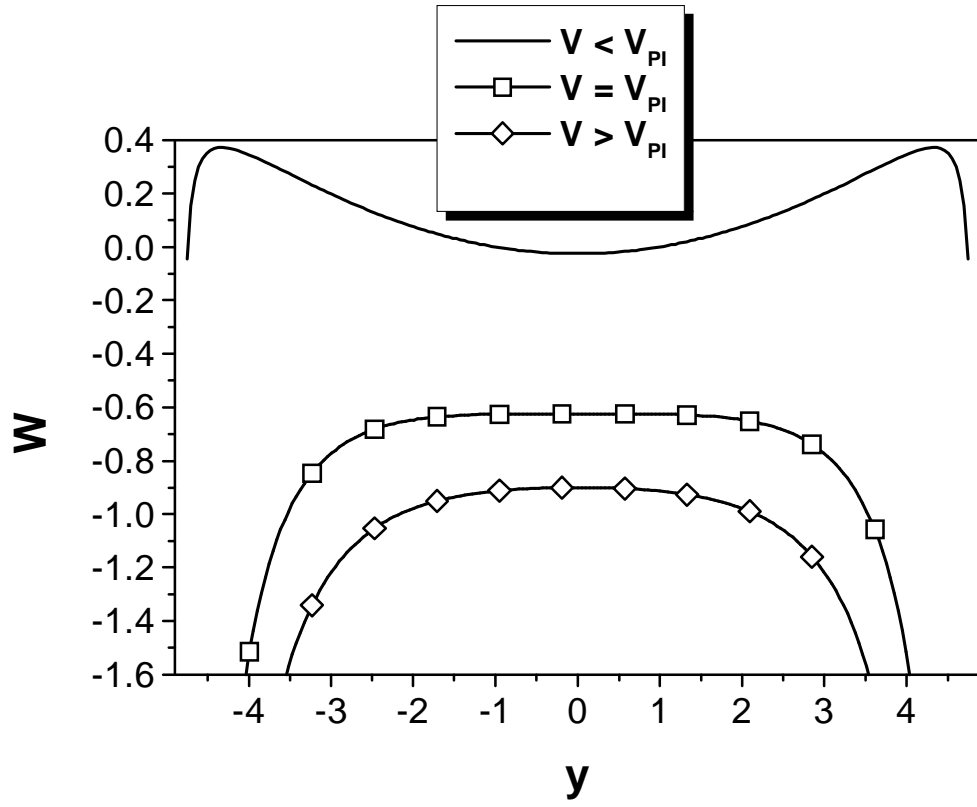
Figure 34: Total potential energy of the combdrive as a function of the translational mis-alignment, y
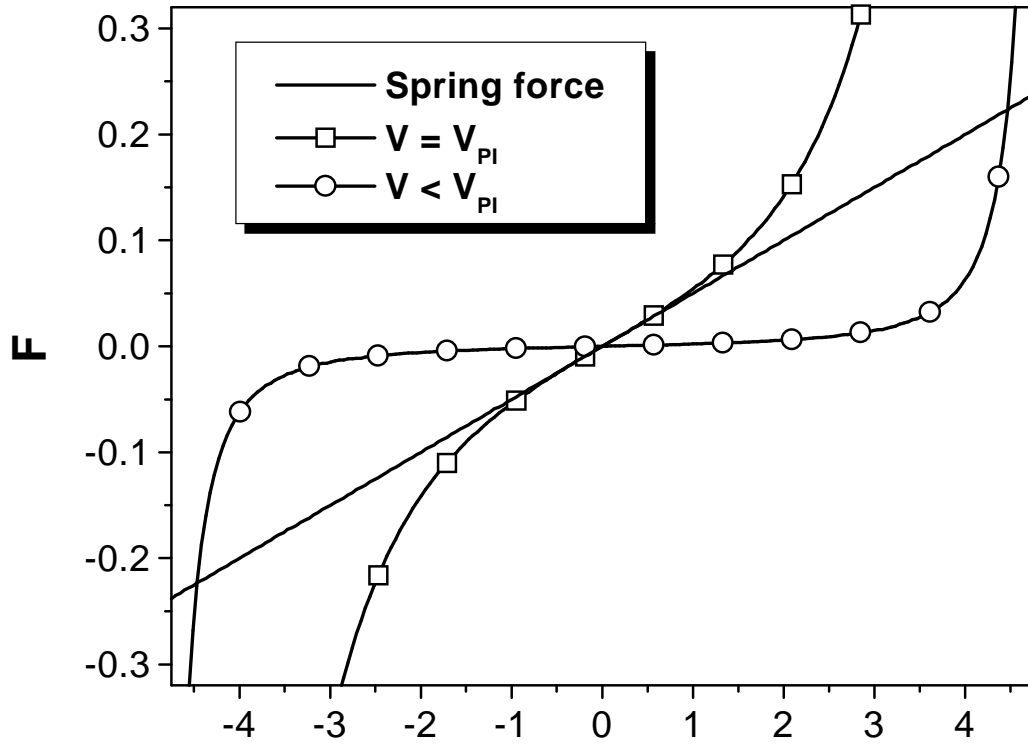
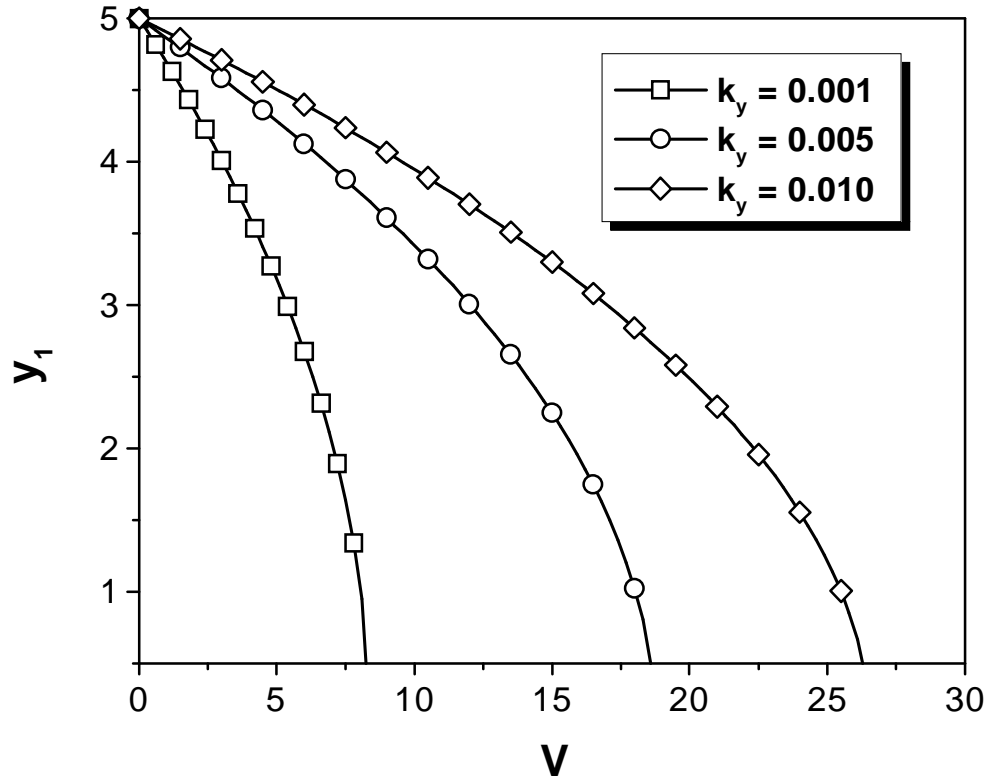Figure 35: Electrostatic force as a function of the translational misalignment, y (μm)

Figure 36: Equilibrium state (y_1) of the misaligned combdrive as a function of the applied voltage

5.4   STRONGLY COUPLED FE MODELS

The uncoupled FE models used to calculate the forces and moments caused by misalignments with fringing effects are incapable of solving the static equilibrium combdrive problem. A new treatment is therefore necessary. In this section, a strongly-coupled 2-D FE model is introduced that is based on a triangular (2-D) transducer [25]. The strongly-coupled FE model allows the analysis of electrostatic and mechanical domains simultaneously. The transducer element potential energy is stored in the electrostatic domain. The energy change is associated with the change of potential distribution in the system, which produces structural reaction forces. The reaction "forces" are electrical charge, and mechanical forces, F_x and F_y. The FE formulation of a transducer follows standard Ritz - Galerkin variational principles which ensure that it is compatible with regular finite elements [16].

The goal of the coupled-field analysis is to determine the pull-in voltage and critical misalignments. There are several methods of accomplishing this [59]. The current technique is based on a semi-automatic algorithm. The semi-automatic algorithm incrementally increases the applied voltage until the non-linear FE solver diverges. After diverging, the incrementally applied voltage is bisected until the desired accuracy is reached. This technique is beneficial because it can be widely applied to complicated geometries and an arbitrary number of electrodes [25].

The translational misalignment was modelled using the coupled-field model and the results of the static simulation were compared to the analytical results. Figure 43 depicts the pull-in voltage as a function of the spring stiffness (selected sensitivity parameter) for the strongly coupled FE model and the analytical solution given by (5.10). As shown in the figure, the analytical and FE results match very closely as the maximum difference between the analytical and the FE curves are less than 5%. This difference can be attributed to the fringing electrostatic fields modelled using FEM.

5.5 SUMMARY

In this chapter, three techniques have been developed and utilized for the static simulation of a misaligned combdrive: (1) analytical, (2) uncoupled 2-D/3-D FE models, and (3) coupled FE models. The analytical model provided a closed-form solution for the forces and moments produced by a combdrive's electrostatic field. Despite ignoring fringing field effects in the combdrive, the analytical model showed that the driving force in a misaligned combdrive was a non-linear function of stroke. In addition, the misaligned driving force was determined to be substantially greater than a perfectly aligned combdrive. The uncoupled finite element approach showed that fringing fields significantly contribute to the capacitance of the combdrive. When compared to the two-dimensional analytical model, including the three-dimensional fringing fields substantially increased the electrostatic forces and moments that develop. Based on these results, it can be concluded that the accuracy of the two-dimensional analytical models current utilized for combdrives can be improved by including three-dimensional fringing field effects. As demonstrated in this chapter, one of the best ways to accomplish this is to utilize the finite element method to evaluate fringing field effects that can be implemented as correction factors in the analytical model.

In conjunction with determining the influence of the fringing fields, the stability of the combdrive equilibrium states was studied using a one-dimensional model that included rotational and lateral springs. In the model, the stiffness of the lateral spring was much smaller than the rotational spring. Such a simplification allowed us to verify a coupled-field finite element analysis technique for determining the pull-in behavior of the combdrive. Utilizing this technique, the value of the critical voltage for the translational pull-in was found to be a function of the geometrical properties of the combdrive and the structural properties of the actuator. This critical voltage is important design parameters and should not be exceeded during the operation of the combdrive to maintain stability over the designed operational range. Unlike the electrostatic forces and moments, a comparison between the analytical and coupled-field FE model showed that fringing fields have little effect on the pull-in voltage for the combdrive geometry studied. Finally, the coupled field FE model also determined that the coupling between the combdrive DOFs leads to a coupling of the pull-in parameters.
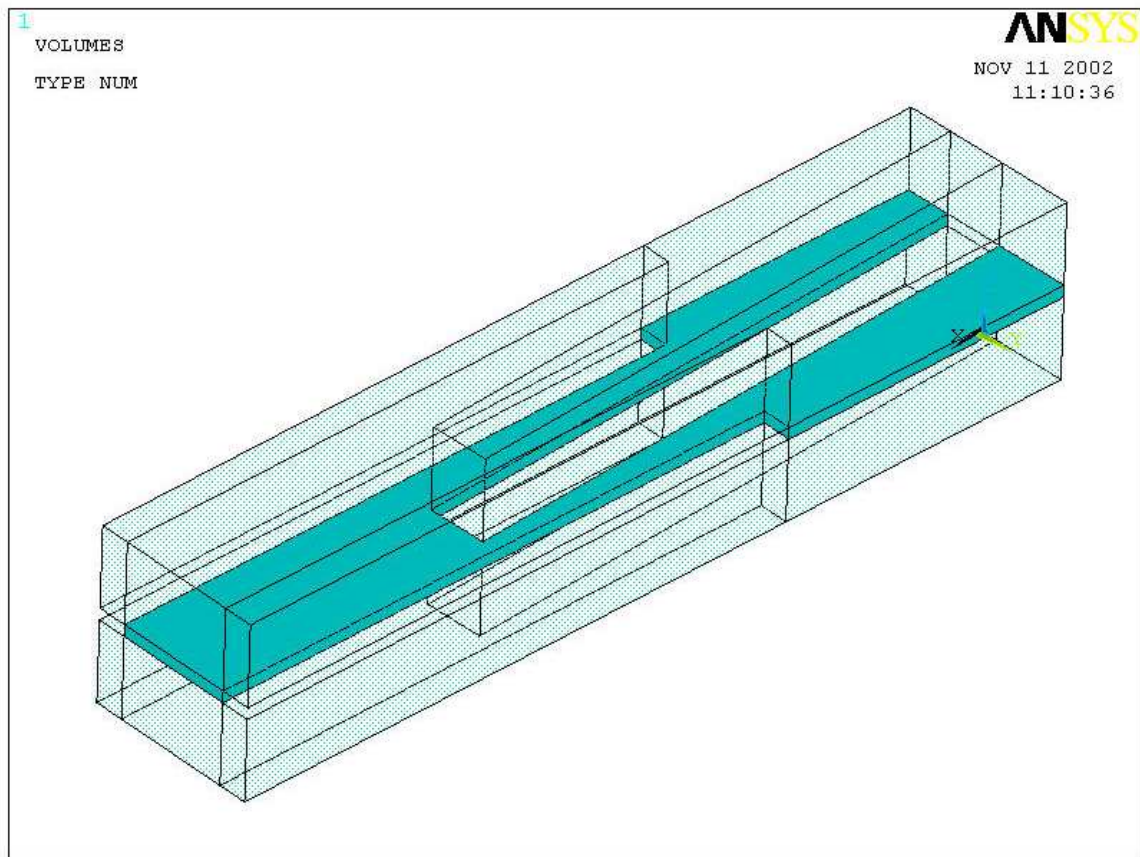
Figure 37: 3-D electrostatic FE model of the combdrive finger used for energy computation
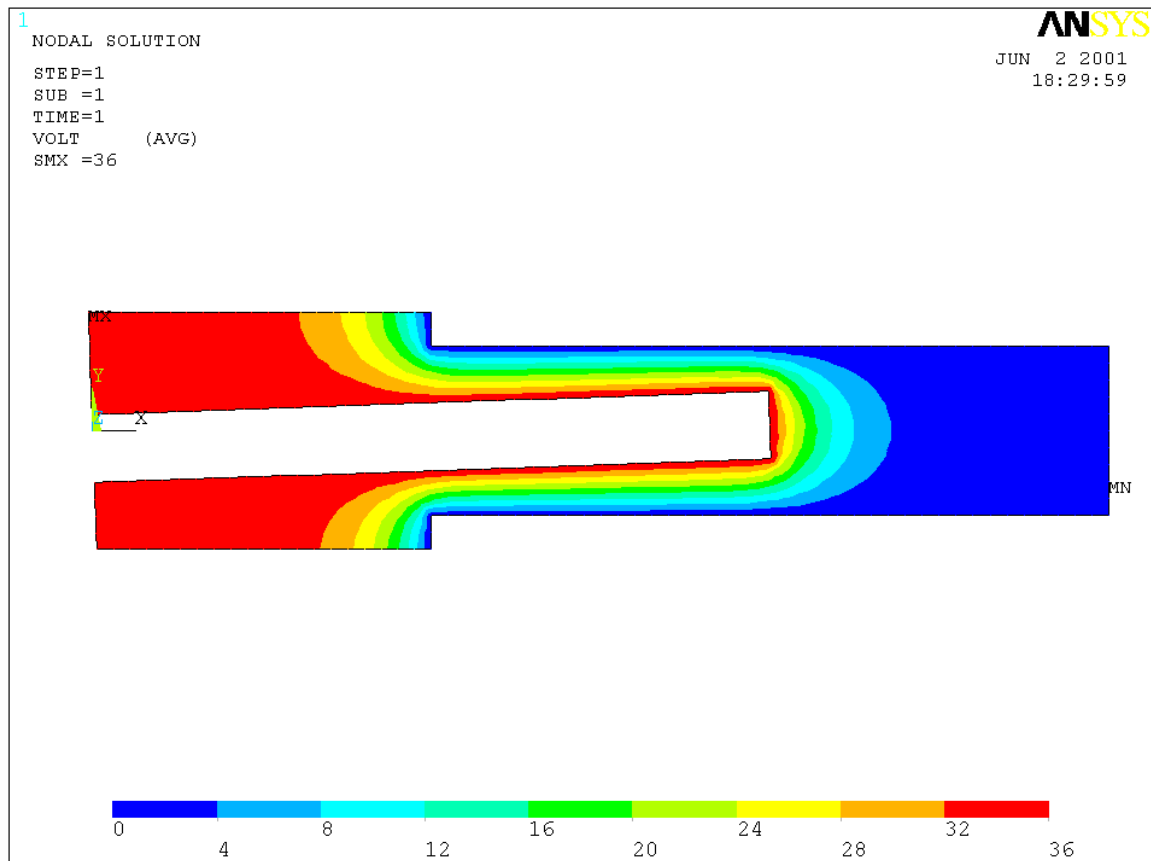
Figure 38: Potential distribution of the electrostatic field representing fringing and tip fields (2-D cross section)
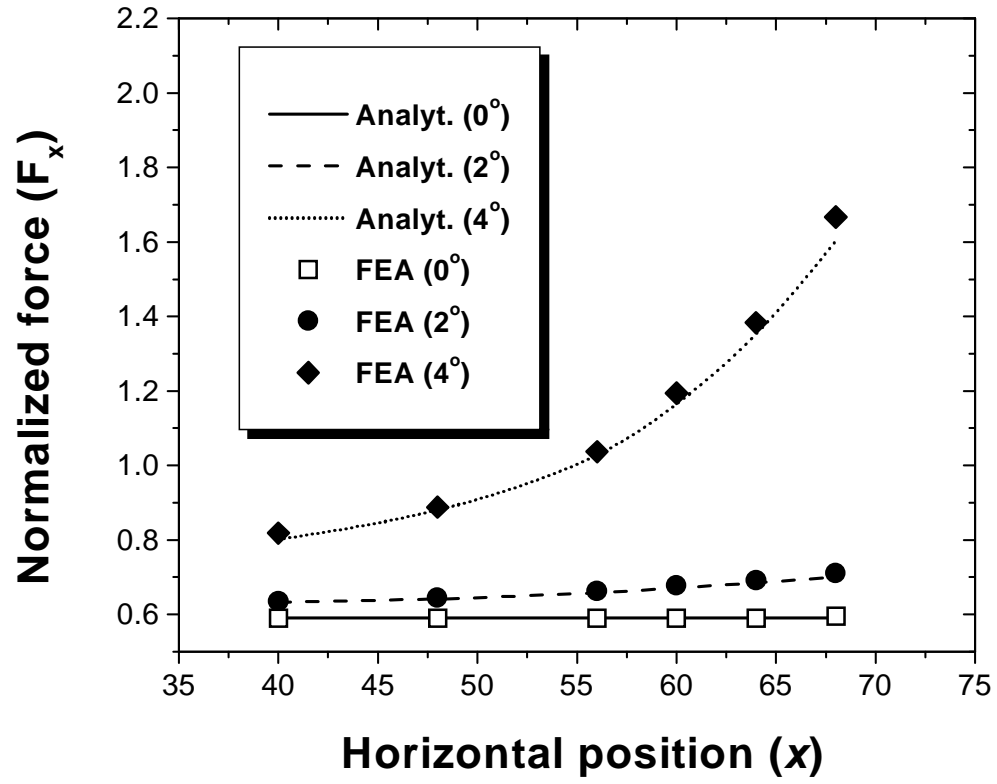
Figure 39: Normalized driving force as a function of the finger overlap (in μm) for three different angular misalignments (Model 1)
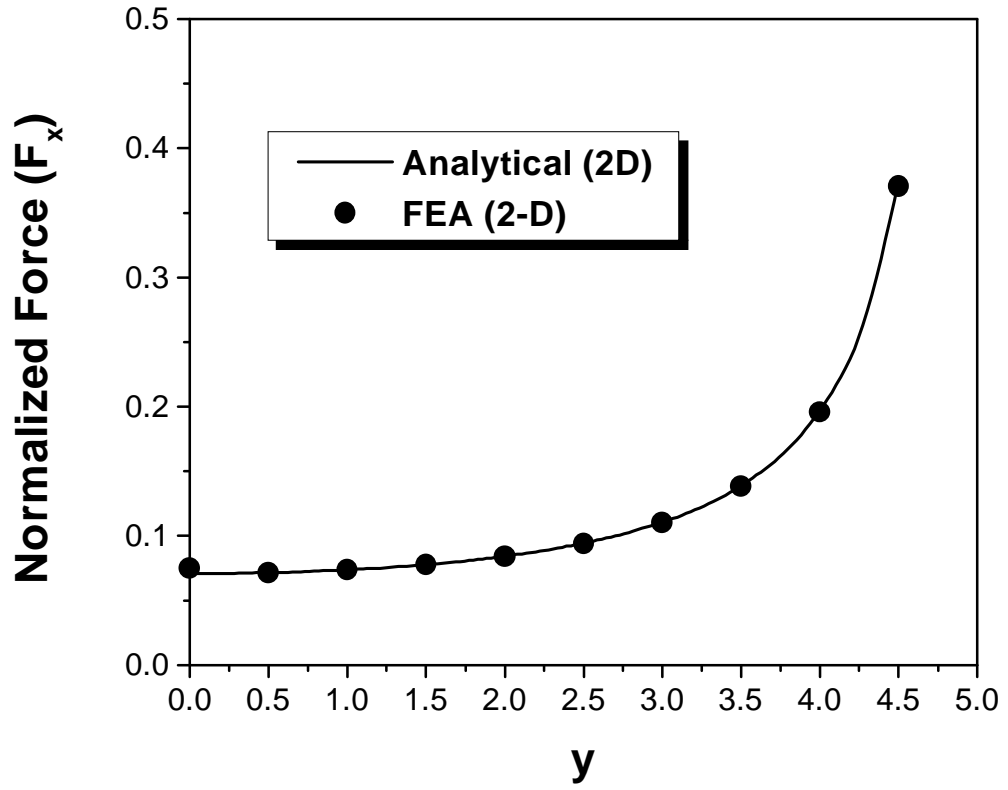
Figure 40: Normalized driving force as a function of vertical misalignment y (in μm) for $\theta = 0$ (Model 1)
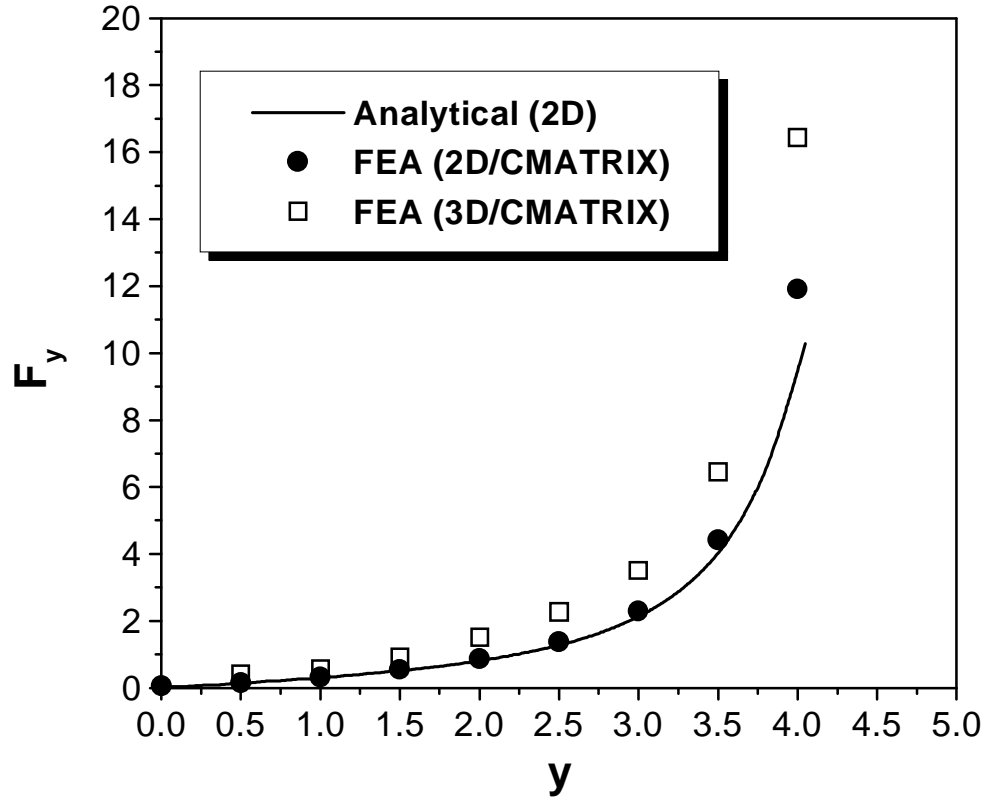
Figure 41: Generated by misalignment force as a function of misalignment y (in μm) for $\theta = 0$ (Model 2))
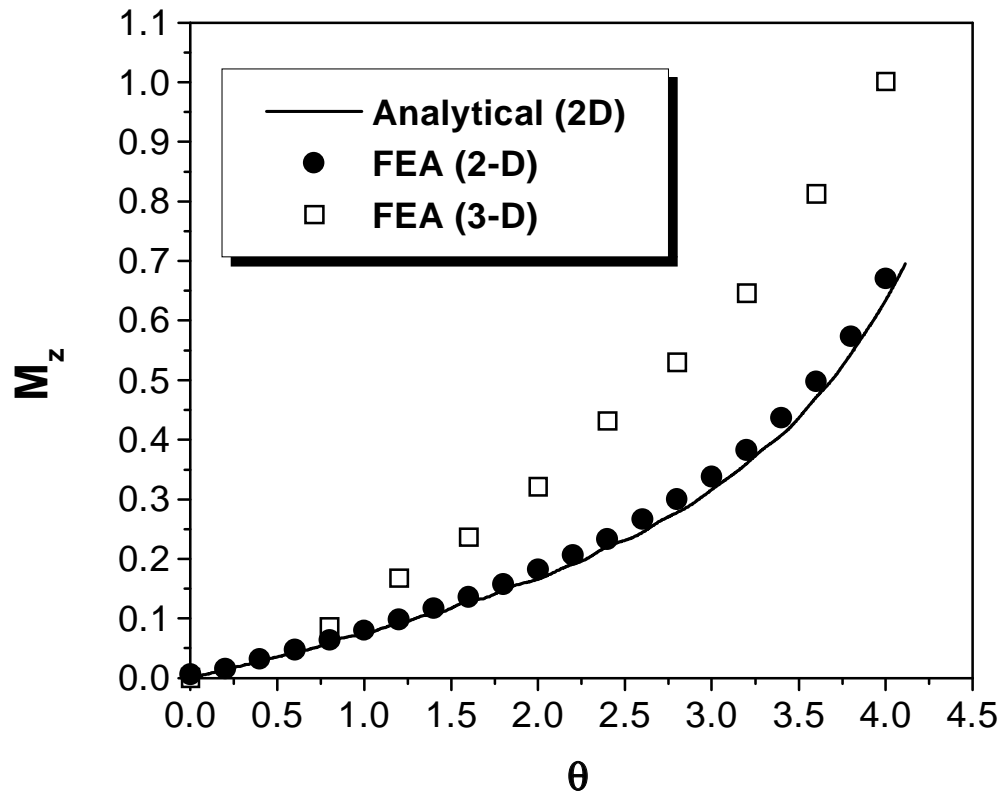
Figure 42: Generated by misalignment moment as a function of θ for $y = 0$ (Model 2)

Figure 43: Pull-in voltage as a function of spring stiffness

6.0   CONCLUSIONS

6.1   CONTRIBUTIONS

Complex configurations of MEMS devices require the development of new and more efficient finite element modeling techniques. The goal of this research was to develop novel numerical analysis techniques for solving coupled field electromechanical problems in MEMS. The effects of combdrive misalignments on the performance of MEMS devices were specifically addressed due to the lack of theoretical and numerical investigations available in this area.

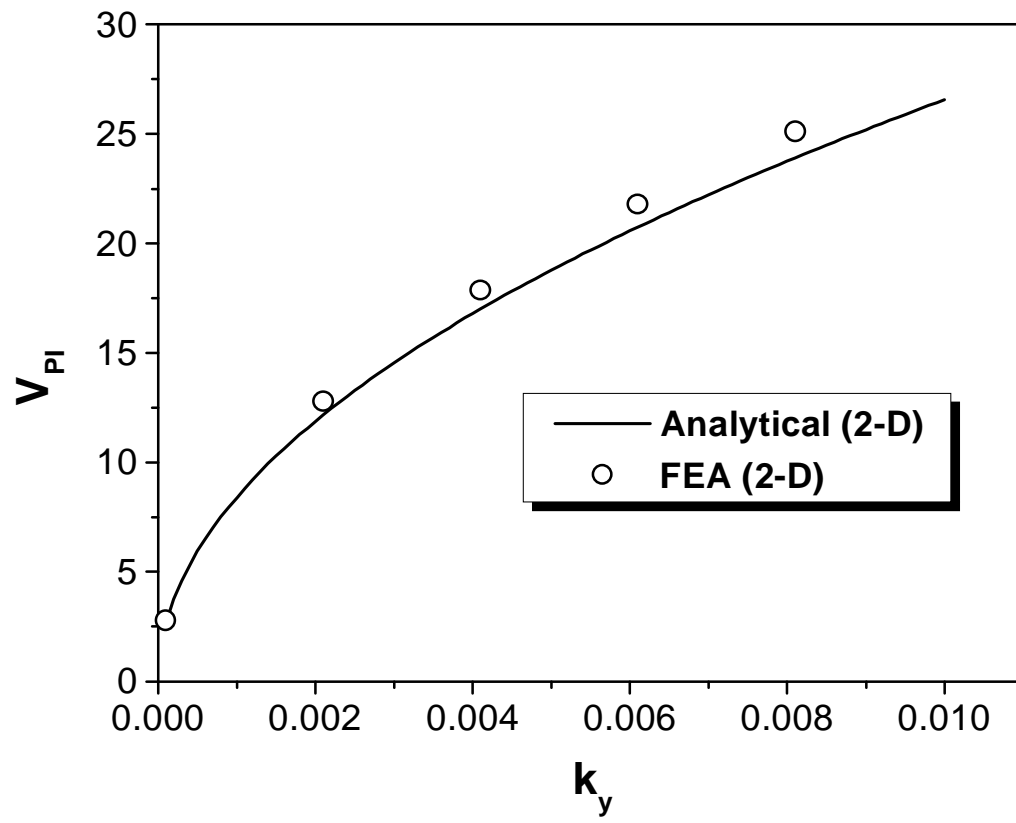In Chapter 3, a new generalized 2-D lumped transducer finite element was presented. The element had strong coupling between rigid or deformable mechanical domains and electrostatic domain that was characterized by slightly curved electrostatic fields. The element is compatible with beam and 2-D plane elements. Based on energy conservation and the principle of virtual work, the element formulation and finite element code were developed for the transducer using ANSYS element technology and non-linear solvers. The developed element was used to solve several representative benchmark problems that show its effectiveness and accuracy in capturing fundamental coupled field effects such as pull-in and release. Experimental and numerical results were used to verify element formulation. The 2-D transducer is a natural extension of 1-D lumped transducers widely used by designers. It requires fewer elements and produces more accurate results for the coupled field problems without significant fringing field effects.

A novel 3-D strongly coupled tetrahedral transducer finite element for modeling the quasi-static behavior of analog electrostatic MEMS devices was presented in Chapter 4. This new transducer element, which can be utilized for a broad range of micro-system applications (i.e. combdrives, micromirrors, and electrostatic motors), is compatible with conventional

electrostatic and structural 3-D finite elements. The element is capable of efficiently modeling interaction between deformable or rigid conductors that generate an electrostatic field. Strong coupling between the electrostatic and mechanical domains allows the static element formulation to be extended to transient and full harmonic analyses. Therefore, in many respects, the element is the most sophisticated FEA tool available for modeling MEMS problems where dominant fringing fields develop. The new technology is also very efficient in determining the pull-in parameters of complicated multi-electrode microdevices.

Four important characteristics of the developed element formulation are: (1) the formulation was derived from the energy conservation principles (general approach), (2) there was no assumptions made regarding the electrostatic domain (modeling fringing fields), (3) all finite element vector and matrices were analytically integrated (high accuracy), and (4) formulation provides an internal morphing capability (no remeshing is required). Several numerical examples were presented to verify element formulation and to identify the role of element parameters in the non-linear solution process. Available experimental data and numerical solutions were used as the references. The new element compared well with the experimental data and provided solutions requiring more sophisticated experimental validation.

In Chapter 5, three techniques were developed and utilized for the static simulation of a misaligned combdrive: (1) analytical, (2) uncoupled 2-D/3-D FE models, and (3) coupled FE models. The analytical model provided a closed-form solution for the forces and moments produced by a combdrive's electrostatic field. Despite ignoring fringing field effects in the combdrive, the analytical model showed that the driving force in a misaligned combdrive was a non-linear function of stroke. In addition, the misaligned driving force was determined to be substantially greater than a perfectly aligned combdrive. The uncoupled finite element approach showed that fringing fields significantly contribute to the capacitance of the combdrive. When compared to the two-dimensional analytical model, the three-dimensional fringing fields included in the uncoupled finite element approach substantially increased the electrostatic forces and moments that developed.

In conjunction with determining the influence of the fringing fields, the stability of the combdrive equilibrium states was studied using a one-dimensional model that included rotational and lateral springs. In the model, the stiffness of the lateral spring was much smaller

than the rotational spring. Such a simplification allowed us to verify a coupled-field finite element analysis technique for determining the pull-in behavior of the combdrive. Utilizing this technique, the value of the critical voltage for the translational pull-in was found to be a function of the geometrical properties of the combdrive and the structural properties of the actuator. This critical voltage is an important design parameters and should not be exceeded during the operation of the combdrive to maintain stability over the designed operational range. Unlike the electrostatic forces and moments, a comparison between the analytical and coupled-field FE model showed that fringing fields have little effect on the pull-in voltage for the combdrive geometry studied. Finally, the coupled-field FE model also determined that the coupling between the combdrive degrees of freedom (DOF) leads to a coupling of the pull-in parameters.

6.2 SUGGESTIONS FOR FUTURE WORK

The developed formulation for static analysis can be extended to transient, modal, and harmonic analyses. Since most of the inertia effects are associated with the mechanical domain, minimal changes to the transducer formulation will be required when extending the element to other domains. An automatic method for determining pull-in parameters can also be developed. Such a method would allow designers to automatically solve optimization problem using the space of design parameters.

The developed 2-D generalized lumped transducer element formulation can be extended to lumped 3-D formulation based on plate/shell capacitance approximation. The 3-D coupled field transducer element can be generalized to include magnetic, thermal, or acoustic domains. The same energy principles as those used in this work should be used to construct the most general coupled field element.

Finally, the coupled field technology developed in this work should be extended to model nano-structures and nano-devices. Accomplishing this task will require incorporating atomic and molecular interaction into solid modeling techniques and formulation.

APPENDIX A

DERIVATIVES OF 2-D LUMPED CAPACITANCE

Capacitance of the 2-D lumped transducer element is given by

$$C^{(e)}(x_1, y_1, x_2, y_2) = \epsilon w \left(\frac{x_2 - x_1}{y_2 - y_1} \right) \ln \left(\frac{y_2}{y_1} \right), \qquad y_1 \neq y_2 \tag{A.1}$$

First-order derivatives with respect to nodal coordinates are given by $(y_1 \neq y_2)$

$$\frac{\partial C^{(e)}}{\partial x_1} = -\epsilon w \frac{1}{y_2 - y_1} \ln \left(\frac{y_2}{y_1} \right) \tag{A.2}$$

$$\frac{\partial C^{(e)}}{\partial x_2} = \epsilon w \frac{1}{y_2 - y_1} \ln \left(\frac{y_2}{y_1} \right) \tag{A.3}$$

$$\frac{\partial C^{(e)}}{\partial y_1} = \epsilon w \left(\frac{x_2 - x_1}{y_2 - y_1} \right) \left[\frac{1}{y_2 - y_1} \ln \left(\frac{y_2}{y_1} \right) - \frac{1}{y_1} \right] \tag{A.4}$$

$$\frac{\partial C^{(e)}}{\partial y_2} = -\epsilon w \left(\frac{x_2 - x_1}{y_2 - y_1} \right) \left[\frac{1}{y_2 - y_1} \ln \left(\frac{y_2}{y_1} \right) - \frac{1}{y_2} \right] \tag{A.5}$$

Second-order derivatives with respect to nodal coordinates are given by $(y_1 \neq y_2)$

$$\frac{\partial^2 C^{(e)}}{\partial x_1^2} = \frac{\partial^2 C^{(e)}}{\partial x_2^2} = 0 \tag{A.6}$$

$$\frac{\partial^2 C^{(e)}}{\partial x_1 \partial x_2} = \frac{\partial^2 C^{(e)}}{\partial x_2 \partial x_1} = 0 \tag{A.7}$$

$$\frac{\partial^2 C^{(e)}}{\partial x_1 \partial y_1} = \frac{\partial^2 C^{(e)}}{\partial y_1 \partial x_1} = -\epsilon w \left(\frac{1}{y_2 - y_1}\right) \left[\frac{1}{y_2 - y_1} \ln\left(\frac{y_2}{y_1}\right) - \frac{1}{y_1}\right] \tag{A.8}$$

$$\frac{\partial^2 C^{(e)}}{\partial x_1 \partial y_2} = \frac{\partial^2 C^{(e)}}{\partial y_2 \partial x_1} = \epsilon w \left(\frac{1}{y_2 - y_1}\right) \left[\frac{1}{y_2 - y_1} \ln\left(\frac{y_2}{y_1}\right) - \frac{1}{y_2}\right] \tag{A.9}$$

$$\frac{\partial^2 C^{(e)}}{\partial x_2 \partial y_1} = \frac{\partial^2 C^{(e)}}{\partial y_1 \partial x_2} = \epsilon w \left(\frac{1}{y_2 - y_1}\right) \left[\frac{1}{y_2 - y_1} \ln\left(\frac{y_2}{y_1}\right) - \frac{1}{y_1}\right] \tag{A.10}$$

$$\frac{\partial^2 C^{(e)}}{\partial x_2 \partial y_2} = \frac{\partial^2 C^{(e)}}{\partial y_2 \partial x_2} = -\epsilon w \left(\frac{1}{y_2 - y_1}\right) \left[\frac{1}{y_2 - y_1} \ln\left(\frac{y_2}{y_1}\right) - \frac{1}{y_2}\right] \tag{A.11}$$

$$\frac{\partial^2 C^{(e)}}{\partial y_1^2} = \epsilon w \left[\frac{x_2 - x_1}{(y_2 - y_1)^2}\right] \left[\frac{1}{y_2 - y_1} \ln\left(\frac{y_2}{y_1}\right) - \frac{1}{y_2}\right] + \frac{x_2 - x_1}{(y_2 - y_1)^2 y_1^2} \tag{A.12}$$

$$\frac{\partial^2 C^{(e)}}{\partial y_2^2} = -\epsilon w \left[\frac{x_2 - x_1}{(y_2 - y_1)^2}\right] \left[\frac{1}{y_2 - y_1} \ln\left(\frac{y_2}{y_1}\right) - \frac{1}{y_2}\right] - \frac{x_2 - x_1}{(y_2 - y_1)^2 y_2^2} \tag{A.13}$$

$$\frac{\partial^2 C^{(e)}}{\partial y_1 \partial y_2} = -\epsilon w \left[\frac{x_2 - x_1}{(y_2 - y_1)^2}\right] \left[\frac{1}{y_2 - y_1} \ln\left(\frac{y_2}{y_1}\right) - \frac{1}{y_2}\right] \tag{A.14}$$

APPENDIX B

3-D TRANSDUCER ELEMENT NORMALS

The Cartesian coordinate system is defined by three normal axes: $\mathbf{i}$, $\mathbf{j}$, and $\mathbf{k}$. The tetrahedral transducer element normals are given by

$$\mathbf{n}_1 = \frac{\mathbf{e}_{24} \times \mathbf{e}_{23}}{2A_1} = \begin{vmatrix} \mathbf{i} & \mathbf{i} & \mathbf{k} \\ x_4 - x_2 & y_4 - y_2 & z_4 - z_2 \\ x_3 - x_2 & y_3 - y_2 & z_3 - z_2 \end{vmatrix} \tag{B.1}$$

$$\mathbf{n}_2 = \frac{\mathbf{e}_{13} \times \mathbf{e}_{14}}{2A_2} = \begin{vmatrix} \mathbf{i} & \mathbf{i} & \mathbf{k} \\ x_3 - x_1 & y_3 - y_1 & z_3 - z_1 \\ x_4 - x_1 & y_4 - y_1 & z_4 - z_1 \end{vmatrix} \tag{B.2}$$

$$\mathbf{n}_3 = \frac{\mathbf{e}_{14} \times \mathbf{e}_{12}}{2A_3} = \begin{vmatrix} \mathbf{i} & \mathbf{i} & \mathbf{k} \\ x_4 - x_1 & y_4 - y_1 & z_4 - z_1 \\ x_2 - x_1 & y_2 - y_1 & z_2 - z_1 \end{vmatrix} \tag{B.3}$$

$$\mathbf{n}_4 = \frac{\mathbf{e}_{12} \times \mathbf{e}_{13}}{2A_4} = \begin{vmatrix} \mathbf{i} & \mathbf{i} & \mathbf{k} \\ x_2 - x_1 & y_2 - y_1 & z_2 - z_1 \\ x_3 - x_1 & y_3 - y_1 & z_3 - z_1 \end{vmatrix} \tag{B.4}$$

90

APPENDIX C

3-D TRANSDUCER ELEMENT VOLUME

The tetrahedral transducer element volume, V, is given by

$$V = -\frac{1}{6} \begin{vmatrix} x_1 & y_1 & z_1 & 1 \\ x_2 & y_2 & z_2 & 1 \\ x_3 & y_3 & z_3 & 1 \\ x_4 & y_4 & z_4 & 1 \end{vmatrix} \tag{C.1}$$

First-order derivatives of the tetrahedral transducer element volume (C.1) with respect to nodal coordinates are given by

$$\frac{\partial V}{\partial x_1} = -\frac{1}{6}\left(y_3 z_4 - y_4 z_3 - y_2 z_4 + y_4 z_2 + y_2 z_3 - y_3 z_2\right) \tag{C.2}$$

$$\frac{\partial V}{\partial y_1} = -\frac{1}{6}\left(z_3 x_4 - z_4 x_3 - z_2 x_4 + z_4 x_2 + z_2 x_3 - z_3 x_2\right) \tag{C.3}$$

$$\frac{\partial V}{\partial z_1} = -\frac{1}{6}\left(x_3 y_4 - x_4 y_3 - x_2 y_4 + x_4 y_2 + x_2 y_3 - x_3 y_2\right) \tag{C.4}$$

$$\frac{\partial V}{\partial x_2} = -\frac{1}{6}\left(-y_3 z_4 + y_4 z_3 - y_4 z_1 + y_1 z_4 + y_3 z_1 - y_1 z_3\right) \tag{C.5}$$

$$\frac{\partial V}{\partial y_2} = -\frac{1}{6}\left(-z_3 x_4 + z_4 x_3 - z_4 x_1 + z_1 x_4 + z_3 x_1 - z_1 x_3\right) \tag{C.6}$$

$$\frac{\partial V}{\partial z_2} = -\frac{1}{6}\left(-x_3 y_4 + x_4 y_3 - x_4 y_1 + x_1 y_4 + x_3 y_1 - x_1 y_3\right) \tag{C.7}$$

$$\frac{\partial V}{\partial x_3} = -\frac{1}{6}\left(-y_4 z_2 + y_2 z_4 + y_4 z_1 - y_1 z_4 + y_1 z_2 - y_2 z_1\right) \tag{C.8}$$

$$\frac{\partial V}{\partial y_3} = -\frac{1}{6}\left(-z_4 x_2 + z_2 x_4 + z_4 x_1 - z_1 x_4 + z_1 x_2 - z_2 x_1\right) \tag{C.9}$$

$$\frac{\partial V}{\partial z_3} = -\frac{1}{6}\left(-x_4 y_2 + x_2 y_4 + x_4 y_1 - x_1 y_4 + x_1 y_2 - x_2 y_1\right) \tag{C.10}$$

$$\frac{\partial V}{\partial x_4} = -\frac{1}{6}\left(-y_2 z_3 + y_3 z_2 + y_1 z_3 - y_3 z_1 - y_1 z_2 + y_2 z_1\right) \tag{C.11}$$

$$\frac{\partial V}{\partial y_4} = -\frac{1}{6}\left(-z_2 x_3 + z_3 x_2 + z_1 x_3 - z_3 x_1 - z_1 x_2 + z_2 x_1\right) \tag{C.12}$$

$$\frac{\partial V}{\partial z_4} = -\frac{1}{6}\left(-x_2 y_3 + x_3 y_2 + x_1 y_3 - x_3 y_1 - x_1 y_2 + x_2 y_1\right) \tag{C.13}$$

BIBLIOGRAPHY

[1] R.P. Feynman. There's plenty of room at the bottom. *Journal of Microelectromechanical Systems*, 1(1):60–66, 1992.

[2] R.P. Feynman. Infinitesimal machinery. 2(1):4–14, 1993.

[3] N. Maluf. *An Introduction to Microelectromechanical Systems Engineering*. Artech House, Boston, MA, 2000.

[4] W.H. Ko. The future of sensor and actuator systems. 56:193–197, 1996.

[5] H. Fujita. Future of actuators and microsystems. *Sensors and Actuators A*, 56:105–111, 1996.

[6] B.E. Boser R.T. Howe and A.P. Pisano. Polysilicon integrated microsystems: technologies and applications. *Sensors and Actuators A*, 56:167–177, 1996.

[7] H. Baltes. Future of ic microtransducers. *Sensors and Actuators A*, 56:179–192, 1996.

[8] M. Bao and W. Wang. Future of microelectromechanical systems (mems). *Sensors and Actuators A*, 56:135–141, 1996.

[9] J. Fluitman. Microsystems technology: objectives. *Sensors and Actuators A*, 56:151–166, 1996.

[10] J. Bryzek. Impact of mems technology on society. *Sensors and Actuators A*, 56:1–9, 1996.

[11] S.D. Senturia. The future of microsensor and microactuator design. *Sensors and Actuators A*, 56:125–127, 1996.

[12] G. Wachutka. Problem-oriented modeling of microtransducers: state of the art and future challenges. *Sensors and Actuators A*, 41-42:279–283, 1994.

[13] G. Wachutka. Tailored modeling: a way to the 'virtual microtransducer fab'? *Sensors and Actuators A*, 46-47:603–612, 1995.

[14] M.R. Lovell I.V. Avdeev and Jr. D. Onipede. Modeling in-plane misalignments in lateral combdrive transducers. *Journal of Micromechanics and Microengineering*, 13:809–815, 2003.

[15] T.-C. H. Nguyen W.C. Tang and R.T. Howe. Laterally driven polysilicon resonant microstructures. *Sensors and Actuators A*, 20:25–32, 1989.

[16] *ANSYS Release 5.6 User Manuals.* Canonsburg, PA, USA: ANSYS Inc., 1999.

[17] *www.coventor.com.* 2003.

[18] A.J. Sangster and V.D. Samper. Accuracy assessment of 2-d and 3-d fe models of a double-stator electrostatic wobble motor. *Journal of Microelectromechanical Systems*, 6(2):142–150, 1997.

[19] *OPERA Software for Electromagnetic Design.* Oxford, U.K.: Vector Fields Limited, 2002.

[20] C. Mul M.H.W. Bonse and J.W. Spronck. Finite-element modeling as a tool for designing capacitive position sensors. *Sensors and Actuators A*, 46-47:266–269, 1995.

[21] *Maxwell 2D Field Simulator, Version 4.3, Release Notes.* Pittsburgh, PA, USA: Ansoft Corporation, 1991.

[22] Y.C. Liang V.J. Logeeswaran F.E.H. Tay, X. Jun and Y. Yufeng. The effects of non-parallel plates in a differential capacitive microaccelerometer. *Journal of Micromechanics and Microengineering*, 9:283–293, 1999.

[23] H. Graef M. Fischer and W. von Munch. Electrostatically deflectable polysilicon torsional mirrors. *Sensors and Actuators A*, 44:83–89, 1994.

[24] S. Garcia-Alonso E. Castano F.J. Gracia G. Bistue, J.G. Elizalde and A. Garcia-Alonso. A design tool for pressure microsensors based on fem simulations. *Sensors and Actuators A*, 62:591–594, 1997.

[25] D. Ostergaard M. Gyimesi and I. Avdeev. Triangle transducer for micro electro mechanical systems (mems) simulation in ansys finite element program. In *Proceedings of the Fifth International Conference on Modeling and Simulation of Microsystems*, pages 380–383, San Juan, Puerto Rico, April 2002.

[26] B.P. Johnson-S. Kim K. Nabors M.A. Shulman S.D. Senturia, R.M. Harris and J.K. White. A computer-aided design system for microelectromechanical systems (memcad). *Journal of Microelectromechanical Systems*, 1(1):3–14, 1992.

[27] R. Legtenberg J.R. Gilbert and S.D. Senturia. 3d coupled electromechanics for mems: applications of cosolve-em. In *Proceedings of the 1995 IEEE Conference on Micro Electro Mechanical Systems*, Amsterdam, January 1995.

[28] K. Nabors and J. White. Fastcap: A multipole-accelerated 3-d capacitance extraction program. *IEEE Transactions on Computer-Aided Design*, 10:1447–1459, 1991.

[29] *ABAQUS Manual*. Hibbitt, Karlsson and Sorenson: 1080 Main Street, Pawtucket, RI 02860 USA, 2003.

[30] S.D. Senturia R. Legtenberg, J. Gilbert and M. Elwenspoek. Electrostatic curved electrode actuators. *Journal of Microelectromechanical Systems*, 6(3):257–265, 1997.

[31] A. Lipson-T. Leitner D.J. Setter S. Kaldor O. Degani, E. Socher and Y. Nemirovsky. Pull-in study of an electrostatic torsion microactuator. *Journal of Microelectromechanical Systems*, 7:373379, 1998.

[32] P. Groth E.-R. Konig and G. Wachutka. New coupled-field device simulation tool for mems based on the tp2000 cad platform. *Sensors and Actuators A*, 76:9–18, 1999.

[33] J. Schaepperle-D. Eichner M. Weinmann W. von Munch M. Fischer, M. Giousouf and F. Assmus. Electrostatically deflectable polysilicon micromirrors – dynamic behavior and comparison with the results from fem modeling with ansys. *Sensors and Actuators A*, 67:89–95, 1998.

[34] T. Blochwitz A. Schroth and G. Gerlach. Simulation of a complex sensor using coupled simulation programs. *Sensors and Actuators A*, 54:632–635, 1996.

[35] M. Gyimesi and D. Ostergaard. Electro-mechanical transducer for mems in ansys. In *Proceedings of 1999 International Conference Modeling/Simulation of Microsystems*, 1999.

[36] J.S. Wang M. Gyimesi and D. Ostergaard. Capacitance computation by hybrid p-element-trefftz method. *IEEE Transactions on Magnetics*, 37:3680–3683, 2001.

[37] S. Ier T. Mukherjee and G.K. Fedder. Optimization-based synthesis of microresonators. *Sensors and Actuators A*, 70:118–127, 1998.

[38] J.E. Mehner L.D. Gabbay and S.D. Senturia. Computer-aided generation of nonlinear reduced-order dynamic macromodels–i: non-stress-stiffened case. *Journal of Microelectromechanical Systems*, 9(2):262–269, 2000.

[39] L.D. Gabbay J.E. Mehner and S.D. Senturia. Computer-aided generation of nonlinear reduced-order dynamic macromodels–ii: stress-stiffened case. *Journal of Microelectromechanical Systems*, 9(2):270–278, 2000.

[40] *ANSYS 5.7 Coupled Field Analysis Guide*. Canonsburg, PA, USA: ANSYS Inc., 2000.

[41] N.R. Aluru and J. White. An efficient numerical technique for electromechanical simulation of complicated microelectromechanical structures. *Sensors and Actuators A*, 58:1–11, 1997.

[42] M. Roos-G. Sartoris H.U. Schwarzenbach, J.G. Korvink and E. Anderheggen. A micro-electromechanical cad extension for seses. *Journal of Microelectromechanical Systems*, 3:162–171, 1994.

[43] M.W. Judy W.C. Tang, T.-C.H. Nguyen and R.T. Howe. Electrostatic-comb drive of lateral polysilicon resonators. *Sensors and Actuators A*, 21-23:328–331, 1990.

[44] R. Puers. apacitive sensors: when and how to use them. *Sensors and Actuators A*, 37-38:93–105, 1993.

[45] D. Ostergaard M. Gyimesi, D. Lavers and T. Pawlak. Hybrid fe-trefftz method for open boundary analysis. *IEEE Transactions on Magnetics*, 32(3):671–674, 1996.

[46] M. Gyimesi and D. Ostergaard. Fe based rom of micro electro mechanical systems (mems). In *Proceedings of the International Conference MSM 2000*, Sand Diego CA, March 2000.

[47] C. Kingsley Jr. A.E. Fitzgerald and S.D. Umans. *Electric Machinery*. McGraw-Hill Publishing Company, New York, 1990.

[48] S.A. Teukolsky W.H. Press, B.P. Flannery and W.T. Vetterling. *Numerical Recipes: The Art of Scientific Computing*. Cambridge University Press, Cambridge, 1986.

[49] M. Lovell I. Avdeev, M. Gyimesi and O. Onipede. Beam modeling for simulation of mems transducers using strong coupling approach. In *Abstracts of the Sixth US National Congress on Computational Mechanics*, Dearborn MI, August 2001.

[50] M. Lovell I. Avdeev and D. Onipede Jr. Design and simulation of microelectromechanical transducer using uncoupled finite element models. In *Proceedings of SPIE*, volume 4627, pages 230–238.

[51] G.K. Ananthasuresh J.R. Gilbert and S.D. Senturia. 3d modeling of contact and hysteresis in coupled electro-mechanics. In *Proceedings of MEMS'96*, pages 127–132, 1996.

[52] I.V. Avdeev M. Gyimesi and D. Ostergaard. Finite element simulation of micro electro mechanical systems (mems) by strongly coupled electro mechanical transducers. *IEEE Transactions on Magnetics*, accepted for publication.

[53] N.F. de Rooij V.P. Jaecklin, C. Linder and J.-M. Moret. Comb actuators for xy-microstages. *Sensors and Actuators A*, 39:83–89, 1993.

[54] R.A. Wickstrom H.C. Nathanson, W.E. Newell and J.R. Davis. The resonant gate transistor. *IEEE Trans. Electron Devices*, 14:117133, 1967.

[55] O. Bochobza-Degani and Y. Nemirovsky. Modeling the pull-in parameters of electrostatic actuators with a novel lumped two degrees of freedom pull-in model. *Sensors and Actuators A*, 97-98:569578, 2002.

[56] C.-Y. Hui A. J.-L. Yeh and N.C. Tien. Electrostatic model for an asymmetric combdrive. *Journal of Microelectromechanical Systems*, 9(1):126–135, 2000.

[57] J.A. Pelesko and D.H. Bernstein. *Modeling MEMS and NEMS.* Chapman and Hall/CRC Press, London/Boca Raton, FL, 2003.

[58] E.K. Chan and R.W. Dutton. Electrostatic micromechanical actuator with extended range of travel. *Journal of Microelectromechanical Systems*, 9:321–328, 2000.

[59] O. Bochobza-Degani D. Elata and Y. Nemirovsky. An efficient numerical algorithm for extracting pull-in hyper-surfaces of electrostatic actuators with multiple uncoupled electrodes. In *Proceedings of the Fifth International Conference on Modeling and Simulation of Microsystems*, page 206209, San Juan, Puerto Rico, April 2002.